12-8-2023

Characterization of isomeric states in neutron-rich nuclei approaching N = 28

Timilehin Hezekiah Ogunbeku
Mississippi State University, hezekiahogunbeku@gmail.com

Characterization of isomeric states in neutron-rich nuclei approaching $N = 28$

By

Timilehin Hezekiah Ogunbeku

Approved by:

Benjamin P. Crider (Major Professor)
Sean N. Liddick (Local Professor, Facility for Rare Isotope Beams, Michigan State University)
Jeff Allen Winger
Dipangkar Dutta
Gautam Rupak Lan Tai Moong
Henk F. Arnoldus (Graduate Coordinator)
Rick Travis (The Dean, College of Arts & Sciences)

A Dissertation
Submitted to the Faculty of
Mississippi State University
in Partial Fulfillment of the Requirements
for the Degree of Doctor of Philosophy
in Physics
in the Department of Physics and Astronomy

Mississippi State, Mississippi

December 2023

Name: Timilehin Hezekiah Ogunbeku

Date of Degree: December 8, 2023

Institution: Mississippi State University

Major Field: Physics

Major Professor: Benjamin P. Crider, Sean N. Liddick

Title of Study: Characterization of isomeric states in neutron-rich nuclei approaching $N = 28$

Pages of Study: 150

Candidate for Degree of Doctor of Philosophy

The investigation of isomeric states in neutron-rich nuclei provides useful insights into the underlying nuclear configurations, and understanding their occurrence along an isotopic chain can inform about shell evolution. Recent studies on neutron-rich Si isotopes near the magic number $N = 20$ and approaching $N = 28$ have revealed the presence of low-lying states with intruder configurations, resulting from multiple-particle, multiple-hole excitations across closed shell gaps. The characterization of these states involves measuring their half-lives and transition probabilities.

In this study, a new low-energy ($7/2^-_1$) isomer at 68 keV in ^{37}Si was accessed via β decay and characterized. To achieve this, radioactive ^{37}Al and ^{38}Al ions were produced through the projectile fragmentation reaction of a ^{48}Ca beam and implanted into a $CeBr_3$ detector, leading to the population of states in ^{37}Si. The 68-keV isomer was directly populated in the β-delayed one neutron emission decay of implanted ^{38}Al ions. Ancillary detector arrays comprising HPGe and $LaBr_3$(Ce) detectors were employed for the detection of β-delayed γ rays. The choice of detectors was driven by their excellent energy and timing resolutions, respectively.

The β-γ timing method was utilized to measure the half-life of the new isomeric state in ^{37}Si. This dissertation also discusses other timing techniques employed to search for and characterize isomeric states following β decay of implanted ions. Notably, the half-life of the newly observed $(7/2^-_1)$ isomeric state in ^{37}Si was measured to be 9.1(7) ns. The half-life of the previously observed closely-lying $(3/2^-_1)$ state at 156 keV was determined to be 3.20(4) ns, consistent with previously reported values. Reduced ground-state transition probabilities associated with the γ-ray decay from these excited states were in agreement with results obtained from shell model calculations.

In addition to the investigation of isomeric states in ^{37}Si, isomeric 0^+ states in ^{34}Si and ^{32}Mg nuclei belonging to the $N = 20$ "island of inversion" were characterized and searched for, respectively. The isomeric 0^+ state in ^{34}Si was populated following the β decay of implanted ^{34}Mg ions and its ^{34}Al daughter nucleus. Similarly, the 0^+ state in ^{32}Mg was searched for via the β-delayed one neutron emission decay of implanted ^{33}Na ions.

DEDICATION

Dedicated to my parents, Abiodun Emmanuel Ogunbeku and Adenike Abigail Ogunbeku. I love you both very much.

ACKNOWLEDGEMENTS

I have been fortunate to cross paths with numerous remarkable individuals and forge countless invaluable connections throughout this journey. So many people have supported and encouraged me in various ways, and I am immensely grateful. Attempting to compile an exhaustive list of names would be a monumental task, and I fear that I may unintentionally omit some. Therefore, I begin this acknowledgment by expressing my deepest gratitude to every single person that has shown me kindness during this phase of my life. Thank you so much. It indeed does take a village!

Dr. Benjamin Crider, I cannot thank you enough for being the very best advisor that I could ask for. I am grateful for your unwavering support, guidance, and advocacy throughout this remarkable journey. Your mentorship and friendship have significantly influenced my academic, professional, and personal growth. Your instrumental role in facilitating my assignment at FRIB has had a profound impact on my life, even shaping the trajectory of my post-graduate school journey. I am deeply grateful to you and your family for your kindness to me.

Dr. Sean Liddick, I extend my heartfelt thanks for your invaluable contributions to my academic journey, for being an exceptional co-advisor, and for accepting me into the beta decay group at FRIB. The positive experience of working with you is etched into the back of my mind. I am profoundly grateful for your time, mentorship, support and patience with me over the years. Thank you for challenging me to be a better scientist and more importantly, a better person.

Dr. Jeff Winger, Dr. Dipangkar Dutta, and Dr. Gautam Rupak Lan Tai Moong, my sincere appreciation goes to each of you for generously agreeing to serve on academic committee. I have found your profound insights and guidance vital throughout my academic journey. Your commitment to lending your time and expertise has played a key role to the success of my research. Dr. Winger, I am especially grateful for your significant contribution to my journey, particularly during my final year in this program.

My gratitude goes to my colleagues in the beta decay group at FRIB and my research group at Mississippi State University. Your support and collaboration mean a lot to me. Special thanks to all my post-doctoral mentors whose guidance and support continue to play a huge role in the advancement of my career. You all have become lifelong friends and I am all the better for it. My gratitude goes to the scientists and collaborators involved in the experiment that forms the bulk of my thesis which was supported by the National Science Foundation under Grant No. PHY-1848177 (CAREER).

Thank you to my parents and siblings, as well as my extended family, friends and all my loved ones. I offer my deepest gratitude to my Heavenly Father for never forsaking me, and for ordering my steps.

Thank you all for being my village!

TABLE OF CONTENTS

LIST OF TABLES

LIST OF FIGURES

CHAPTER I

INTRODUCTION

1.1 The Nucleus and Magic Numbers

The nucleus, which exists within every atom, is characterized by the number of protons, Z, and the number of neutrons, N. Z defines individual elements and their chemical properties, as well as the number of electrons in a neutral atom. The mass number, A, represents the total number of nucleons (protons and neutrons) in a nucleus. The nucleons are held together in the nucleus by the strong, short-ranged nuclear force, which determines what combination of protons and neutrons can form a bound nucleus. While the strong force has not yet been fully described by current microscopic models of nuclei due to their complexity, reproducing experimentally measured properties of the nucleus can improve the predictive power of such models. This endeavor begins with one of the earliest observations that contributed to the notion of the nuclear shell structure — the appearance of "magic numbers".

One-neutron separation energies, S_n, can be used as a tool to demonstrate the existence of the so-called magic numbers in nuclei. The distribution of one-neutron separation energies for even-even nuclei over varying neutron number, N, is shown in Figure 1.1(a). S_n is the energy required to remove a single neutron from a nucleus and is given by

$$S_n(A, Z) = BE(A, Z) - BE(A - 1, Z) \tag{1.1}$$

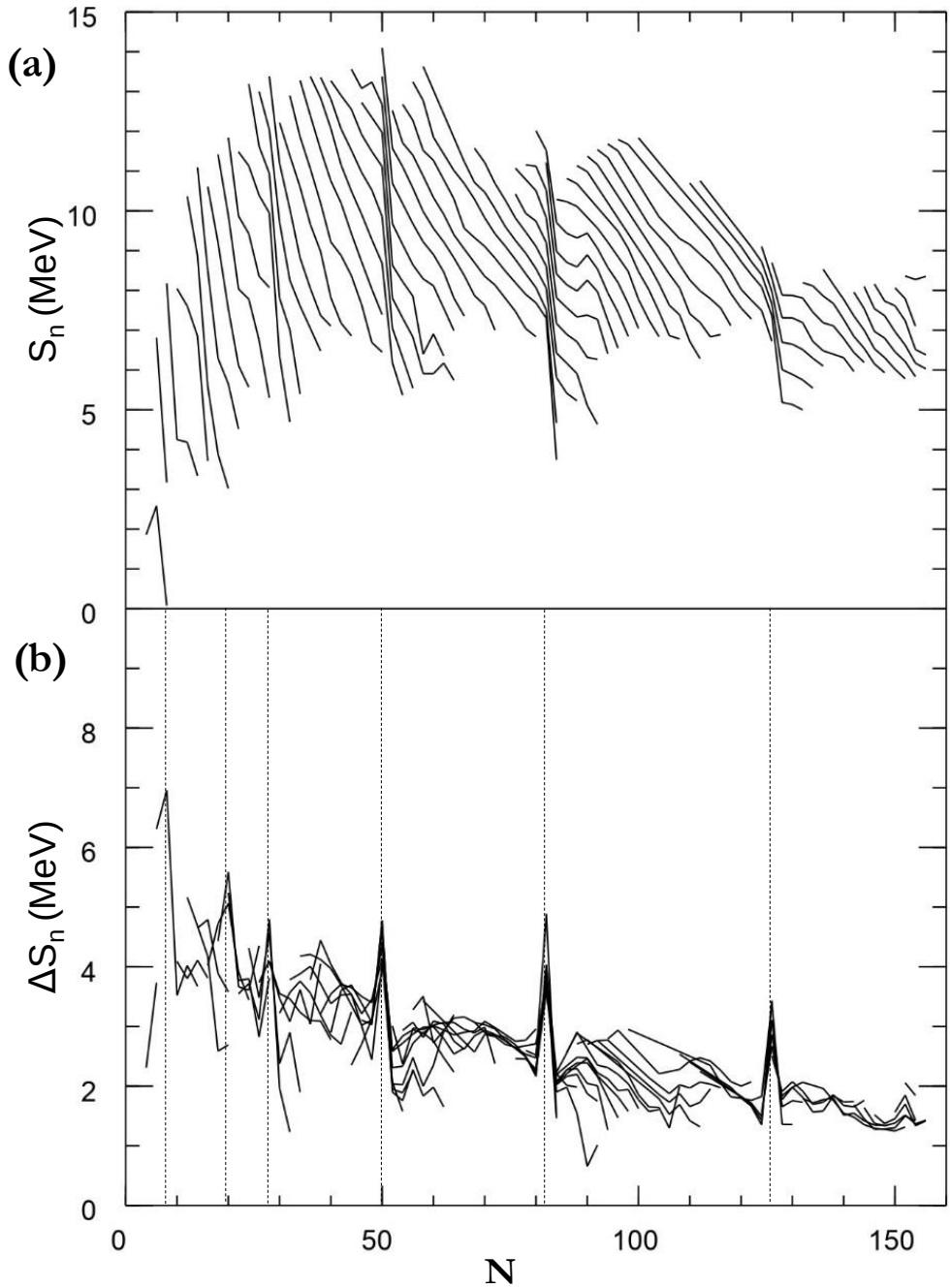

Figure 1.1: **(a)** One-neutron separation energies as a function of N for even-even nuclei. **(b)** Differential one-neutron separation energies as a function of N for even-even nuclei. The vertical lines represent magic numbers 8, 20, 28, 50, 82 and 126, associated with spikes in ΔS_n followed by a drastic drop, corresponding to enhanced stability at shell closures. This figure is adapted from Ref. [7].

where BE represents the binding energy of a nucleus with A nucleons, and Z is the atomic number. The discontinuities in S_n values after magic neutron numbers, 2, 8, 20, 28, 50, 82 and 126 is comparable to the sudden drops in ionization energy observed for atoms as a function of the proton number, Z, after the filling of electronic shells. The Z values corresponding to the ionization energy values just before the discontinuities represent magic Z numbers. Atoms with such magic Z numbers are referred to as noble gases which are known to exhibit enhanced stability because of their closed electronic configurations. Such analogy remains true for the nuclear shell where discontinuities in S_n (S_p, the one-proton separation energy) are similarly observed after magic neutron (proton) numbers. In this case, however, the discontinuities are better highlighted when considering the differential one-neutron separation energy as a function of neutron number, N, as shown in Figure 1.1(b) for even-even nuclei. The differential one-neutron separation energy, ΔS_n is the difference between the one-neutron separation energy, S_n of neighbouring nuclei along an isotopic chain, expressed as

$$\Delta S_n = BE(A, Z) - BE(A-1, Z) - [BE(A+1, Z) - BE(A, Z)] \tag{1.2}$$

where BE is the binding energy of a nucleus with A nucleons and Z protons, where the atomic number is the same along isotopic chains of interest.

1.2 The Nuclear Shell Model

The development of the nuclear shell model can be traced back to the need to predict experimentally observed magic proton and neutron numbers characteristic of stable nuclei. In the mean-field approximation of the shell model, the behavior of an independent or single nucleon is considered with the assumption that it is affected by a mean central potential due to other nucleons in the nucleus.

Single-particle eigenstates or orbitals are characterized by their energies and quantum numbers. The single-particle eigenstates and energies are obtained by solving the Schrödinger equation that describes the behaviour of a nucleon within the given mean potential. The energies of the single-particle eigenstates represent the allowed energy levels that the particle can occupy. These energy levels determine the stability and behavior of the particle within the system. Three mean potentials from which single-particle states have been obtained when solving the Schrödinger equation are presented in Figure 1.2.

As shown in Figure 1.2, the nuclear potential is not well described by the Harmonic Oscillator (HO) and Woods-Saxon (WS) potentials, as they are unable to reproduce experimentally observed magic nucleon numbers beyond $N, Z = 20$. This limitation was circumvented when Mayer [38], and Haxel, Jensen and Suess [23] independently suggested the addition of a spin-orbit coupling term to the WS potential, consequently expressed as

$$V_{LS}(r) = -V_{LS}\frac{d}{dr}\left(\frac{1}{1+e^{(r-R_0)/a}}\right)\left(\vec{l}\cdot\vec{s}\right), \tag{1.3}$$

accounting for the tendency of relativistic particles to align their orbital angular momenta, $\vec{l}$ and spins or intrinsic angular momenta, $\vec{s}$, and resulting in the removal of degeneracy of single-particle states according to the total angular momentum, $j = l \pm s$, where $s = 1/2$ for protons and neutrons, being fermions. With the addition of the spin-orbit coupling term, experimentally observed magic nucleon numbers are accurately reproduced, represented by the large gaps separated by the magic N numbers in Figure 1.2. Each single-particle state is represented by the notation $nl(2j)$ where the radial quantum number $n = 0, 1, 2, 3, ...$ corresponds to the number of radial nodes in the wavefunction; and the orbital angular momentum quantum number, $l = 0, 1, 2, 3...$, using the corresponding spectroscopic symbols $s, p, d, f...$, respectively. Each single-particle state has

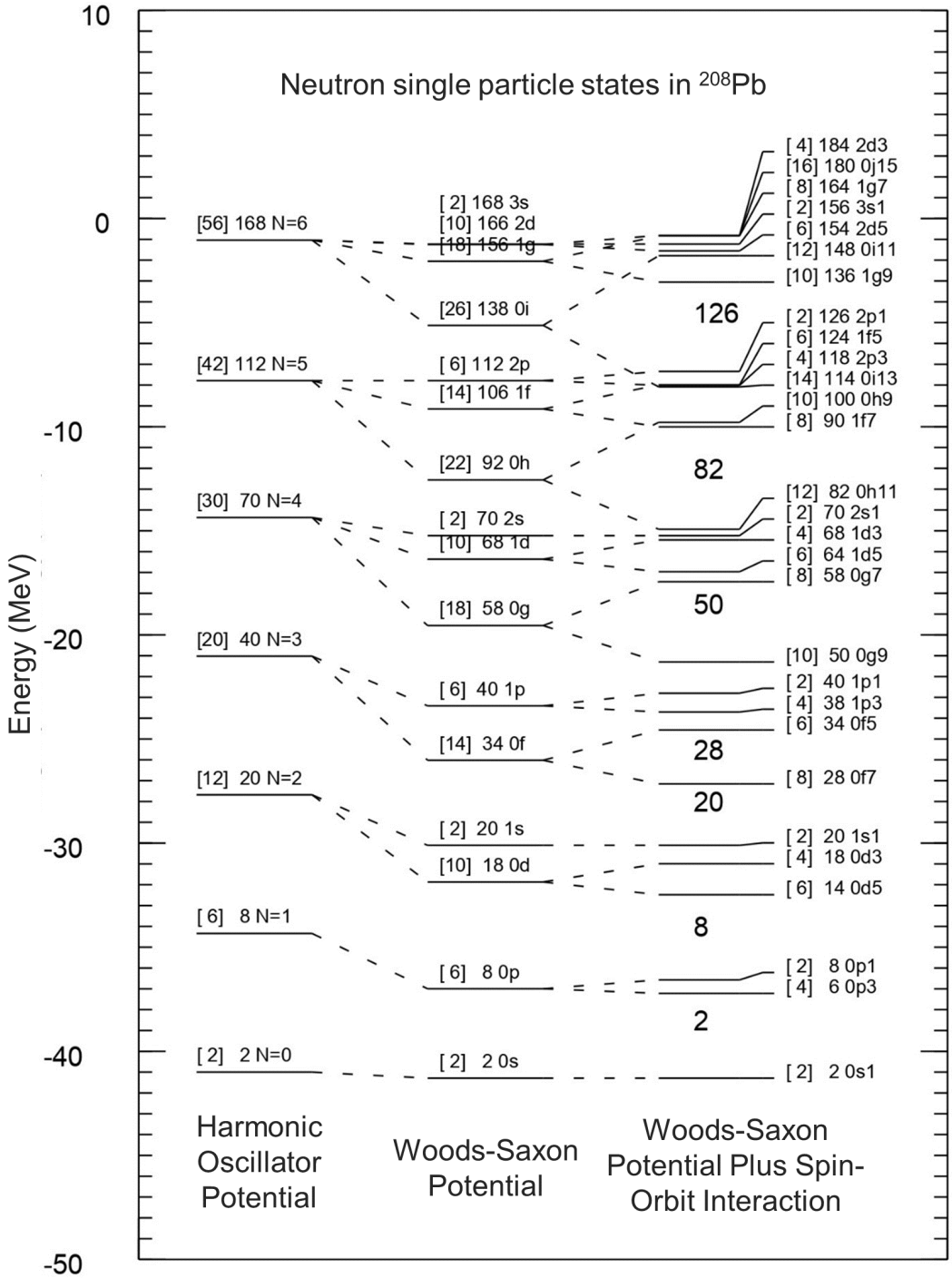

Figure 1.2: Neutron single-particle states in ^{208}Pb calculated using the Harmonic Oscillator potential (left), Wood-Saxon potential (middle), and Wood-Saxon potential with the spin-orbit coupling term (right) adapted from Ref. [7]. Individual levels are characterized by their occupancy in square brackets to the left, a cumulative occupancy in the middle and quantum numbers, $N = 2n + l$; n, l; and $n, l, 2j$ on the right for each potential.

$2j + 1$ substates or projections of the angular momentum from $m_j = -j, ..., 0, ..., +j$; such that each j state can contain a maximum of $2j + 1$ nucleons. The addition of the spin-orbit coupling term causes states with parallel coupling of l and s (larger j values) to be lower in energy than states with an antiparallel configuration. Moreover, the spin-orbit force induces a splitting of the j states, leading to significant energy differences and the formation of large energy gaps.

The independent particle model is particularly sufficient for predictions about the ground states of a broad range of nuclei but begins to fail when nuclei with extreme isospins or large N to Z ratios are considered.

1.3 The Interacting Shell Model

Over the years, nuclear shell models that allow for the inclusion of interactions between multiple valence particles have been established, resulting in the enhancement of the predictive capabilities of theoretical models of the nucleus. Limitations due to computational capabilities arise in solving the Schrödinger equations for nucleons in large nuclei, requiring the construction of a truncated or simplified model space. A typical model space is made up of a closed or inert core consisting of completely filled proton and neutron shells and a valence space, within which valence nucleons interact via the nucleon-nucleon (NN) or residual interaction, which is not considered in the independent particle model.

The single-particle energy (SPE) of every orbital with angular momentum j in the valence space and the two-body matrix elements (TBMEs) that model the residual interaction between nucleons in the valence space generally make up the input parameters for the shell model space. Specifically, the SPE is given by the kinetic energy and the effects of the closed core on each orbit with angular momentum j in the valence space [51], and taken from experimental data. On the

other hand, the TBMEs are derived from comparing and adjusting nuclear properties like binding energies, excitation energies and transition probabilities to experimental data in a certain region of the nuclear chart, and can be written as

$$< j_1 j_2 \mid V_{res} \mid j_3 j_4 >_{JT} \tag{1.4}$$

where j_1, j_2, j_3 and j_4 represent the angular momenta of the orbits occupied by the nucleons and V_{res} is an effective interaction between the nucleons. The individual angular momenta couple to a total angular momentum, J and isospin, T. It should be noted that all possible combinations of j's must be accounted for, such that the wavefunction of a state will be a linear combination of all possible configurations of nucleons in a model space.

1.4 The diminishing shell gap at $N = 28$

A diminished shell gap at $N = 28$ allows for energetically favored cross-shell excitations in exotic nuclei in the region where Z and N are very different. Such excitations result in the creation of states with intruder configuration which compete with, and exhibit structural differences from states characterized by normal, closed-shell configurations. Notably, these states with intruder configuration manifest at low excitation energies, and in some cases, become the ground state, as observed in neutron-rich isotopes near the $N = 20$ "island of inversion" [25]. The observation and characterization of these states that appear at low energies can provide more information on the microscopic structure of the nuclei in which they appear and additional insight into shell evolution along isotopic chains as nuclei become more exotic.

The first indication of the disappearance of the $N = 28$ shell gap was observed in ^{44}S, where a low excitation energy of 1297(18) keV was measured for the 2^+_1 state, characterized by a large quadrupole

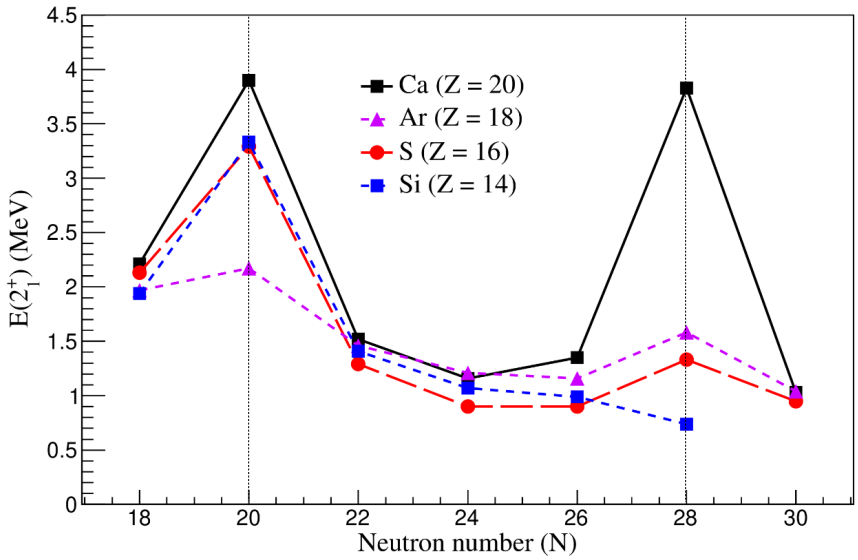

Figure 1.3: Experimental excitation energies of the first 2^+ states in Ca, Ar, S, and Si isotopes from $N = 20$ to $N = 28$. Data taken from Ref. [55].

transition strength, $B(E2; 0^+_{g.s.} \rightarrow 2^+_1) \uparrow$[1] of 314(88) $e^2\text{fm}^2$ [22], different from experimental signatures of high 2^+_1 energies and low $B(E2) \uparrow$ values for good shell closures. A similar evidence in the downward trend of 2^+_1 excitation energies has been established along the $N = 20$ up to $N = 28$ chains of even-even isotones below ^{48}Ca as visually represented in Figure 1.3. The sharp increase in the $E(2^+_1)$ for Ca isotopes with magic neutron numbers $N = 20$ and $N = 28$ observed relative to their neighbouring even-even isotopes in Figure 1.3 becomes inconsistent for the Si and S isotopes as they become more exotic. It can be inferred that both S and Si exhibit properties of good shell closures at $N = 20$, but the magicity at $N = 28$ disappears. This is primarily due to the monopole term of the tensor force component of NN interactions which drives the collapse and subsequent disappearance of the magic nature of classical shell gaps and the appearance of new

[1]In contrast to Coulomb excitation measurements, the notation, $B(E2; J_i \rightarrow J_f) \downarrow$ is used for electromagnetic transitions and relevant to the work presented in this dissertation. Here, J_i and J_f represent the higher- and lower-lying states, respectively. $B(E2) \downarrow$ values can be obtained from $B(E2) \uparrow$ strengths from Coulomb excitation measurements using the relation: $B(E2; J_i \rightarrow J_f) \downarrow = \frac{2J_i+1}{2J_f+1} B(E2; J_f \rightarrow J_i) \uparrow$.

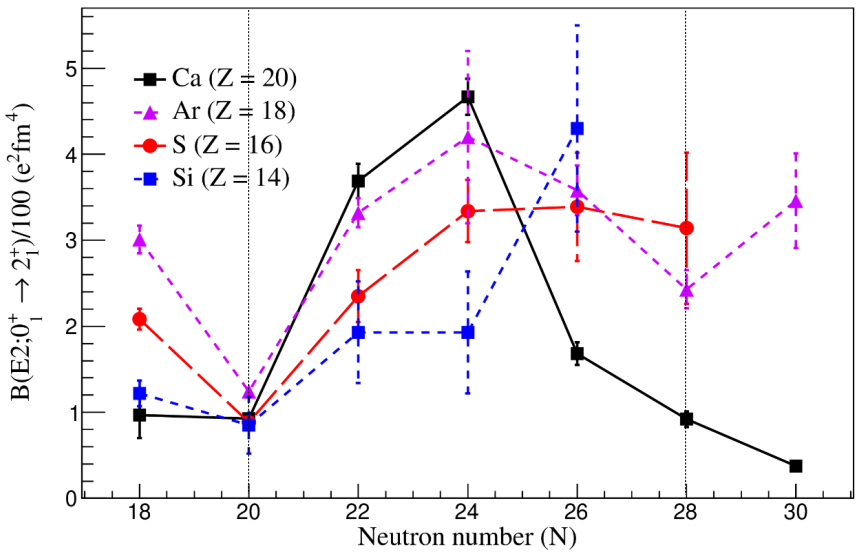

Figure 1.4: Experimental $B(E2; 0^+_{g.s.} \rightarrow 2^+_1)$ strengths for the same set of isotopes shown in Figure 1.3. Data taken from Ref. [55].

ones[49, 51, 48]. In terms of relevance to this dissertation, the neutron $0f_{7/2}$ orbit gets filled as a progression is made from $N = 20$ to $N = 28$. As discussed in Ref. [51], the tensor force, simply taken as the exchange of $\pi + \rho$ mesons, will induce a repulsion between the neutron $0f_{7/2}$ orbit $(j'_>)$ [2] and the proton $0d_{5/2}$ orbit $(j_>)$, and an attraction between the neutron $0f_{7/2}$ orbit $(j'_>)$ and the proton $0d_{3/2}$ orbit $(j_<)$. The interplay between the repulsion and attraction caused by the tensor force leads to the reduction of the energy gap between the neutron $0f_{7/2}$ $(j'_>)$ and proton $0d_{5/2}$ $(j_>)$ orbits and enhances the energy gap between the neutron $0f_{7/2}$ $(j'_>)$ and proton $0d_{3/2}$ $(j_<)$ orbits, as depicted in Figure 1.5. This results in the reduction of the $Z = 14$ sub-shell gap relative to ^{34}Si.

In the same vein, the removal of protons will weaken the attractive force between the proton $0d_{3/2}$ orbit $(j_<)$ and neutron $0f_{7/2}$ orbit $(j'_>)$ relative to ^{48}Ca. This weakening occurs because the presence of protons in the $0d_{3/2}$ $(j_<)$ orbit enhances the attractive interaction with the neutron $0f_{7/2}$

[2]For a neutron orbit, j', neutrons are either in $j'_> = l + 1/2$ or $j'_< = l - 1/2$, while protons are either in orbit $j_> = l + 1/2$ or $j_< = l - 1/2$.

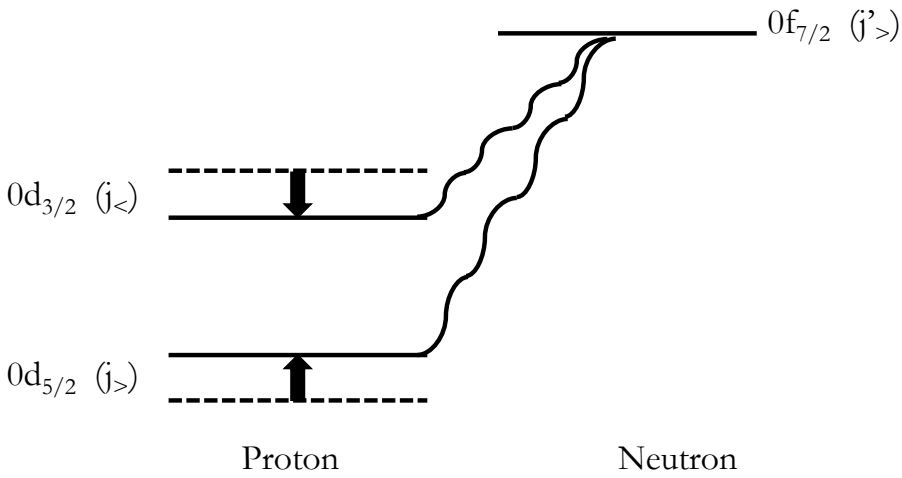

Figure 1.5: Schematic figure illustrating the effects of the tensor force on the neutron and proton orbits, adapted from Ref. [51].

($j'_>$) orbit. Moreover, the attractive force between the proton $0d_{3/2}$ ($j_<$) orbit and neutron $1p_{3/2}$ ($j'_>$) orbit is also weakened as protons are removed from the $0d_{3/2}$ ($j_<$) orbit. However, the repulsive force between the proton $0d_{3/2}$ orbit ($j_<$) and neutron $1p_{3/2}$ orbit ($j_<$) results in an enhancement of the energy of the neutron $0f_{7/2}$ orbit such that the $N = 28$ gap (between the neutron $0f_{7/2}$ and $1p_{3/2}$ orbits) is reduced.

The narrowing of the $Z = 14$ and $N = 28$ gaps result in enhanced excitations across the gaps such that the development of collectivity and deformation is favored in such nuclei. This is manifested in the observation of 2^+_1 states with low excitation energies and large quadrupole transition probabilities, and in some cases, coexisting spherical and deformed 0^+ states [18, 26, 52, 61]. As shown in Figure 1.4, the $B(E2)$ strength increases along the S and Si isotopic chains as $N = 28$ is approached, compared to the Ca and Ar isotopic chains.

1.5 Investigation: Low-lying isomers in exotic Odd-A Si isotopes

Low-lying excited states are observed in odd-A Si isotopes approaching $N = 28$. The $(3/2^+_1)$ state at 973.8(30) keV in ^{35}Si, with a half-life of 5.9(6) ns [46] decays to the excited $(3/2^-_1)$ state at 909.95(23) keV ($T_{1/2} = 55(14)$ ps) [67] and $(7/2)^-$ ground state. In contrast, the $(3/2^+_1)$ states in ^{37}Si and ^{39}Si decay by a fast $E1$ to the $(5/2^-)$ ground states and excited $(3/2^-_1)$ states which progressively become lower in energy. These $(3/2^-_1)$ states, along with the $(7/2^-_1)$ states in ^{37}Si and ^{39}Si, are predicted to be nanosecond isomers [67, 66] as illustrated in Figure 1.6.

The $(3/2^-_1)$ and $(7/2^-_1)$ states were established in the level scheme of ^{37}Si in a β^- [65, 4] and β^-n [65] decay experiment of ^{37}Al and ^{38}Al, respectively. The structure of ^{37}Si was also investigated in a ^{9}Be(^{38}Si, ^{37}Siγ) reaction which led to the identification of the 156-keV $(3/2^-_1)$ state as a nanosecond isomer with a reported half-life of 3.0(7) ns [67]. Although the $(7/2^-_1)$ state was not experimentally observed in Ref. [67], shell model calculation results in the same work predicted it to be a low-lying nanosecond isomer in ^{37}Si, alongside the $(3/2^-_1)$ state.

In this study, the isomeric states in ^{37}Si were investigated using β-decay and γ-ray spectroscopy. The half-lives of these states were determined using both β-γ and β-γ-γ measurement techniques. Additionally, their reduced ground-state transition probabilities were extracted and compared to theoretical predictions. The comparison between the experimental and theoretical results allow for inferences on the shell structure of the exotic ^{37}Si nucleus, as discussed in Chapter IV of this dissertation. Furthermore, the 0^+_2 states in ^{34}Si and ^{32}Mg were investigated using double-pulse and β-γ-γ half-life measurement techniques, discussed in Chapter V of this dissertation.

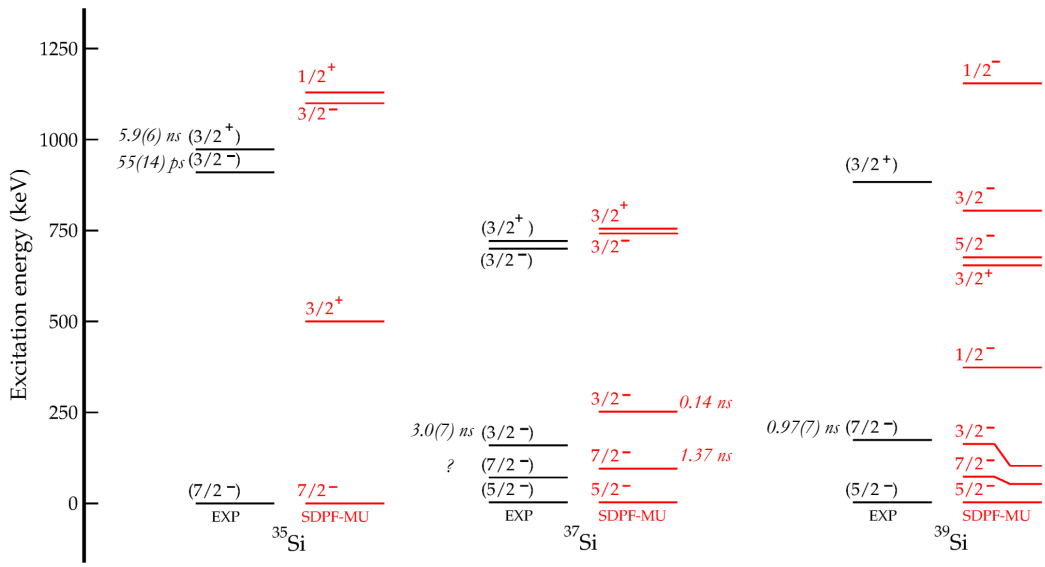

Figure 1.6: Experimental and theoretical level schemes for low-lying states in ^{35}Si, ^{37}Si, and ^{39}Si, including predicted nanosecond isomers in ^{37}Si and ^{39}Si. Experimental half-life data for isomers in ^{37}Si and ^{39}Si are from Ref. [67], while data for the $(3/2^+_1)$ and $(3/2^-_1)$ states in ^{35}Si are from Ref. [46] and Ref. [67], respectively. Theoretical half-life values are also included in red.

CHAPTER II

THEORETICAL BACKGROUND

2.1 Radioactivity

Of the approximately 3000 naturally occurring or artificially produced nuclei that we have some measurable information about, only about 300 are stable. The remaining majority, on the other hand are radioactive and undergo various decay processes. After undergoing radioactive decay, a parent nucleus transforms into a daughter nucleus with higher binding energy. The difference in binding energy determines the types of decays that can occur based on energy considerations, and any excess energy is converted into the kinetic energy of the resulting decay products. Common radioactive decay types include α, β and γ decay. Single and multiple proton or neutron emission is also possible in nuclei that lie close to the proton (neutron) drip line while heavy neutron-rich nuclei split roughly into half via spontaneous fission (SF).

A decay process can be characterized by an associated decay rate, dN/dt, expressed as

$$\frac{dN}{dt} = -\lambda N \tag{2.1}$$

where λ is the decay constant. The solution to Eq. 2.1 is given by

$$\frac{N}{N_0} = e^{-\lambda t} \tag{2.2}$$

where N is the number of nuclei remaining in a sample at time t, and N_0 is the number of nuclei in the sample at $t = 0$. The time t when $N/N_0 = 1/2$ is known as the half-life, $T_{1/2}$. It can be related to the decay rate, λ as

$$T_{1/2} = \frac{\ln 2}{\lambda}. \tag{2.3}$$

Isomeric states characterized in this dissertation were populated in the β decay of radioactive parent nuclei. Subsequent sections will delve into concepts associated with β decay.

2.2 β Decay

The majority of the known radioactive nuclei lie in regions where β decay is the dominant decay mode for such nuclei to become more stable [33]. β-decay spectroscopy is important for investigating and understanding the nuclear structure of exotic nuclei with large neutron number to proton number imbalance. Experimental measurements of observables such as β-decay half-lives, branching ratios, as well as characteristics of states populated via β decay offer insights into the structure of these nuclei. β decay involves the conversion of a proton (neutron) into a neutron (proton), such that a nucleus with mass number A is converted to another nucleus with the same A but differing N (Z). The value of A being kept constant indicates that successive β decays occur along an isobaric chain.

2.2.1 β-Decay Modes

Three different decay modes, β^-, β^+ and electron capture (EC) are all classified as β decays and are expressed as follows:

$$\beta^-: {}^{A}_{Z}X_N \rightarrow {}^{A}_{Z+1}Y^{+}_{N-1} + \beta^- + \bar{\nu_e} + Q_{\beta^-} \tag{2.4}$$

$$\beta^+: {}^{A}_{Z}X_N \rightarrow {}^{A}_{Z-1}Y^{-}_{N+1} + \beta^+ + \nu_e + Q_{\beta^+} \tag{2.5}$$

$$EC: {}^{A}_{Z}X_N + e^- \rightarrow {}^{A}_{Z-1}Y_{N+1} + \nu_e + Q_{EC}, \tag{2.6}$$

where the beta particle $\beta^{\pm}$ is an electron (β^-) or a positron (β^+), $\bar{\nu_e}$ is an electron anti-neutrino, ν_e is an electron neutrino and e^- is an atomic electron. β-decay Q-values are represented by Q_{β^-}, Q_{β^+} and Q_{EC} indicating the amount of energy released in each respective decay mode. Specifically, the Q-value is the mass-energy difference between the initial state in a parent nucleus and the final state in a daughter nucleus, which could be an excited state or the ground state. A β-decay mode is energetically feasible if the associated Q-value is positive.

β^- Decay

β^- decay mode is dominant in neutron-rich nuclei. The Q-value of a β^- decay can be calculated using the expression

$$Q_{\beta^-} = [M(A, Z) - M(A, Z + 1)]c^2 \tag{2.7}$$

where $M(A, Z)$ and $M(A, Z + 1)$ are the neutral atomic masses of the parent and daughter nucleus respectively and c is the speed of light. The decay energy, Q_{β^-} is shared among the recoiling daughter nucleus, the emitted β^- particle and electron antineutrino such that the energy of the of the emitted β^- particle can range from 0 to an endpoint value of Q_{β^-}. The emitted β^- particle can be detected due to it electromagnetically interacting with detector material, and depositing energy until it is fully stopped.

β^+ and EC Decay

β^+ and EC decay modes compete with each other in proton-rich nuclei. In β^+ decay, the decay energy is shared among the recoiling daughter nucleus, the emitted β^+ particle and the electron neutrino. The β^+ decay process requires that the mass-energy difference between the parent and daughter nuclei must be greater than the rest mass-energy of the emitted positron and an extra

electron ($2m_ec^2$ or 1022 keV), accounting for the neutral atomic masses of the parent and daughter nuclei. Similar to β^- decay, it is difficult to directly detect the recoiling daughter nucleus and electron neutrino due to their small mass-energy. However, the emitted positron can be detected using information from the energy it deposits within a detector medium as it interacts with the medium, gradually losing energy and slowing down. Commonly, two 511-keV γ rays emitted in opposite directions following the eventual annihilation of the positron with an electron after reaching thermal energies can also be detected in this decay mode.

EC decay becomes the dominant β-decay mode of a proton-rich nucleus when the decay energy is less than $2m_ec^2$ or 1022 keV. In EC decay, a proton in a nucleus captures an orbital electron (typically situated in the inner-most electronic shell or K shell), reducing the number of protons. This process is particularly relevant for heavier nuclei [33] and is accompanied with the emission of only one particle - a mono-energetic neutrino - whose energy depends on the binding energy of the captured electron and the initial and final states of the parent and daughter nucleus respectively. As described above, the electron neutrino has a negligible mass and does not interact with detector media due to its low weak interaction cross section. However, X-rays and Auger electrons emitted as a result of the reconfiguration of other electrons in outer shells filling the vacancy left behind by the captured electron can be tracked and used to identify EC decays.

2.2.2 β-Decay Selectivity

β-decay is a process that follows specific selection rules based on the conservation of angular momentum, denoted as l, during the transition from an initial state in the parent nucleus to a final state in the daughter nucleus. The parities of the states involved also play a role in determining the transition strengths.

Table 2.1: β-decay selection rules for allowed transitions ($l = 0$).

Transition Type	ΔJ	$\Delta\pi = (-1)^l$
Fermi	0 ($J_i = 0$ and $J_f = 0$)	No
Gamow-Teller	0, 1	No

Allowed transitions

If a β particle and neutrino are emitted with no angular momentum relative to the nucleus, such that $l = 0$, the decay is referred to as *allowed* and the selectivity of the decay will become dependent on the spin-alignment or coupling of the β particle and neutrino (both of which have intrinsic spins, $s = 1/2$). If the spins of the β particle and neutrino are anti-parallel in an *allowed* β decay such that their coupled spin is given by $S = 0$, the decay mode is referred to as a Fermi decay. For Fermi decay, the total change in spin, ΔJ between the initial and final states is 0, with no change in parity between the states as described in Table 2.1. If the spins of the β particle and neutrino in an *allowed* decay are parallel so that $S = 1$, the decay mode is referred to as a Gamow-Teller (GT) transition. In this mode, the possible values of ΔJ become 0 and 1. Since $\Delta J = 0$ is possible for both Fermi and GT decays, most decays will have a mixed Fermi and GT character, except when the initial and final states involved in the decay have spins of 0. These decay types are referred to as *superallowed* and have a high probability of occurrence.

Forbidden transitions

Forbidden transitions involve the emission of a β particle and neutrino with l values greater than 0, resulting in a higher degree of hinderance relative to *allowed* transitions. Each unit increase in the l value leads to an increase in the degree of forbiddeness of a transition by a factor of $\sim 3 \times$

10^{-4} [33]. Table 2.2 contains the selection rules for allowed and forbidden transitions for l values up to 3.

Branching ratios and $\log ft$ ***values***

β decay involves transitions that occur between an initial state in a parent nucleus to several final states in its daughter, such that all these transitions individually contribute to the total decay. It is therefore imperative to measure β-decay branching ratios (BR)[1] for transitions to the different final states in a daughter nucleus.

The decay rate, λ, in Eq. 2.3 may be rewritten for a decay into one daughter state, i such that

$$\lambda_i = \lambda \times BR_i \tag{2.8}$$

where BR_i is the branching ratio to state i. λ represents the total decay rate which can be written as the sum of decay rates to all possible final daughter states, such that

$$\lambda = \sum_i \lambda_i. \tag{2.9}$$

In the same vein, Eq. 2.3 can be rewritten for the partial half-life, $T_{1/2}^{partial,i}$ for the decay to state i as

$$T_{1/2}^{partial,i} = \frac{\ln 2}{\lambda_i}. \tag{2.10}$$

A comparative half-life, ft can be used to compare different β-decay transitions and measure their degree of forbiddenness. The Fermi function, f, is related to the Coulomb interaction between the daughter nucleus and emitted β particle and implicitly dependent on the atomic number Z of the daughter nucleus and the maximum (or endpoint) energy of the β decay; while t is the partial half-life in seconds. Since β-decay half-lives and their corresponding ft values span about 21

[1]The branching ratio is the fraction of decays that will occur through a specific decay channel.

Table 2.2: β-decay selection rules for allowed and forbidden transitions and associated $\log ft$ values adapted from Ref. [33].

Transition Type	l	ΔJ	$\Delta\pi = (-1)^l$	$\log ft$
Superallowed	0	0	No	2.9 - 3.7
Allowed	0	0, 1	No	4.4 - 6.0
First forbidden	1	0, 1, 2	Yes	6 - 10
Second forbidden	2	1, 2, 3	No	10 - 13
Third forbidden	3	2, 3, 4	Yes	≥ 15

orders of magnitude [64], the logarithmic ft value is widely used to conveniently characterize β decays.

The $\log ft$ values are also quite useful in roughly assigning spins and parities to nuclear states involved in β decay. Table 2.2 shows the correlation between $\log ft$ values and spin and parity change between an initial state in a parent nucleus and a final state in a daughter nucleus involved in β decay. Approximations for $\log ft$ values for specific types of β decay can be obtained using the graphs and nomographs developed by S. A. Moszkowski in 1951 [42]. A comprehensive review of $\log ft$ values for approximately 3,900 transitions is available in Ref. [64] and $\log ft$ values can be calculated using parent and daughter information from the $\log ft$ webpage provided by the National Nuclear Data Center (NNDC) [3].

2.2.3 β-delayed neutron emission

β decay in neutron-rich nuclei allows for a wide-ranging number of states including excited and ground states of a daughter nucleus to be populated. The access to such a wide range of states can be attributed to a very large Q-value window of the decaying neutron-rich nuclei. The large Q-value window coupled with relatively low neutron-separation energies, S_n, in these nuclei account

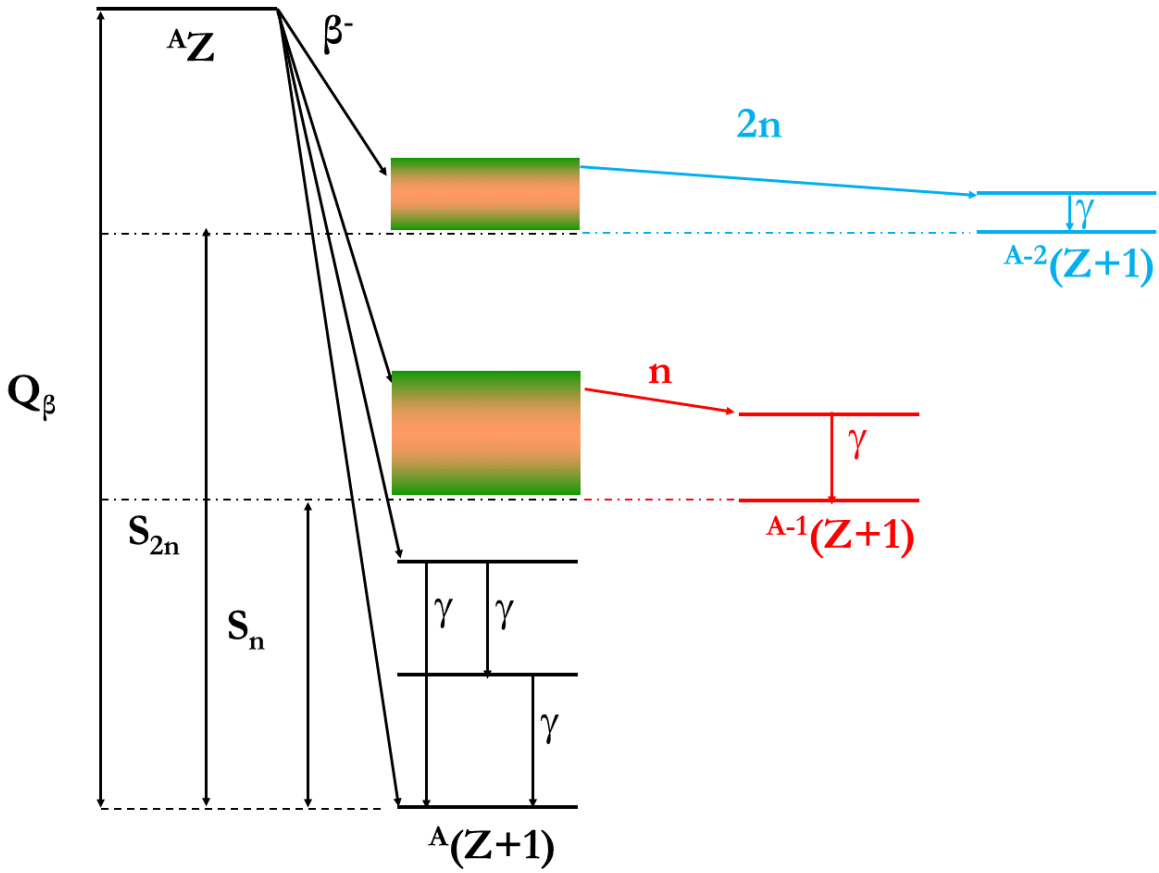

Figure 2.1: Schematics and energetics for β-delayed neutron emission channels

for large neutron-emission probabilities, P_n, and the possibility of β-delayed neutron emission. β-delayed neutron emission can be written as

$$ {}^{A}_{Z}X_N \rightarrow {}^{A-1}_{Z}X_{N-1} + n + \beta^- + \bar{\nu_e} + Q_n \tag{2.11} $$

where Q_n is the difference in the total energy between the initial and final states involved in the decay. With this logic, the neutron separation energy, S_n, is positive for all bound nuclei such that delayed neutron emission is impossible from the ground state.

A β-decay schematic showing decay channels up to two-neutron emission is shown in Figure 2.1. In the figure, a parent nucleus with mass number A and proton number Z decays via β^- and populates states in its daughter with the same A and an additional proton. Neutron-unbound states above the one-neutron and two-neutron separation energies, S_n and S_{2n} respectively, in the daughter are represented by the green and yellow bands. These states de-excite by competing γ-ray and neutron emissions, with neutron emission being the dominant mode of de-excitation. The Q-value for delayed emission of neutrons is explicitly dependent on the neutron-separation energies for the respective number of neutrons such that the maximum energy available for a β-delayed one-neutron or two-neutron emission decay becomes the difference between Q_β and S_n or S_{2n}, respectively. Due to the emission of a neutron, states that may not be directly accessible by β decay alone can be populated.

2.3 γ-ray Decay

γ-ray decay is the emission of excess energy in the form of electromagnetic radiation or photons associated with the de-excitation of higher-energy to lower-energy, and/or ground states states in nuclei. In this process, a nucleus releases excess energy while maintaining its atomic number, Z and neutron number, N. In this dissertation, γ rays of interest are observed following the population

of excited states in daughter nuclei in β^- and β-delayed one-neutron emission decays. They are referred to as β-delayed γ rays in subsequent chapters.

In γ-ray decay, a single nucleus undergoes a transition between two states. The energy of the emitted γ ray, denoted as E_γ, is equal to the energy difference (ΔE) between the initial and final states. While the nucleus also acquires recoil kinetic energy (T_r), this contribution is typically very small compared to ΔE and can be neglected. As a result, E_γ is approximately equal to ΔE.

A γ-ray transition connecting two nuclear states is characterized by its conserved parity π and angular momentum (or multipolarity) λ, such that it carries away an integer number of angular momentum in units of $\hbar$ (or $h/2\pi$). The conservation of angular momentum implies that the allowed values of λ will be given by

$$\mid J_i - J_f \mid \leq \lambda \leq J_i + J_f \tag{2.12}$$

where J_i and J_f are the spins of the initial and final states respectively. The minimum intrinsic spin that an emitted photon must carry is $1\hbar$, therefore, angular momentum $\lambda = 0$ is forbidden for single-photon emission. The effect of the conservation of parity implies that a γ-ray transition is restricted by

$$\pi_i \pi_f = \pi_\sigma (-1)^\lambda \tag{2.13}$$

where π_i and π_f are the parities of the initial and final states respectively and σ is the type of transition (electric or magnetic), with $\pi_{Electric} = 1$ and $\pi_{Magnetic} = -1$. Information from Eqs. 2.12 and 2.13 provide us with a set of allowed transitions for given γ-ray decay types, with λ increasing by 2 for the next allowed multipolarites for electric and magnetic transitions.

The characteristics of common transition types relevant to the work in this dissertation are provided in Table 2.3.

Table 2.3: γ-ray transition types and their associated multipolarities and parities. The transitions are referred to as 2^{λ} poles.

Transition Type ($\sigma\lambda$)	Name	$\Delta\pi$
E1	Electric dipole	Yes
M1	Magnetic dipole	No
E2	Electric quadrupole	No
M2	Magnetic quadrupole	Yes
E3	Electric octupole	Yes
M3	Magnetic octupole	No

2.3.1 γ-ray transition rates and reduced transition probabilities

The rate of the electromagnetic transition between two states is given by

$$W_{M_i,M_f,\mu} = \left(\frac{8\pi(\lambda+1)}{\lambda[(2\lambda+1)!!]^2}\right)\left(\frac{1}{\hbar}\right)\left(\frac{E_\gamma}{\hbar c}\right)^{2\lambda+1} |< J_f M_f \mid O(\lambda)_\mu \mid J_i M_i >|^2 \tag{2.14}$$

where λ is the multipolarity, c is the speed of light, E_γ is the energy of the transition, μ is z-projection of λ, $< J_f M_f \mid O(\lambda)_\mu \mid J_i M_i >$ is the nuclear matrix element of the electromagnetic transition between the initial state $\mid J_i M_i >$ and final state $< J_f M_f \mid$. M_i and M_f are the initial and final magnetic substates which are averaged over. The sum over allowed electric and magnetic transition operators is given by $O(\lambda)_\mu$.

Experimental measurements are not sensitive to magnetic substates M_i and M_f, so $< J_f M_f \mid O(\lambda)_\mu \mid J_i M_i >$ can be replaced with the reduced transition probability, $B(\sigma\lambda; J_i \rightarrow J_f)$, expressed as

$$B(\sigma\lambda; J_i \rightarrow J_f) = \frac{|< J_f \mid\mid O(\sigma\lambda) \mid\mid J_i >|^2}{2J_i + 1} \tag{2.15}$$

where $|< J_f \mid\mid O(\sigma\lambda) \mid\mid J_i >|$ is the reduced transition matrix element.

For the scope of this study, $B(\sigma\lambda; J_i \rightarrow J_f)$ is interchangeable with $B(\sigma\lambda; J_i \rightarrow J_f)\downarrow$. The $\downarrow$ symbol signifies the direction of the electromagnetic decay from a higher-lying state with spin J_i

to a lower-lying state with spin J_f, as discussed in Section 1.4. The double bar in the expression of the reduced transition matrix element, $|< J_f \,||\, O(\sigma\lambda) \,||\, J_i >|$, signifies that the dependence of the transition matrix element on maagnetic substates and z-projection of λ has been removed, making the complex quantum mechanical calculations more manageable. The removal of this dependency is made possible by applying the Wigner-Eckart theorem to separate out the radial and angular parts of the matrix element and using the Clebsch-Gordan coefficients to handle the angular part.

2.3.1.1 Weisskopf single-particle estimates

The expression of the reduced transition probability in Eq. 2.15 is strongly dependent on nuclear models and quite complicated. It is therefore easier to extract estimates for $B(\sigma\lambda)$ within the single-particle limit by assuming that a γ-ray transition results from the change of a single nucleon inside a nucleus with uniform density and radius $R = R_0 A^{1/3}$, with $R_0 = 1.27 fm$ [41].

The Weisskopf single particle estimates for the reduced transition probabilities are given by

$$B_W(E\lambda) = \frac{1}{4\pi}\left(\frac{3}{\lambda+3}\right)^2 (1.2)^{2\lambda} A^{2\lambda/3} \ \mathrm{e^2fm^{2\lambda}} \text{ and} \tag{2.16}$$

$$B_W(M\lambda) = \frac{10}{\pi}\left(\frac{3}{\lambda+3}\right)^2 (1.2)^{2\lambda-2} A^{(2\lambda-2)/3} \ \mu_N^2 \mathrm{fm^{2\lambda-2}} \tag{2.17}$$

for electric and magnetic transitions, respectively. The nuclear magneton, μ_N, is denoted by

$$\mu_N = \frac{e\hbar}{2m_p c} = 0.105 e fm. \tag{2.18}$$

The relationship between transition rates and λ is inverse, resulting in lower-multipolarity γ-ray decays being favored for a given E_γ. For instance, when E_γ is 1000 keV, the rate of the subsequent allowed electric (magnetic) transitions with $\lambda+2$ is approximately seven orders of magnitude lower than the rate of the lowest allowed electric (magnetic) multipole with λ [7].

For the scope of this dissertation, the inverse relationship between the reduced transition probabilities of $M1$ and $E2$ transitions (in Weisskopf single-particle strength estimates) and the measured half-life, $T_{1/2}$ is given by

$$B(M1)(W.u.) = \frac{2.202 \times 10^{-5} BR}{(E_\gamma)^3 T_{1/2}(1+\alpha)} \text{ and} \tag{2.19}$$

$$B(E2)(W.u.) = \frac{9.527 \times 10^{6} BR}{(E_\gamma)^5 T_{1/2}(1+\alpha)} \tag{2.20}$$

respectively, where BR is the branching ratio for the transition of interest, E_γ is the energy of the transition in keV, $T_{1/2}$ is the half-life of the decaying state, and α is the internal conversion coefficient which can be estimated from Ref. [1]. It should be noted that the equations provided above consider only pure $M1$ and $E2$ transitions.

2.3.2 Mixed transitions and contributions to lifetimes

The electromagnetic decay of excited states can occur by a mixture of electric and magnetic multipole transitions such that Eq. 2.14 can be simplified to represent the total transition rate, W, as

$$W_{i,f} = \sum [W_{i,f}(E\lambda) + W_{i,f}(M\lambda)]. \tag{2.21}$$

As indicated in Section 2.3.1.1, in most cases, the lowest allowed multipole for a given transition is dominant. Therefore, when more than one transition type is allowed, the decay rate associated with the lowest allowed multipolarity normally becomes dominant over the next by several orders of magnitude. However, an exception exists for $M1$ and $E2$ transitions which can be strongly mixed. Mixed transitions must also be considered when extracting transition rates, W, for the

lowest allowed multipoles of electric and magnetic transitions, as both transition types may be equally important. A mixing ratio, δ, is necessary to to quantify this, with

$$\delta^2(E2/M1) = \frac{W_{E2}}{W_{M1}} \tag{2.22}$$

for the scope of this dissertation, considering a mixed $M1 + E2$ γ-ray transition.

A branching factor, b, can also be extracted for the individual transition types, with

$$b(M1) = \frac{W_{M1}}{W_{M1} + W_{E2}} = \frac{1}{1 + \delta^2} \text{ and} \tag{2.23}$$

$$b(E2) = \frac{W_{E2}}{W_{M1} + W_{E2}} = \frac{\delta^2}{1 + \delta^2} \tag{2.24}$$

such that partial lifetimes can be attributed to the transition types and their contributions to the decay lifetime can be quantified.

2.4 Internal conversion

Excited nuclear states may decay via internal conversion, which competes with γ-ray decay. An internal conversion decay is an electromagnetic interaction between a nucleus in an excited state and an atomic electron, resulting in the emission of the electron. The emitted electron is monoenergetic such that its energy, E_{IC} is represented by

$$E_{IC} = E_{transition} - e_{BE} \tag{2.25}$$

where $E_{transition}$ is the energy difference between the initial and final states involved in the decay, and e_{BE} is the binding energy of the ejected atomic electron.

The probability of internal conversion for a particular decay is called the internal conversion coefficient, α, and is given by

$$\alpha = \frac{\text{number of internal conversion decays}}{\text{number of } \gamma\text{-ray decays}} = \frac{\lambda_{IC}}{\lambda_\gamma} \tag{2.26}$$

where λ_{IC} and λ_{γ} are the partial decay constants for internal conversion and γ-ray decay, respectively. α can be estimated from Ref. [1].

The multipolarity, λ can be determined for a given internal conversion transition using the relative probabilities of emitting conversion electrons from different possible atomic shells, with the K-shell being the most dominant because of its proximity to the nucleus relative to other shells. Therefore, the total internal conversion coefficient, α_{total}, is the sum of the conversion coefficients of all available electronic shells such that

$$\alpha_{total} = \alpha_K + \alpha_L + \alpha_M + ... \tag{2.27}$$

The probability of internal conversion is directly proportional to the atomic number, Z of the excited nucleus and the multipolarity, λ of the transition; and inversely proportional to the decay energy. Consequently, internal conversion may be significant for low-energy transitions as well as transitions involving a large λ or Z. These relationships are established for approximate internal conversion coefficients for electric and magnetic transitions, with the formulas (adapted from Ref. [33])

$$\alpha(E\lambda) = \frac{Z^3\alpha_{EM}^4}{n^3}\left(\frac{\lambda}{\lambda+1}\right)\left(\frac{2m_ec^2}{E}\right)^{\lambda+5/2} \text{ and} \tag{2.28}$$

$$\alpha(M\lambda) = \frac{Z^3\alpha_{EM}^4}{n^3}\left(\frac{2m_ec^2}{E}\right)^{\lambda+3/2} \tag{2.29}$$

where n is the principal quantum number of the ejected electron, m_e is the mass of the electron, α_{EM} is the fine structure constant represented by $\left(\frac{e^2}{4\pi\epsilon_0}\right)\left(\frac{1}{\hbar c}\right)$ or $\frac{1}{137}$, and E is the energy of the transition.

2.5 Internal pair production

Internal pair production is another electromagnetic decay process alternative to γ-ray or internal-conversion electron emission. An electron-positron pair is created in internal pair production which is reserved for transitions with energies greater than 1022 keV. Excess energy is shared between the electron and positron as kinetic energy. The emitted positron will annihilate after slowing down in the detection materials and two 511-keV photons are emitted as secondary products of the interaction, in opposite directions. Internal pair production and internal conversion are less likely to occur compared to γ-ray decay, except in cases when the angular momentum available for a γ ray is 0, such that γ-ray emission is forbidden.

2.6 $E0$ transitions

As mentioned in Section 2.5, the competition between γ-ray decay and internal conversion or internal pair production becomes favorable for the latter two processes when $\lambda = 0$. A typical case is for transitions between two 0^+ states which can only proceed via internal conversion or internal pair production. These are known as electric monopole ($E0$) transitions [13]. It should be noted that γ-ray decay typically remains the dominant decay mode for transitions with the same spins that are greater than 0, as there are other possible higher-order λ values. The probability for an $E0$ transition to occur, $\lambda(E0)$, is given by

$$\lambda(E0) = \lambda_{IC}(E0) + \lambda_{\pi}(E0) = \frac{\ln 2}{T_{1/2}(E0)} = \rho^2(E0) \times [\Omega_{IC}(E0) + \Omega_{\pi}(E0)] \tag{2.30}$$

where $\lambda_{IC}(E0)$ and $\lambda_{\pi}(E0)$ are the partial transition probabilities for internal conversion and internal pair production, respectively, $T_{1/2}(E0)$ is the partial half-life for the $E0$ decay, $\rho^2(E0)$

is the electric monopole transition strength, and $\Omega_{IC}(E0)$ and $\Omega_{I\pi}(E0)$ are electronic factors for internal conversion and internal pair production, respectively.

$\rho^2(E0)$ is a dimensionless quantity that carries vital information about the nuclear structure. The experimental determination of $\rho^2(E0)$ is dependent on the measurement of absolute transition rates and calculation of electronic factors. $\Omega_{IC}(E0)$ and $\Omega_{I\pi}(E0)$ cannot be measured directly and are therefore calculated theoretically, independent of nuclear properties. They are dependent on the atomic number, Z and the transition energy, and are expressed in units of s^{-1}. Electronic factors can be obtained using the BrIcc conversion coefficient calculator [1].

CHAPTER III

EXPERIMENTAL SETUP

Experiments involving exotic isotopes far from β stability are almost exclusively produced in nuclear reactions between stable nuclei or their ions [53]. The experiment E16032 described in this thesis was conducted at the National Superconducting Cyclotron Laboratory (NSCL) [21] at Michigan State University with a primary goal to study isomeric states in neutron-rich nuclei located near the $N = 20$ "island of inversion" up to the $N = 28$ shell closure. These isomeric states were populated following the β decay of radioactive neutron-rich isotopes artificially produced in a projectile fragmentation reaction [70] between a stable 140-MeV/nucleon ^{48}Ca primary beam and a 642 mg/cm^2 -thick ^{9}Be target [40] at the Coupled Cyclotron Facility (CCF)[39, 41] of the NSCL. The reaction fragments were then delivered to the experimental end station as a secondary cocktail beam. Particularly for this dissertation, isomeric states in ^{32}Mg, ^{34}Si and ^{37}Si were populated following the β decay of their respective parent nuclei, and their isomeric decays were studied using fast-timing analysis. An overview of the experimental setup at NSCL is presented in subsequent sections of this chapter.

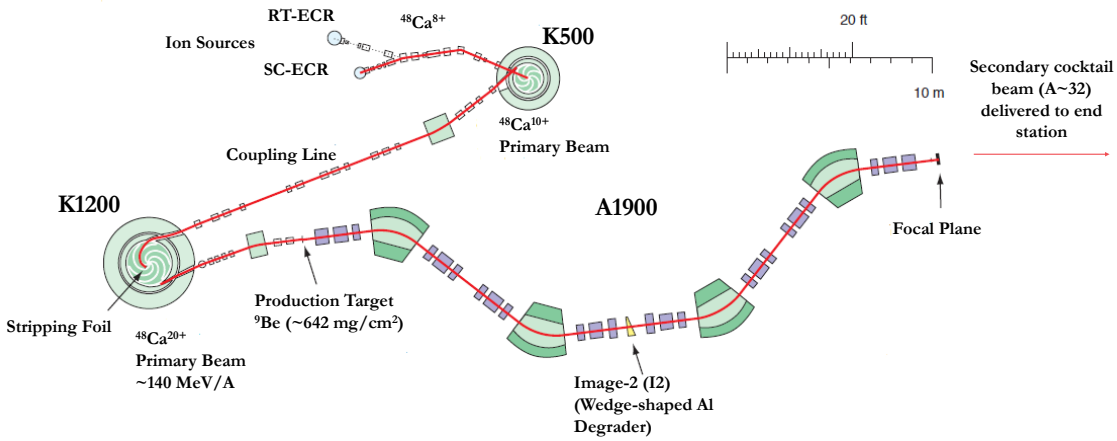

Figure 3.1: Schematic layout of the Coupled Cyclotron Facility at NSCL. The figure is adapted from Ref. [63] and modified to reflect settings for E16032.

3.1 Cocktail beam production and separation

A schematic layout of the CCF at NSCL is shown in Figure 3.1 with the K500 and K1200 cyclotrons highlighted as well as the A1900 fragment separator, all necessary for beam production and separation.

3.1.1 Production

A block of metallic ^{48}Ca was heated to produce vapor, then slightly ionized to a charge state of 8+ using the electron cyclotron resonance (ECR) technique [80]. The $^{48}Ca^{8+}$ ions were then selected using a magnetic dipole and extracted by an electric field to be sent to the K500 cyclotron. In the K500, the $^{48}Ca^{8+}$ ions were accelerated to energies of 12 MeV/nucleon and then transported and injected into the K1200 where they were fully stripped of their electrons to a higher charge state of 20+ and accelerated to a final energy of 140 MeV/nucleon. After acceleration, the ^{48}Ca

primary beam was impinged on a stationary 642 mg/cm^2-thick ^{9}Be target producing a wide variety of reaction products including stable and radioactive nuclei.

3.1.2 Separation

The A1900 — a large ion optical fragment separator — was used to select and guide nuclei of interest to the experimental end station using magnetic and electric separation techniques, eliminating unwanted nuclei. It consists of 4 dipole magnets which act on the nuclei like prisms act on different colors of light, by bending and spreading the beam particles according to their momentum to charge ratio. The magnets are arranged in a 45° reverse-bend geometry so that incoming and outgoing beams remain coaxial, and only some particles make it around each 45° turn. The A1900 also includes 24 quadrupole magnets arranged in eight groups of three to focus the beam, preventing further loss of nuclei. During E16032, the A1900 was tuned to optimize the production and implantation of ^{33}Na ions which the secondary cocktail beam was centered around, accounting for ~5% of the total transmitted ions.

Following the fragmentation reaction between the primary beam and the target, reaction products have nearly equal velocities, slightly lower than the velocity of primary beam [53]. In the first half of the A1900, before the I2 dispersive image as shown in Figure 3.1, nuclei are separated by means of momentum analysis such that the magnetic fields of the first two dipoles are tuned based on the magnetic rigidity, $B\rho$ of the nuclei. In accordance with Lorentz's law, the product of the magnetic field strength B and the radius of curvature ρ is directly related to the momentum p of a charged particle with charge q as it moves along a circular trajectory within the field. Mathematically, this relationship can be expressed as

$$B\rho = \frac{p}{q} = \frac{\gamma m v}{q} \tag{3.1}$$

where m and v are the mass and velocity of the particle, respectively, and γ is Lorentz or relativistic factor expressed as $\left(\sqrt{1-\frac{v^2}{c^2}}\right)^{-1}$ where c is the speed of light. In this half of the A1900, separation is dependent on the momentum to charge ratio, mv/q, given that the fragments have nearly equal velocities, v. The magnetic rigidity $B\rho$ was set to 4.8216 Tm in the first half of the A1900 for E16032.

Maximum dispersion of the beam occurred at the center of the A1900 where a 150 mg/cm^2 achromatic aluminum wedge-shaped degrader was located. At this stage, nuclei are dispersed according to the stopping power or rate of energy loss of the ions along the path length in the degrader as a function of Z^2. After the wedge, isotopes with different atomic number, Z will have different rigidities. This results in further separation using the last two dipole magnets in the second half of the A1900, optimized for centering ^{33}Na ions within the slits at the focal plane of the A1900. In this region, B_ρ was set to 4.78763 Tm. The slits at the focal plane allow for removal of additional unwanted fragments by controlling the momentum acceptance, $\Delta\rho/\rho$. For this experiment, a value of $\Delta\rho/\rho$ = 5.07% was selected. This choice aligns with the typical 5% range often employed in β-decay experiments, as it enables the maximum transmission of isotopes to the experimental end station.

3.2 The experimental end station

Figure 3.2 shows the configuration of detectors employed in the experimental end station, particularly highlighting their placement. Figure 3.3 presents a schematic representation of the detectors and materials the secondary cocktail beam would interact with, leading up to the point of implantation. Descriptions of each detector utilized in the experimental end station are provided in

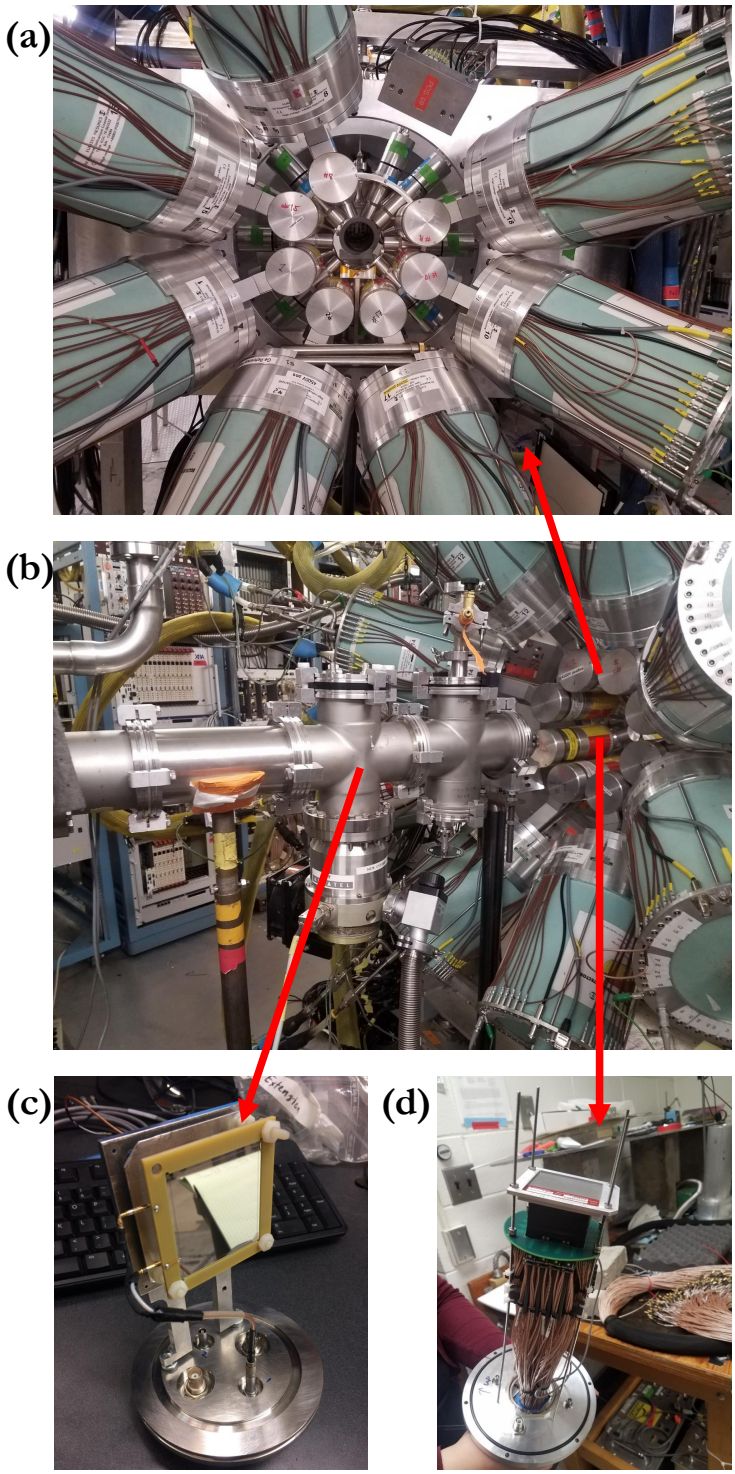

Figure 3.2: **(a)** Arrays of $LaBr_3$(Ce) and SeGA detectors positioned to surround the $CeBr_3$ implantation detector; **(b)** upstream portion of experimental end station; **(c)** a silicon PIN detector; and **(d)** the $CeBr_3$ implantation detector coupled to the PSPMT.

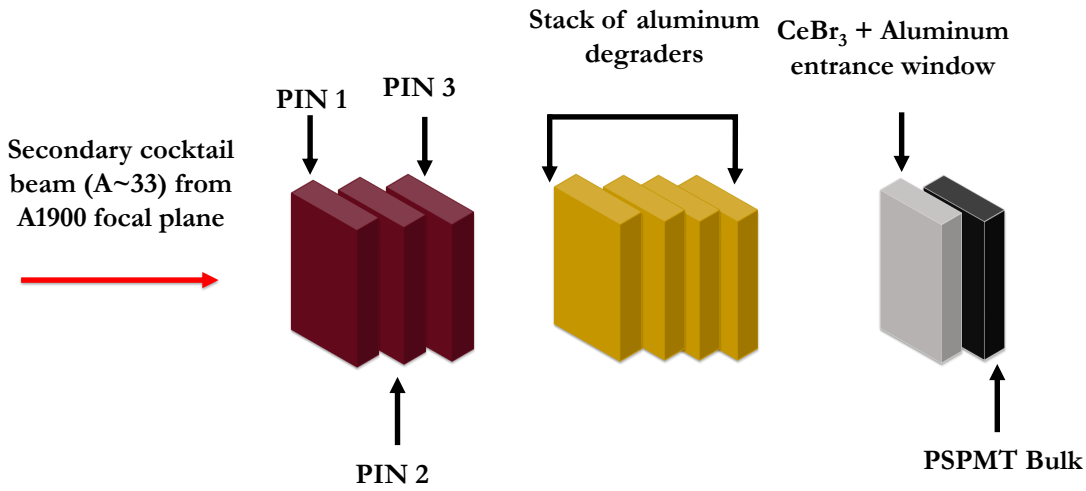

Figure 3.3: Schematic layout of E16032 experimental setup.

subsequent subsections, as outlined in Table 3.1. All events were read out using the NSCL Digital Data Acquisition System (DDAS) [57, 58].

3.2.1 Silicon PIN detectors

The secondary beam was delivered to the experimental end station as a cocktail beam centered around ^{33}Na. The first set of detectors that the secondary beam interacted with at the end station were 3 silicon PIN[1] detectors with respective thicknesses of 996 μm, 1041 μm and 503 μm. The detectors were placed approximately 1 m upstream of the $CeBr_3$ implantation detector within which ions were implanted.

3.2.1.1 Particle identification

Any of the PIN detectors can be used to identify fragments in the secondary beam on an event-by-event basis, but the first of the three was used in analysis discussed in this dissertation. Particle

[1]The Silicon PIN photodiode consists of an undoped intrinsic semiconductor region sandwiched between a p-type and an n-type semiconductor region.

Table 3.1: Experiment E16032 detector list.

Detector	Function	Notes
Si PIN ($\times$ 3)	Particle identification	ΔE - TOF
$CeBr_3$	Ion implantation, β-decay electron detection, decay - ion correlation, low-energy γ ray detection, fast-timing measurements	Optically coupled with electrically-segmented PSPMT
HPGe (x16)	β-delayed γ-ray detection	Arranged in beta-SeGA configuration
$LaBr_3$ ($\times$ 15)	β-delayed γ-ray detection, fast-timing measurements	

identification was carried out by taking the energy loss (ΔE) information through the first PIN detector and the time-of-flight (TOF) between the position-sensitive scintillator at the dispersive image of the A1900 fragment separator (I2) and the PIN detector. Figure 3.4 shows the raw particle identification (PID), i.e. ΔE versus TOF plot accumulated for the entirety the experiment, which ran for approximately 83 hours. In the plot, the horizontal rows of oval spots correspond to isotopic chains while the vertical rows correspond to the mass to charge ratio, A/q.

A closer examination of the PID plot reveals smaller structures beneath each isotopic chain, which raises questions of isotopes of interest potentially mixing with beam contaminants during the experimental run. Efforts were undertaken to address this concern, improve the PID plot and enhance the reliability of radioactive ion identification as described in the subsequent section.

3.2.1.2 Improving the particle identification spectrum

The observation of additional bands in a raw PID is usually traced back to the opening of the I2 slits due to the large momentum acceptance used in β-decay experiments, resulting in the broadening of the TOF distribution. This is due to the ions taking different trajectories in the A1900 fragment separator, which will require characterizing the dependence of the TOF and ΔE

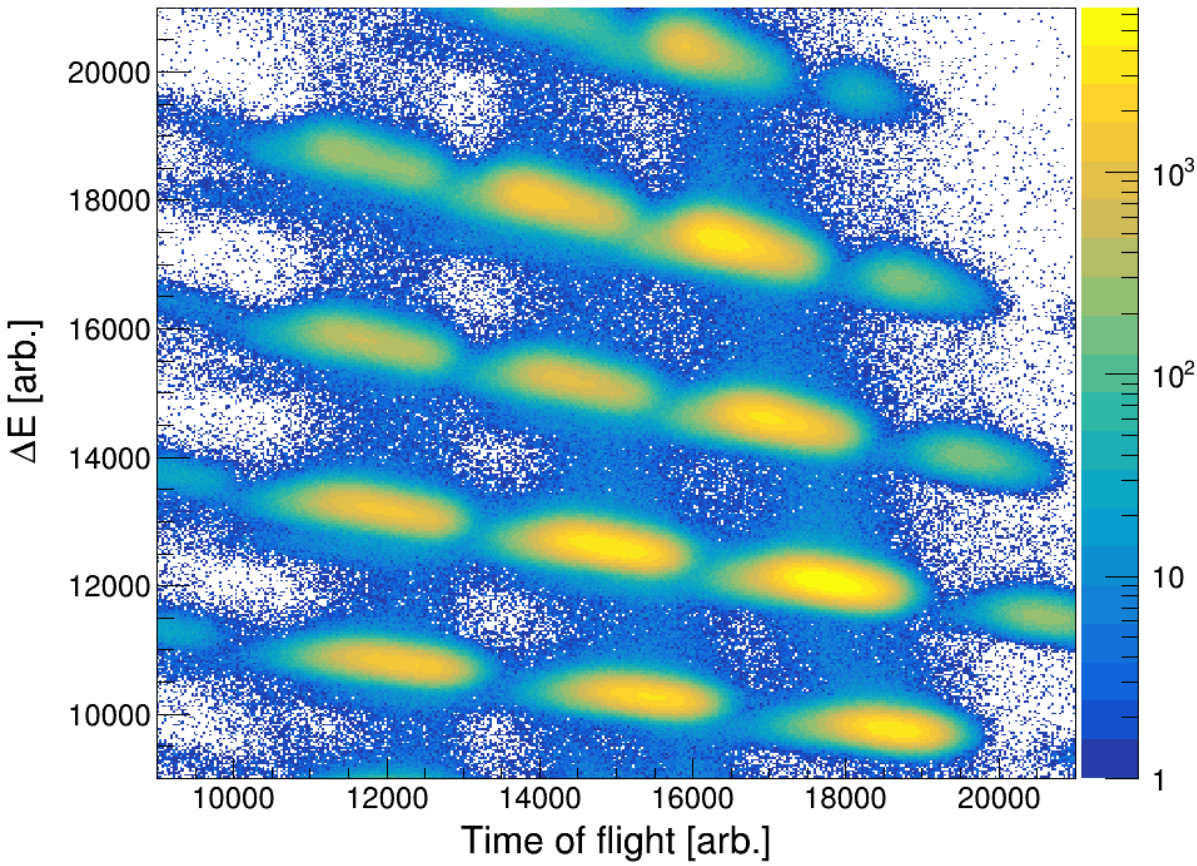

Figure 3.4: Raw particle identification (PID) plot for ions delivered to the experimental end station during experiment E16032. The plot displays the energy loss (ΔE) in the first PIN detector on the vertical axis, while the horizontal axis represents the time-of-flight (TOF) between the I2 scintillator in the A1900 and the first PIN detector. Each row of oval spots corresponds to a specific isotopic chain. Under each isotopic chain, smaller distributions can be observed.

of the ions based on their position in the I2 scintillator. The I2 position is obtained by calculating the time differences between the signals generated from photomultipliers connected to the north and south ends of the I2 scintillator.

Figure 3.5(a) shows a 2D plot depicting the correlation between the time-of-flight (TOF) and the position of the ions within the I2 scintillator. Discussions of a similar investigation in Ref. [29] showed multiple distributions in a similar 2D plot. In Figure 3.5(a), only one prominent distribution is evident, and there is no significant smearing or separation along isotopic bands. Consequently, it was determined that making a correction to the TOF would have little impact on improving the PID plot for E16032.

The dependence of ΔE on the I2 position is shown in Figure 3.5 (b). Three distinct distributions numbered "1", "2" and "3" were observed in the spectrum of ΔE plotted against the position of the ions in the I2 scintillator. A closer look at distribution "1" shows a smearing of the distribution about a constant I2 position for individual isotopic chains - informing the tightness of the graphical cut in red subsequently created to represent the distribution. A similar structure of smearing can be observed for the low-mass isotopes in distribution "2", while distribution "3" seems to be produced due to the re-triggering of the I2 scintillator.

Graphical cuts were created around the three distributions in Figure 3.5(b) such that PID spectra gated on each cut were plotted and compared to the raw PID. Figure 3.6 shows a comparison between the raw PID spectrum without any gates compared to the spectrum gated on distribution "1". In the gated spectrum, a more distinct separation is noticeable along isotopic chains. Moreover, the smaller structures observed beneath the isotopic chains in the raw PID spectrum are not evident when applying a tight gate specifically around distribution "1".

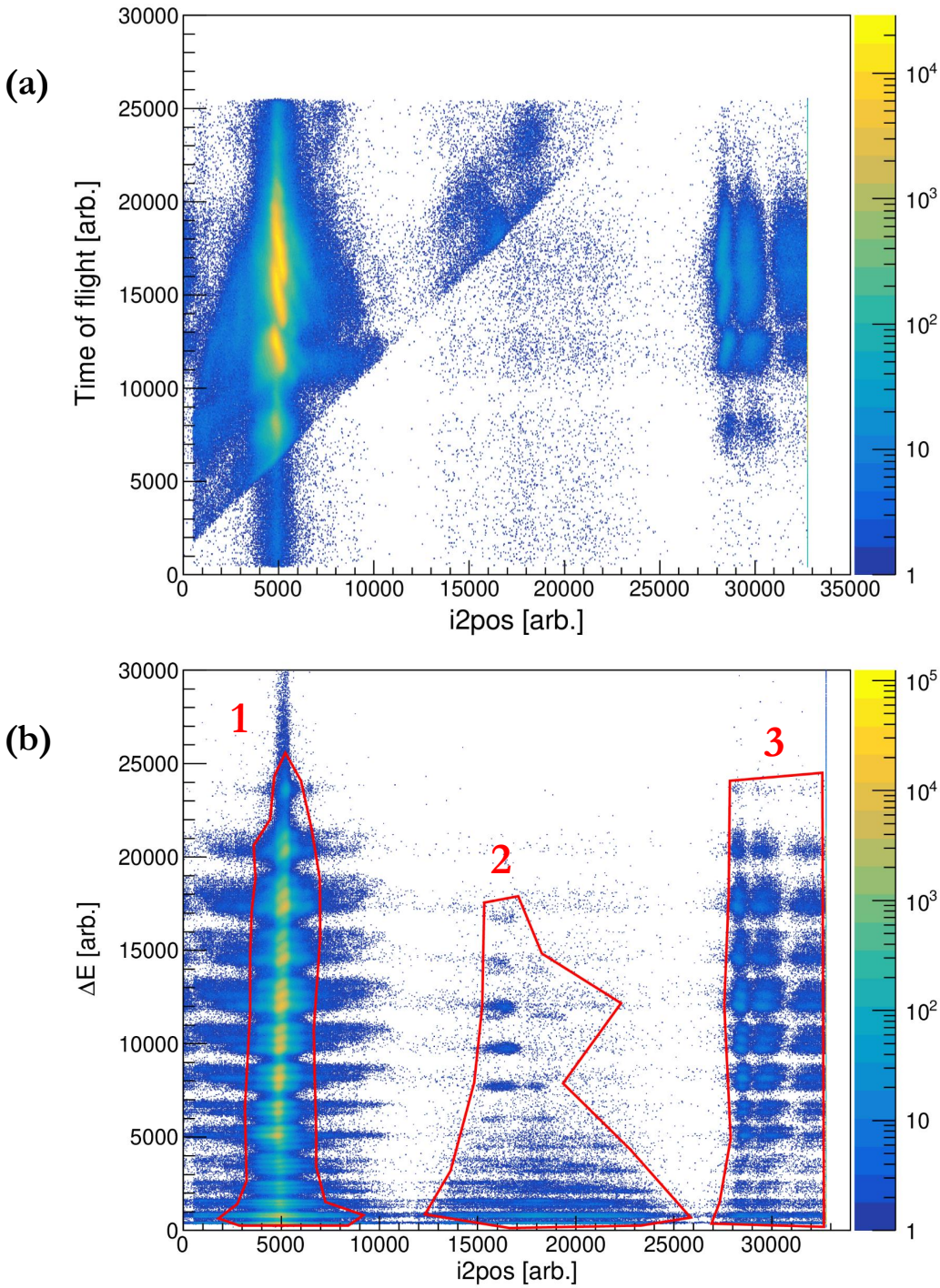

Figure 3.5: Plots of **(a)** the time-of-flight (TOF) between the first PIN detector and the I2 scintillator in the A1900, and **(b)** the energy loss in the first PIN detector, as a function of the I2 position for experiment E16032. In plot (b), three distinct distributions labeled as "1" (main distribution), "2" (low mass isotopes), and "3" (retriggering of the I2 scintillator) are visually captured by two-dimensional graphical cuts in red.

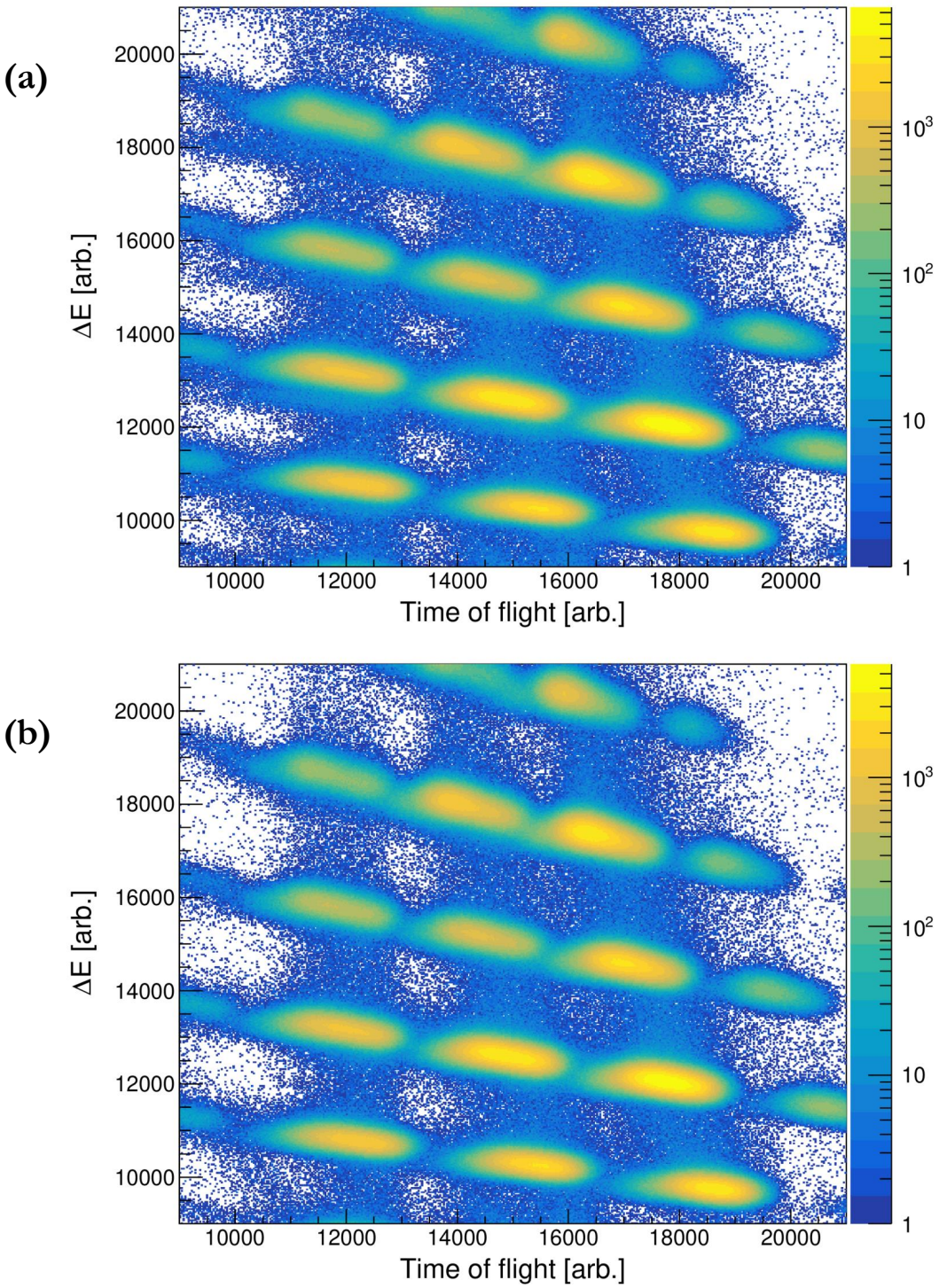

Figure 3.6: **(a)** Raw PID spectrum. **(b)** Corrected PID spectrum gated on distribution "1" in Figure 3.5(b). The entries in (b) appear devoid of the shadow structures that appear beneath each isotopic chain in the raw PID.

Table 3.2: Total number of ions delivered to the experimental end station in experiment E16032.

Isotope	Number of ions		Clean/Raw entries (%)
	Raw PID	Clean PID	
^{40}Si	477536	407374	85
^{39}Al	204135	171261	84
^{38}Al	982363	842491	86
^{37}Al	2020615	1741959	86
^{36}Mg	315608	266040	84
^{35}Mg	514523	438819	85
^{34}Mg	1599406	1368737	86
^{33}**Na**	**818637**	**692387**	**85**
^{32}Na	2202920	1894646	86
^{31}Na	3061458	2623059	86
^{30}Ne	877764	742227	85
^{29}Ne	1274388	1094753	86
^{28}Ne	1517473	1293707	85
		Average	85

Another set of tight 2D graphical cuts were created around each isotope such that their borders were defined using the cleaner PID spectrum gated on distribution "1". The total number of ions was extracted for each isotopic blob in the raw PID by calculating the integral of the graphical cuts described in the previous sentence. These values are shown in Table 3.2 and compared to the total number of ions from the cleaner PID generated using the gate around distribution "1", accounting for approximately 85% of entries in the raw PID spectrum.

Similar figures created for distributions "2" and "3" are shown in Appendix A and the total number of ions for each isotope was calculated using the same method described above. The PID spectra gated on these distributions accounted for an average of $\ll 1\%$ and $\sim 1\%$ of the entries in the raw PID spectrum, respectively. The contributions of the remaining $\sim 14\%$ of the data that fall

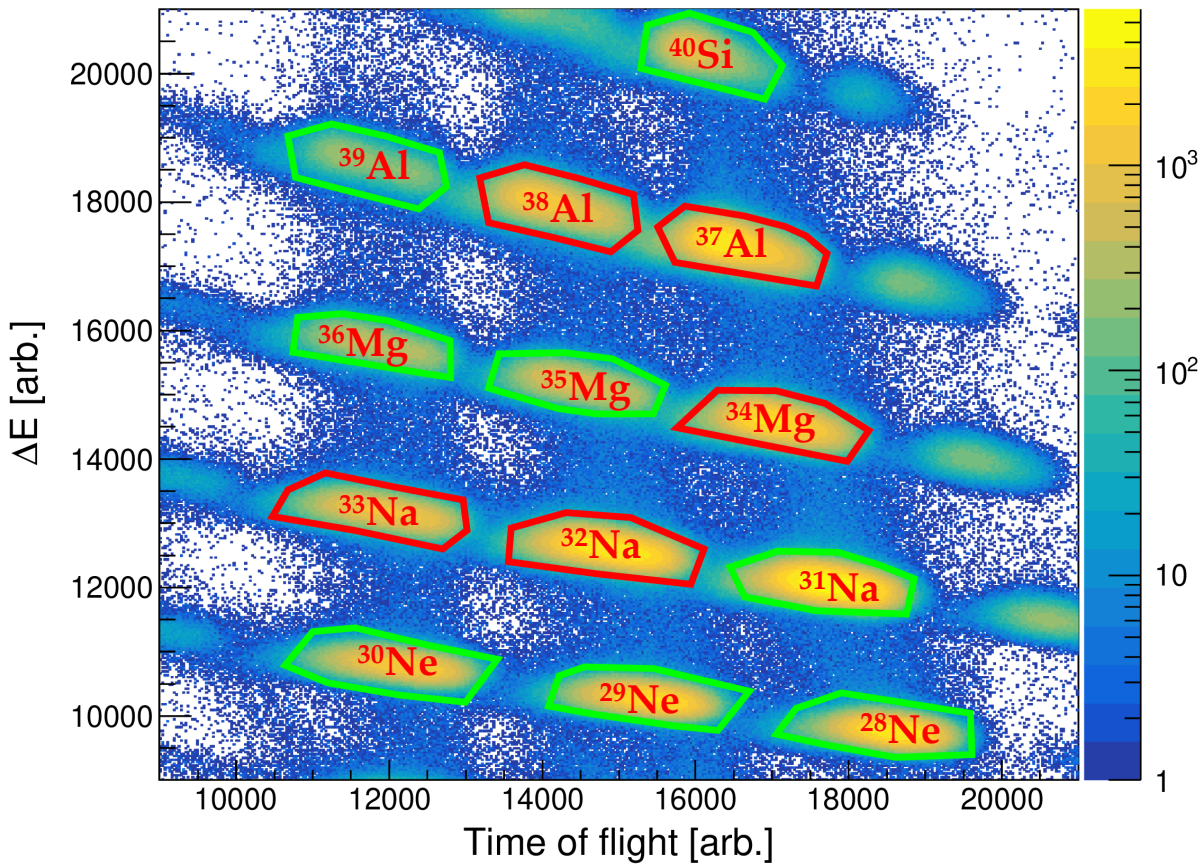

Figure 3.7: Corrected E16032 PID spectrum. The isotopes discussed in this dissertation are highlighted with red graphical cuts while others are shown in green.

outside of the primary three distributions bordered by the red graphical cuts in Figure 3.5(b), as well as distributions "2" and "3" were excluded from the analyses presented in this dissertation.

Although the main cause of the unclean PID spectrum in experiment E16032 is not fully known, efforts made to clean out the spectrum resulted in clearer particle identification for subsequent data analysis. The final PID used in analysis discussed in this dissertation is shown in Figure 3.7. It showcases various radioactive isotopes, including ^{32}Na, ^{33}Na, ^{34}Mg, ^{37}Al, and ^{38}Al, which populate the states characterized and emphasized in this dissertation. The ions were also verified using known γ rays in daughter isotopes as discussed in Chapter IV.

3.2.2 Cerium bromide ($CeBr_3$) implantation detector

Upstream of the implantation detector, a stack of aluminum degraders was positioned after the last Si PIN detector. These degraders, with an effective thickness of 8.3 mm, served to facilitate additional energy loss of the secondary beam, enough to optimize for 100% implantation of the beam centered around ^{33}Na, within the active volume of a thin 51 mm $\times$ 51 mm $\times$ 3 mm $CeBr_3$ implantation detector, as illustrated in Figure 3.3. The $CeBr_3$ implantation detector was located at the center of the experimental end station, with a 0.5 mm-thick aluminum entrance window.

The range distribution of ions stopped within the volume of the $CeBr_3$ detector is presented in Figure 3.8, calculated using the LISE++ Monte Carlo simulation toolkit [69] for fragment transmission and ion optics calculation and optimization. The range distribution was obtained by integrating the energy loss, ΔE along the path of each ion. It is important to mention that the LISE++ simulation takes into account the interaction of the secondary beam with all detector and degrader materials before implantation within the $CeBr_3$ detector.

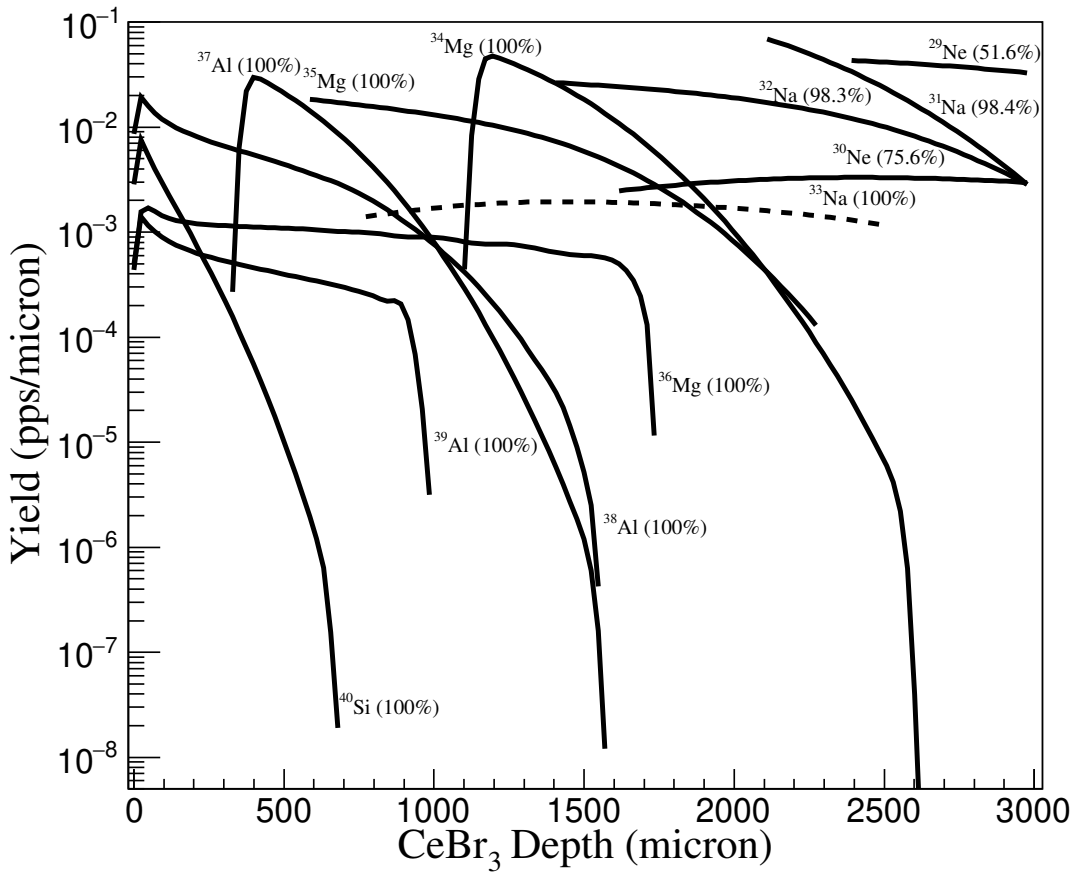

Figure 3.8: Depth distribution profile of ions implanted within the 3mm-thick $CeBr_3$ crystal calculated using LISE++ and optimized for 100% implantation of ^{33}Na (dashed line). The numbers in bracket represent the percentage of implanted ions that are incident on the $CeBr_3$ crystal. (See text for additional information.)

As shown in Figure 3.2(d), the $CeBr_3$ detector was optically coupled to a 52 mm $\times$ 52 mm Hamamatsu H13700 series Position Sensitive Photo-Multiplier Tube (PSPMT) [79]. The PSPMT was electronically segmented over a 16 $\times$ 16 grid allowing for pixelation of the signals read out after charged particles are registered within the $CeBr_3$ crystal. Energy information from each 3 mm $\times$ 3 mm pixel was read out by individual anodes, amounting for 256 of the 320 digitizer channels used for instrumenting the experimental setup. The development of the readout cables was carried out in collaboration with CD International Technology.

A single PSPMT dynode readout was also used in the instrumentation of the $CeBr_3$, representing the summed energy output of all anode readouts. In addition to providing energy information, the output from the PSPMT dynode served as a fast timing reference for all recorded events. To ensure optimal timing performance of the setup, the PSPMT was instrumented using 1 of 16 digitizer channels on a 500 MHz XIA Pixie-16 digitizer module [78]. This same digitizer module was also employed for instrumenting the 15 fast timing $LaBr_3$ detectors employed in the experimental setup. In contrast to the dynode, the PSPMT anodes were instrumented with 250 MHz digitizers, as their primary function was for position determination rather than timing information.

Successful analysis of data including efficient correlation of β-decay and $E0$ electrons to the relevant ions, as well as the attribution of β-delayed γ rays to the decay of radioactive parents hinges on the valid identification and discrimination of these radiation types registered within the $CeBr_3$ crystal. Event-type identification and classification techniques relevant to the analysis of E16032 data are discussed in the following subsections.

3.2.2.1 Pulse shape analysis

Following the implantation of radioactive ions, radiation including electrons emitted during β decay, $E0$ decay or pair production, as well as γ rays are detected by the $CeBr_3$. These radiation signals exhibit characteristic timing delays.

Event identification and discrimination was achieved by analyzing the PSPMT dynode traces, where the number of pulses recorded in a trace served as an experimental identifier for the event type. In this analysis, the presence of a single pulse indicated the recording of a β-decay event (referred to as a single-pulse event) following ion implantation. On the other hand, the presence of two pulses, separated in time, indicated the detection of another transition that occurred after β decay within the $CeBr_3$ crystal (referred to as a double-pulse event). In rare instances, an additional pulse may be observed in a trace. However, the discussions in this subsection are focused solely on events with two pulses.

The energy and time difference between the two pulses in a double-pulse trace are the primary characteristics that define such events and enhance the selectivity of identifying isomeric transitions using the $CeBr_3$ implantation detector. Trace fitting algorithms were optimized to properly characterize such events and discriminate the single-pulse from double-pulse events. It is also worth noting that not all events with multiple pulses are distinctly separated in time, as they may fall below the timing resolution of the $CeBr_3$ detector.

Two distinct fit functions comprising of the rise time of a logistic function convoluted with an exponential decay were employed to characterize the response of the $CeBr_3$ detector, represented by the PSPMT dynode trace. This approach, based on prior work in Ref. [68], was validated for the $CeBr_3$ detector in Refs. [10, 11]. A single-pulse fit function expressed as

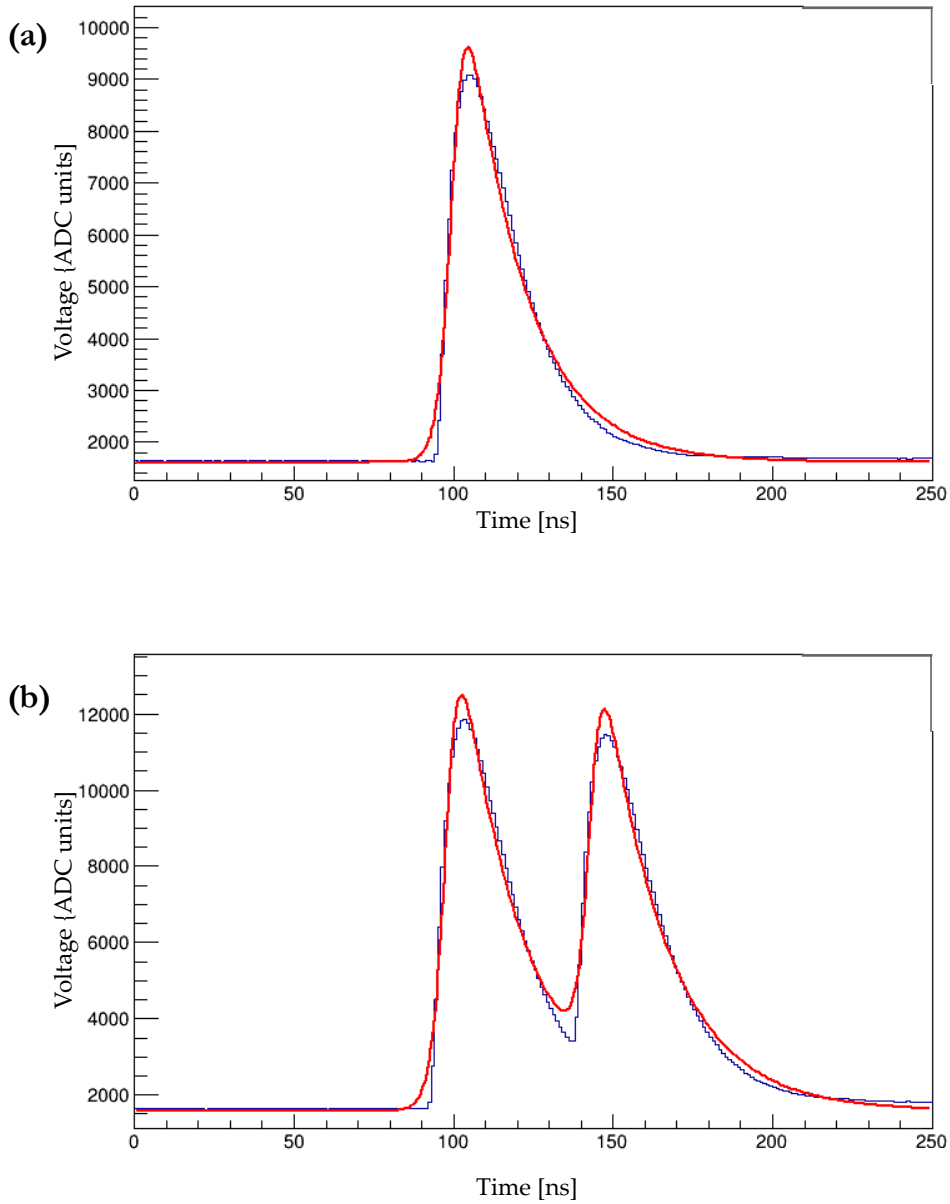

Figure 3.9: **(a)** An example of a single-pulse trace indicating the detection of a β-decay electron. **(b)** An example of a double-pulse trace indicating the detection of an $E0$ electron, γ ray or pair production electron following β decay. The detector response was modeled using the fits (in red) superimposed on the traces.

$$F(t) = \frac{A_1 \exp^{-k_1(t-t_1)}}{1 + \exp^{-k_2(t-t_1)}} + C, \tag{3.2}$$

was used to model a typical β-decay event while the observation of another radiation type following β decay was modeled using a double-pulse fit function expressed as

$$F(t) = \frac{A_1 \exp^{-k_1(t-t_1)}}{1 + \exp^{-k_2(t-t_1)}} + \frac{A_2 \exp^{-k_3(t-t_2)}}{1 + \exp^{-k_4(t-t_2)}} + C. \tag{3.3}$$

In Eqs. 3.2 and 3.3, A_1 and A_2 represent the pulse heights or amplitudes, k_1 and k_3 are the exponential decay constants, k_2 and k_4 are the risetime constants, t_1 and t_2 are the event time parameters and C is a constant background term.

Each PSPMT dynode trace recorded by DDAS was fit with both single- and double-pulse fit functions as shown in Figure 3.9(a) and (b), and their qualities were gauged using χ^2 values extracted by comparing the experimental traces and the fits. The adequacy of both fit functions in modeling the detector response was evaluated by comparing the ratio of the χ^2 value obtained from the single-pulse fit to the χ^2 value obtained from the double-pulse fit, as shown in the distribution presented in Figure 3.10. This ratio served as a metric to determine whether the fit functions adequately described the data.

As shown in Figure 3.10, a $\chi^2_{single}/\chi^2_{double}$ ratio of 10 was chosen to separate "good" single-pulse fits from "good" double-pulse fits such that

$$\frac{\chi^2_{single}}{\chi^2_{double}} < 10 \text{ for "good" single-pulse fits, and} \tag{3.4}$$

$$\frac{\chi^2_{single}}{\chi^2_{double}} > 10 \text{ for "good" double-pulse fits.} \tag{3.5}$$

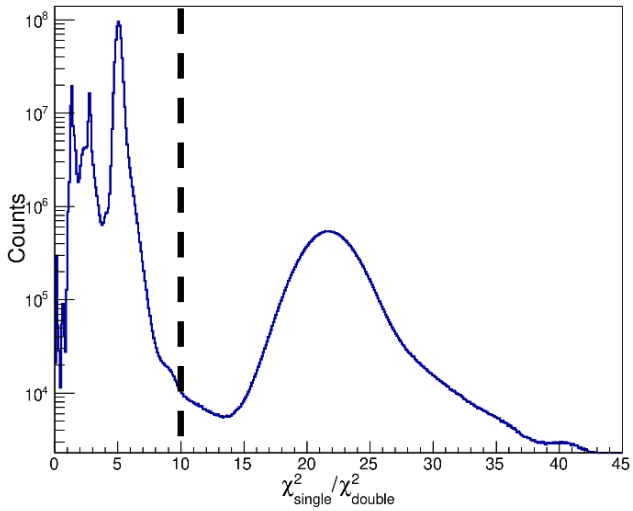

Figure 3.10: Distribution of $\chi^2_{single}/\chi^2_{double}$ ratios based on fitting of the PSPMT dynode traces. The dashed line represents the $\chi^2_{single}/\chi^2_{double}$ ratio of 10 chosen to separate "good" single-pulse fits from "good" double-pulse fits.

Parameters associated with the "good" fits, including amplitudes and timestamps were recorded and subsequently used for further analysis. For example, I discuss techniques associated with correlating β-decay electrons to implanted radioactive ions in the following subsection. This is relevant for events involving the detection of electrons due to β decay only — single-pulse events. I therefore use the "good" single-pulse fit condition to identify relevant PSPMT dynode traces to access pulse information recorded as fit parameters. Further discrimination required for analyzing data associated with double-pulse events are discussed in Chapter V.

3.2.2.2 Decay-Ion Correlation

Radioactive ions delivered to the experimental end station as a cocktail beam lose some energy in the Si PIN detectors as well as Al degraders before getting implanted within the $CeBr_3$ detector.

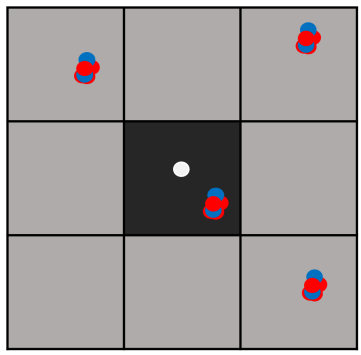

Figure 3.11: Illustration of a 3 × 3 correlation grid. Assuming, in the simplest of terms, a decay electron (represented by a white circle) is detected in the darkest grid, the search for implanted ions (red and blue circles) for correlation is limited to the 3 × 3 correlation grid while ions with interaction positions outside of the grid are not considered. *It is worth noting that a 1 × 1 correlation grid is preferred for substantial background reduction. This is however not considered in the scope of this dissertation to maximize statistics.*

Following ion implantation, β decay occurs after a characteristic amount of time, such that β-decay electrons interact with the $CeBr_3$ and deposit their energy within its volume until they are fully stopped. The β-decay electrons must then be correlated to respective implanted ions using spatial and temporal information recorded by the PSPMT anodes and dynode, respectively.

In order to establish correlation between decay electrons and implanted ions in this dataset, certain conditions were applied. First, an implanted ion had to be detected within the same pixel as a decay electron, or within a 3 × 3 correlation grid as shown in Figure 3.11. This ensured that the ion and electron were in close proximity and likely originated from the same event. Once the first condition was satisfied, the timing information obtained from the implanted ions was utilized for further analysis. The goal was to identify the ion that was implanted closest in time to the decay electron, thus establishing a correlation between the two.

To achieve efficient correlation results, it was essential to accurately determine the interaction positions of all events, and therefore necessary to keep the ion implantation rate low during the experiment. This ensured that each decay electron could be uniquely associated with an implanted ion, minimizing ambiguities and false correlations. I explain concepts pertinent to position extraction and event identification below.

Spatial information: Determining interaction positions

The pixelization of the anode readouts was instrumental towards accurately localizing interactions registered within the $CeBr_3$ detector on an event-by-event basis. Figure 3.12 and Figure 3.13 show the 2D energy distribution profiles of sample ion implantation and decay events readout by the PSPMT anodes, respectively. Interaction positions were determined by fitting the energy distribution profile with a 2D Lorentzian function defined as

$$L(x, y) = A \times \left(\frac{\Gamma_x^2 \Gamma_y^2}{[(x - x_0)^2 + \Gamma_x^2][(y - y_0)^2 + \Gamma_y^2]} \right) \tag{3.6}$$

where A is the amplitude, Γ_x and Γ_y are the widths, and x_0 and y_0 are the positions along the x- and y-axes, respectively. An alternative to extracting interaction positions using the 2D Lorentzian fit, developed to combat the slow, iterative procedure was carried out by A. Chester and briefly discussed in Appendix B.

Event identification

Several event-type identifiers were created to distinguish between interactions registered in the $CeBr_3$ implantation detector for efficient correlation purposes during single-pulse events described in Section 3.2.2.1. The observation of signals in the silicon PIN detectors and $CeBr_3$ implantation detector were primarily used as discriminators for event identification. Furthermore, every event

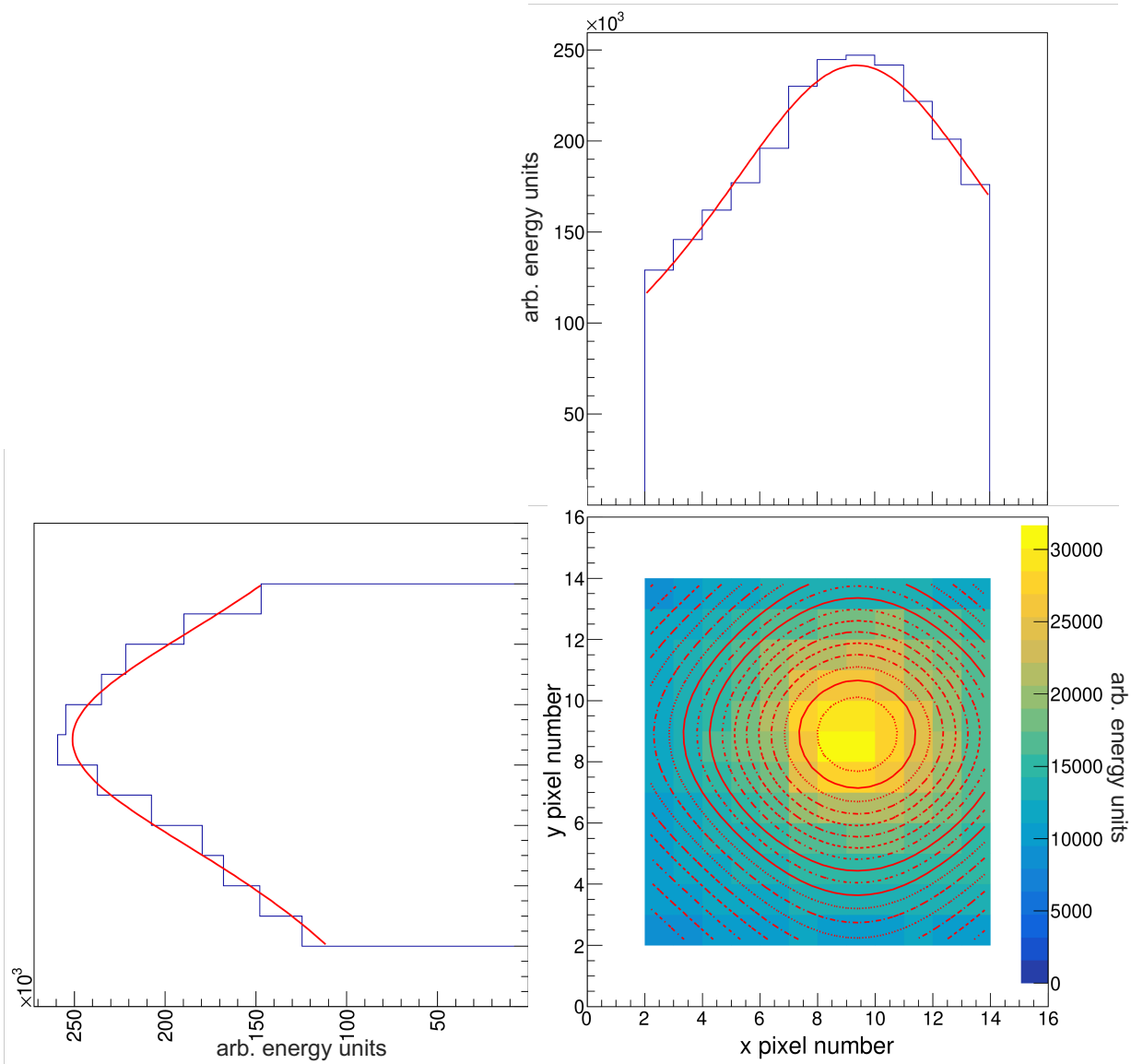

Figure 3.12: **Bottom right**: Energy distribution of the PSPMT anodes for an ion implantation event observed across the 16 × 16 grid. The x,y position information for this event was determined by fitting a 2D Lorentzian function (red overlay) to the energy distribution. **Bottom left**: Projection of the 2D energy distribution map onto the y axis, with the y-component of the 2D Lorentzian fit overlaid. **Top right**: Projection of the 2D energy distribution map onto the x axis, with the x-component of the 2D Lorentzian fit superimposed. Each pixel contains recorded anode energies. (See text for more details.)

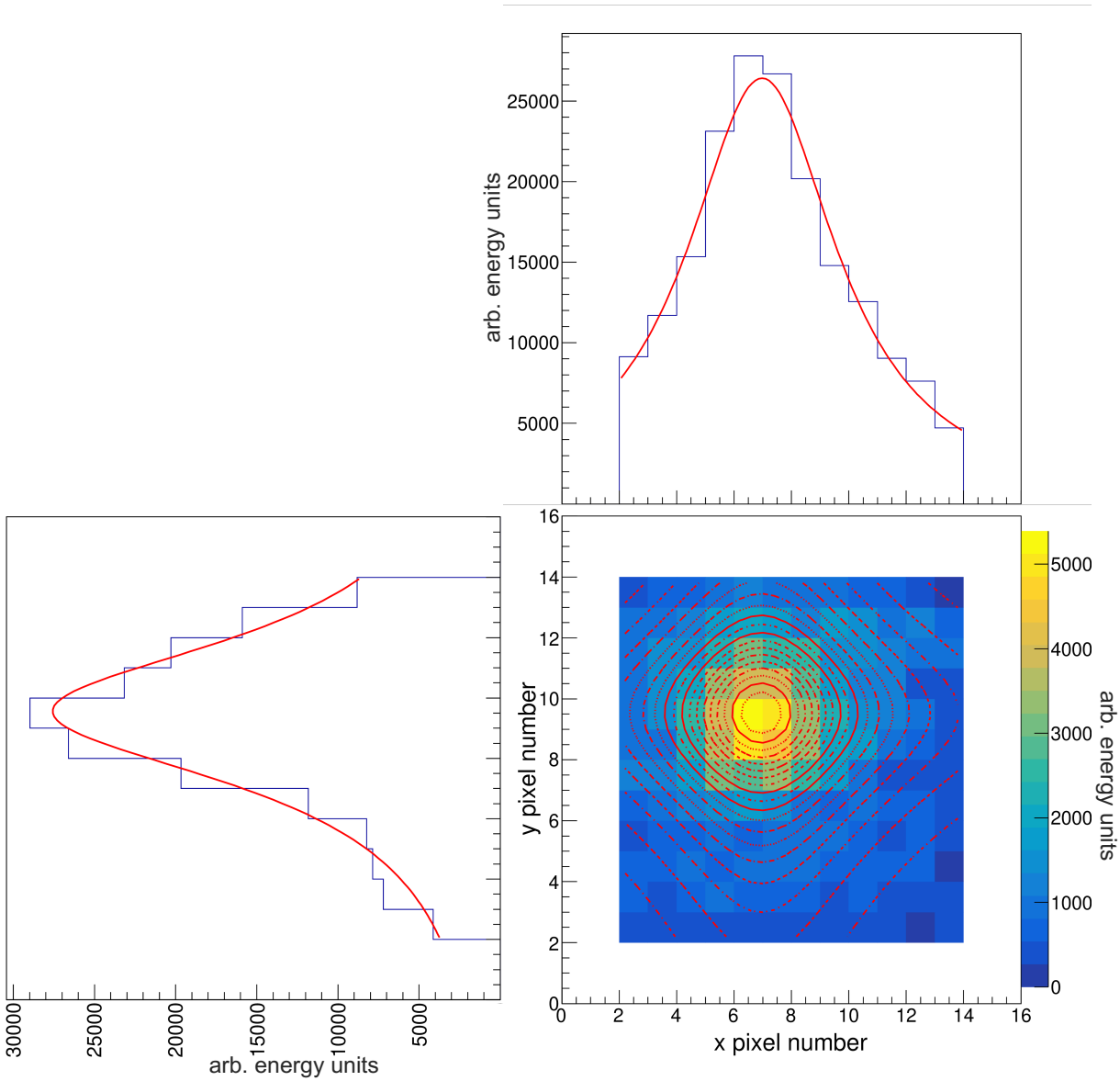

Figure 3.13: **Bottom right**: Energy distribution of the PSPMT anodes for a decay event observed across the 16 × 16 grid. The x,y position information for this event was determined by fitting a 2D Lorentzian function (red overlay) to the energy distribution. **Bottom left**: Projection of the 2D energy distribution map onto the y axis, with the y-component of the 2D Lorentzian fit overlaid. **Top right**: Projection of the 2D energy distribution map onto the x axis, with the x-component of the 2D Lorentzian fit superimposed. Each pixel contains recorded anode energies (See text for more details.)

Table 3.3: Event-type discrimination for decay-ion purposes in E16032.

Event type	Detector(s) required	Additional conditions
Implants	PIN 1 only	PIN 01 energy > 5000 arb. units; x,y position within 16 ×16 PSPMT grid
Decays	$CeBr_3$ (PSPMT) only	Dynode energy < 6200 arb units; x,y position within 16 ×16 PSPMT grid
Light ions	$CeBr_3$ (PSPMT) only	PIN 01 energy < 5000 arb. units; Dynode energy < 6200 arb. units; x,y position within 16 ×16 PSPMT grid

type considered for correlation was required to have corresponding interaction positions within the experimentally feasible 16 × 16 PSPMT grid [2]. This was done to weed out the few instances when the fitting procedure used to localize interaction positions failed — a feature common to interactions near the edge of the PSPMT. I describe the main event types taken into consideration for correlation purposes below, and summarized in Table 3.3.

I **Implants:** An ion implantation event differs from the decay events described in the next point as it involves the secondary beam interacting with both the Si PIN detectors and the $CeBr_3$ implantation detector. For this reason, a condition requiring signals to be observed in both the Si PIN detectors and the PSPMT dynode during single-pulse events was implemented to flag implant events. This is emphasized by comparing Figure 3.14(a) and (b). In Figure 3.14(a), the PSPMT dynode energy distribution for all single-pulse events, which includes implant and decay events, is displayed. When the condition to flag implant events is applied before populating the spectrum, the distribution shown in Figure 3.14(b) reveals a

[2] In the case of E16032, the outermost two-pixel frame on the PSPMT grid, represented by the anode readout cables, was excluded from the PIXIE-16 digitizers due to the high data rate exceeding the readout capabilities. Consequently, an experimentally feasible 14 × 14 grid was taken into account.

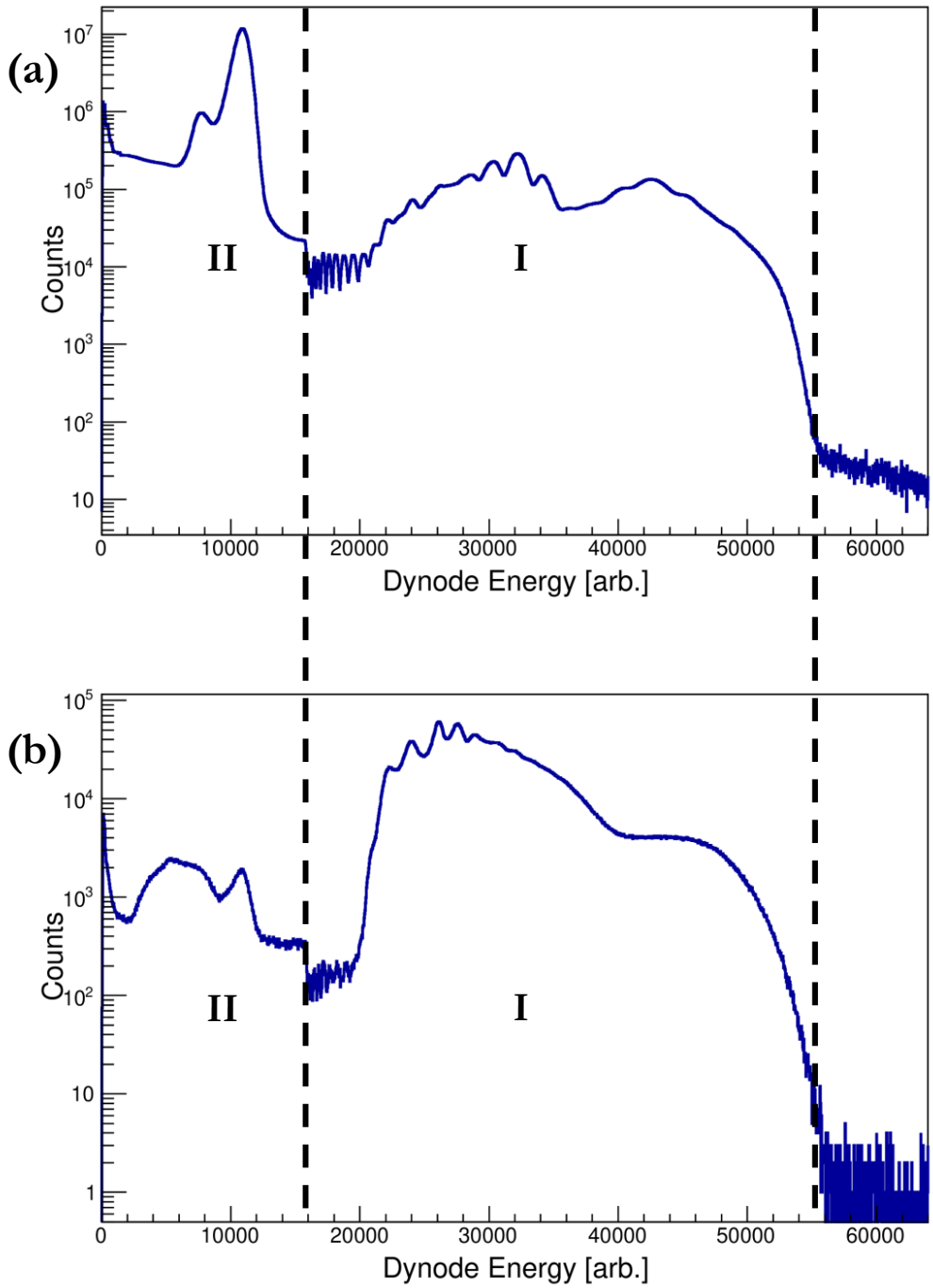

Figure 3.14: **(a)**: PSPMT dynode energy distribution for single-pulse events. **(b)**: Conditional PSPMT dynode energy spectrum for single-pulse events identified as **implants** (region I) informing the demarcation of energy regions with dashed lines. (See text for additional information.)

Table 3.4: Percentage of ions implanted in the $CeBr_3$ detector.

Isotope	Number of ions		Transmission (%)
	Detected in PIN 1	Implanted in the $CeBr_3$	
^{40}Si	407374	207612	51
^{39}Al	171261	35693	21
^{38}Al	842491	765427	91
^{37}Al	1741959	1626917	93
^{36}Mg	266040	243401	91
^{35}Mg	438819	409922	93
^{34}Mg	1368737	1297789	95
^{33}Na	692387	648075	94
^{32}Na	1894646	1794761	95
^{31}Na	2623059	2501548	95
^{30}Ne	742227	700780	94
^{29}Ne	1094753	1040574	95
^{28}Ne	1293707	1235495	96

noticeable enhancement of region I relative to region II. This enhancement clearly indicates that dynode energies recorded within region I correspond to ion implantation.

Implant events considered for correlation also had corresponding x,y positions that fell within the 16 $\times$ 16 PSPMT grid. These events were flagged as "good" implant events. Table 3.4 shows the percentage of ions of interest implanted within the $CeBr_3$ detector. These percentages were calculated by comparing the counts of each isotope in the PID spectrum shown in Figure 3.7 to the counts in the PID spectrum created using the conditions for flagging "good" implant events.

II **Decays:** Following ion implantation, β decay occurs after a characteristic amount of time such that β-decay electrons are detected within the $CeBr_3$ crystal. "Good" decay events were flagged when signals were **only** recorded by the PSPMT; and the event position fell within the

16×16 PSPMT grid. Decays are easily distinguishable from implants based on the amount of energy the decay electrons deposit within the $CeBr_3$ compared to implants in the higher-energy range. It is shown in Figure 3.14(b) that decays fall will within region II of the PSPMT dynode energy distribution. However, complications arise due to the presence of light ions that fall within a similar energy range as decays. Therefore, additional considerations were required to further discriminate decays from light ions as described below.

III **Light ions:** Light ions were delivered to the experimental end station alongside heavy ions that decay and populate states in daughter nuclei. In reality, light ions lose energy as they pass through the PIN detectors for E16032, but their ΔE values were lower than the PIN detection thresholds, such that no corresponding PIN signals were recorded. Although light ions are not stopped within the $CeBr_3$ crystal, they still interact with the detector volume and have corresponding PSPMT signals recorded, leading to the possibilities of flagging them as "good" decay events. Complications arise because they fall under a similar energy range as decays. Light ions must therefore be properly flagged for accurate discrimination from decay events. In E16032, light ions were distinguished from decays by applying an energy cut to ΔE values obtained from the PIN detector and used for particle identification. It is worth noting that an alternative method for tagging light ions could involve employing a thick veto detector instrumented with a high-gain preamplifier in the experimental setup.

Figure 3.15(b) shows the PSPMT dynode energy distribution filled with the condition for flagging light ions (energy cut on ΔE with PSPMT signals). Region II was subdivided into II A and II B, primarily due to the heightened presence of region II B in comparison to II A when the condition for detecting light ions was employed. Although it is expected that

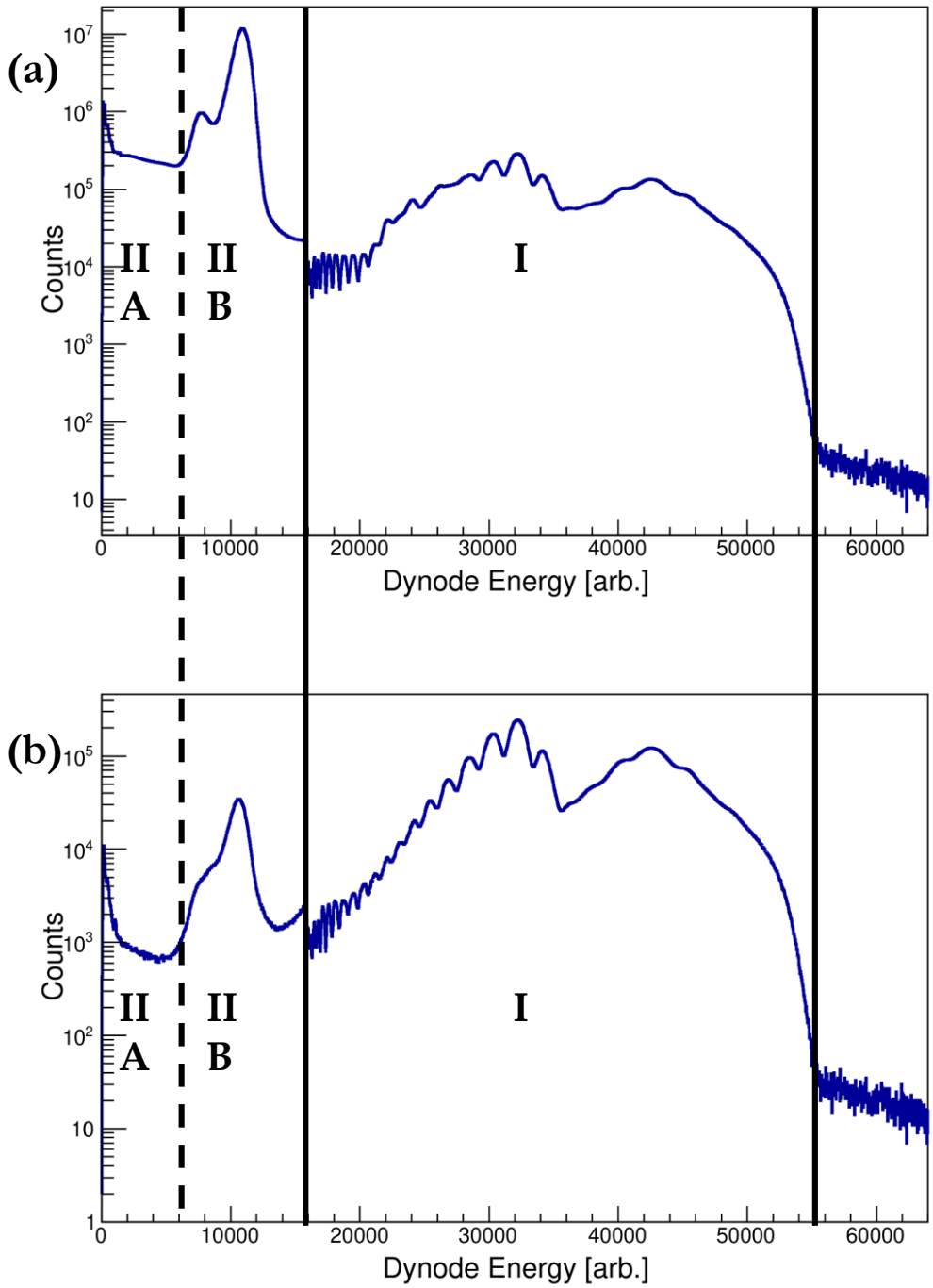

Figure 3.15: **(a)**: PSPMT dynode energy distribution for single-pulse events. **(b)**: Conditional PSPMT dynode energy spectrum for single-pulse events identified as **light ions**, informing the division of energy region II into two distinct regions demarcated by the dashed line.

certain decays may fall within region II B, a distinct boundary for region II A was set to ensure reliable ion - decay correlations , even though statistics were substantially reduced.

Temporal information: Correlation time windows

After accurately determining the interaction positions and identifying ions within a correlation grid, a decay electron can be correlated with the ion that was detected closest in time to it. However, the presence of *"back-to-back"* ion implantation events, where multiple ions are implanted in the same pixel in a correlation grid within a short time window, complicates this procedure. To address this, it is crucial to conduct the experiment with a low per-pixel implantation rate and establish reasonable decay-ion correlation windows to accurately attribute the decay electron to the corresponding ion.

The correlation window is representative of the half-life of the nucleus undergoing β-decay and must be set so that the probability of correlating a decay electron to an earlier ion implantation event is low (with the convention being a probability of less than 12.5%.) For the current analysis, the correlation window was carefully defined to ensure that the time difference between ion implantation events was at least 3 times longer than the β-decay half-life of the nucleus of interest. This choice of correlation window provides a sufficient temporal separation between the implantation events.

It is important to note that alternative, shorter correlation time windows could potentially be used in different scenarios or analyses. However, for the specific purpose analysis discussed in this dissertation, the chosen correlation window configuration was deemed appropriate for a balance between number of random correlations, good peak to background ratios and amount of statistics in β-delayed γ-ray spectra discussed in Section 4.1.1 of Chapter IV.

3.2.3 β-delayed γ-ray detectors

Ground states as well as excited states in daughter nuclei are populated following β decay of implanted parent nuclei. A nucleus in an excited state will often de-excite by emitting energy in the form of high-energy light or photons - in this case referred to as β-delayed γ rays. These γ rays were detected using two ancillary arrays surrounding the $CeBr_3$ implantation detector [62]. The first array — a Segmented Germanium Array (SeGA) — consisted of 16 segmented high-purity germanium (Ge) detectors and the second comprised of 15 $LaBr_3$(Ce) detectors. I provide additional information on the detector sets relevant to analysis presented in this dissertation below.

3.2.3.1 Segmented Germanium Array (SeGA)

The Segmented Germanium Array (SeGA) consists of multiple 32-fold segmented high-purity germanium (HPGe) detectors [43] that can be arranged in different configurations depending on the kind of experiment carried out. SeGA, although typically reserved for in-beam γ-ray spectroscopy of intermediate energies, was used in this experiment with the HPGe detectors arranged in the "beta-SeGA" configuration [45] in two concentric rings of around the $CeBr_3$ implantation detector as shown in Figure 3.2(a). Specifically, 8 of the detectors were placed upstream of the $CeBr_3$ detector and the other 8 detectors placed downstream, all equidistant to the center of the $CeBr_3$ implantation detector at a radial distance of 8.6 cm. Energy and detection efficiency calibration efforts relevant to the SeGA detectors are detailed in subsequent subsections.

SeGA efficiency calibrations

Accurate detection efficiency calibration is crucial in γ-ray spectroscopy, especially when it comes to measuring γ-ray intensities. In E16032, like most ion implantation studies, γ rays were emitted from within the volume of the $CeBr_3$ implantation detector, following decay of implanted

ions. Monte Carlo simulations were therefore required to model the emission of γ rays based on the distribution of sources — in this case the implanted ions — and accurately measure the detection efficiency of the ancillary HPGe detectors that make up SeGA, while accounting for all attenuating materials between the implanted ions and the active volume of the γ-ray detectors. GEANT4 radiation transport toolkit [5] was used for modeling the E16032 setup as described in subsequent subsections.

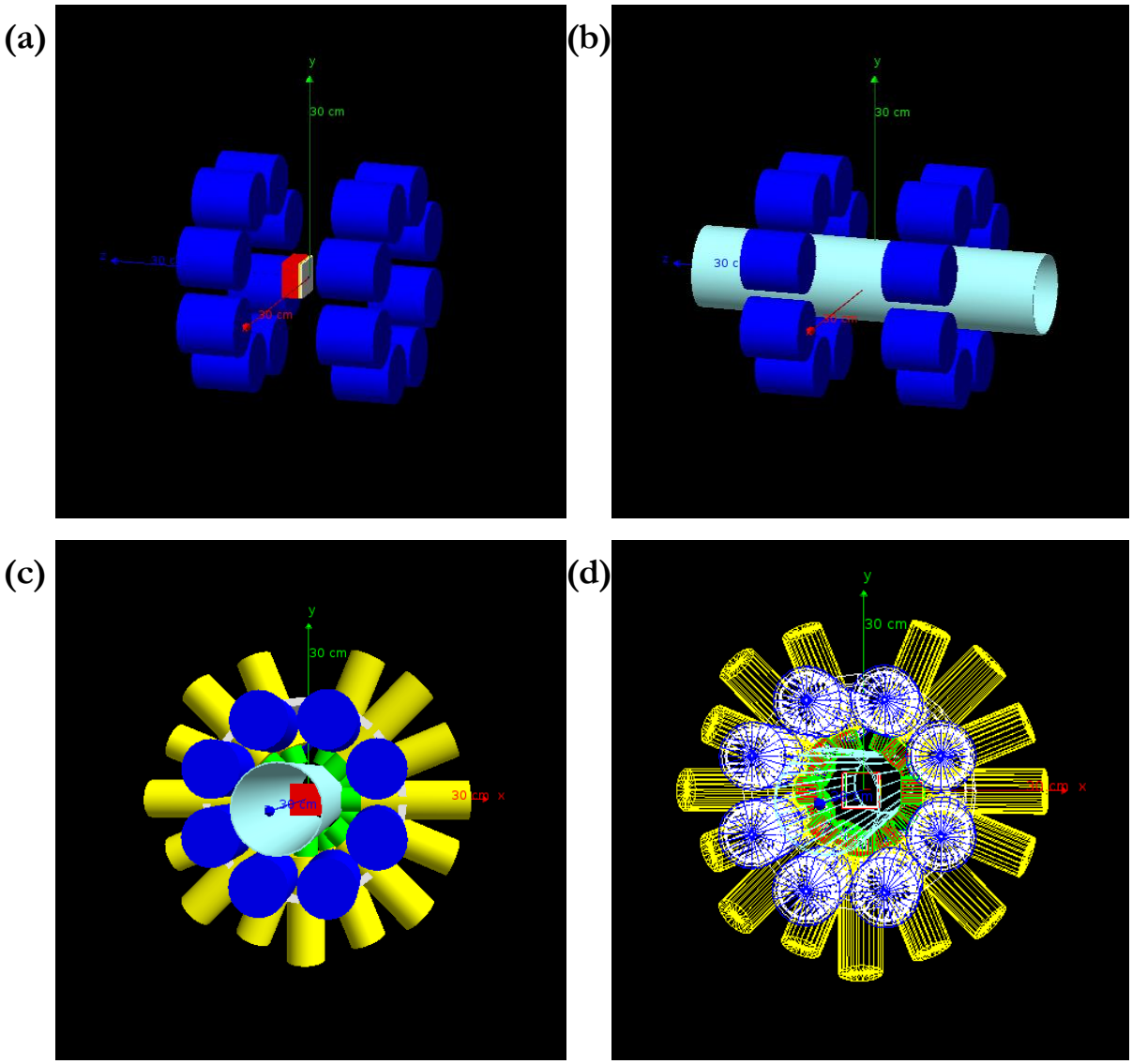

Legend (Surface view)	
	$CeBr_3$
	PSPMT
	SeGA Cryostat
	Pipe
	$LaBr_3$ Electronics Housing
	$LaBr_3$ Al Cover

Figure 3.16: E16032 experimental setup modeled in GEANT4. **(a)**: Orientation of SeGA relative to the $CeBr_3$ and PSPMT. **(b)**: Aluminum pipe housing the $CeBr_3$ and PSPMT included in the model. **Bottom**: Orthographic view of full setup in surface (**c**) and wireframe (**d**).

Benchmarking efficiency calibrations

The validity of the GEANT4 simulation was confirmed by benchmarking simulated SeGA γ-ray detection efficiencies against experimentally measured efficiencies of γ rays emitted by a National Institute of Standards and Technology (NIST)-calibrated mixed radionuclide source or standard reference material (SRM). The SRM, which was a point-source on a polyester tape containing ^{125}Sb, ^{154}Eu, and ^{155}Eu, was positioned at a precisely defined location on the surface of the $CeBr_3$ implantation detector. Data collection took place for approximately 23 hours.

The experimental setup was modeled in GEANT4 as shown in Figure 3.16. The SRM was replicated using point mono-energetic γ-ray sources that isotropically emitted one million γ rays with energies ranging from 42.8 keV to 1596.4 keV. It is worth noting that the γ rays considered for benchmarking purposes were primarily emitted from the ^{154}Eu and ^{155}Eu components of the SRM. This emphasis is due to the fact that the ^{125}Sb component of the SRM, with a half-life of 2.76 years, had decayed away by the time of the measurement[3]. Components of the experimental setup including detectors like the $CeBr_3$ coupled with the PSPMT; attenuating materials like the aluminum beam pipe; as well as layers of the HPGe detectors that made up SeGA were meticulously constructed in GEANT4 to ensure accuracy in the modeling process. Particular attention was geared towards modeling the germanium dead layer in the HPGe detectors known to increase in thickness over time [12]; and contribute to a reduction in the detection efficiency for γ-ray energies between 10 and 60 keV which lie close to the Ge K-absorption edge [16]. Additional considerations were also taken into account while extracting the experimentally measured detection efficiencies. These are outlined below.

Consideration: Coincidence summing

[3]The SRM source was produced on 9/1/1988 while the source measurement for E16032 took place on 7/5/2018.

β decay populates the ground state as well as several excited states in radioactive nuclei. The majority of these excited states have half-lives (on the order of ns to ps) and decay to lower-lying states involved in a γ-ray cascade. The poor timing resolution of HPGe detectors used in high-resolution γ-ray spectroscopy varies from the very short half-lives of these excited states and is a typical limitation of these detectors. This limitation becomes significant when two or more γ rays in coincidence are incident on the same detector, a process known as *coincidence summing*. Coincidence summing can have two effects on γ-ray spectra: it can either reduce the number of entries in photopeaks associated with γ rays in a cascade (referred to as "*summing out*"), or increase the number of entries in photopeaks corresponding to any γ ray with an energy equal to the combined energy of coincident γ rays in a cascade (referred to as "*summing in*") [77]. Therefore, when performing γ-ray efficiency measurements, particularly with sources that emit multiple γ rays in coincidence compared to simulated mono-energetic γ-ray sources, it is crucial to consider and correct for coincidence summing effects [27].

Summing corrections recommended by NIST in the accompanying source data sheet and subsequently applied to the detection efficiencies of the eleven γ rays used for efficiency calibration are shown in Table 3.5. The summing corrections were applied by dividing the efficiencies of the γ rays with energy E by the evaluated summing correction. In the table, $\{E\}$ represents the full-energy peak (photopeak) efficiency at γ-ray energy, E or the fraction of all emitted γ rays recorded in a full-energy peak. $[E]$ is the total efficiency at γ-ray energy, E or the fraction of radiation emitted at a given energy that generates pulses of any size.

Table 3.5: Summing corrections applied to detection efficiencies of γ rays emitted by the SRM, recommended by NIST. (See text for details.)

E (keV)	Summing correction
42.8	1.0
105.3	1.0
123.1	1.0 − 0.072[248.0] − 0.055[591.7] − 0.019[692.4] − 0.120[723.3] − 0.049[756.9] −0.130[873.2] − 0.201[1004.8] − 0.010[1246.2] − 0.401[1274.4] − 0.021[1596.5]
248.0	1.0 − 0.287[42.8] − 0.455[123.1] − 0.072[444.4] − 0.022[582.0] − 0.134[591.7] −0.015[612.2] − 0.043[625.2] − 0.022[676.6] − 0.039[723.3] − 0.613[756.9] −0.059[892.7] − 0.022[904.1] − 0.130[1246.2]
591.7	1.0 − 0.297[42.8] − 0.455[123.1] − 0.178[248.0] − 0.196[756.9] − 0.800[1004.8]
723.3	1.0 − 0.154[42.8] − 0.243[123.1] − 0.013[248.0] − 0.014[625.2] −0.518[873.2] − 0.465[996.4]
873.2	(1.0 + 0.024{248.0}{625.2}/{873.2}) × (1.0 − 0.282[42.8] − 0.455[123.1] −0.894[723.3])
996.4	(1.0 + 0.507{123.1}{873.2}/{996.4} × (1.0 − 0.894[723.3])
1004.8	(1.0 + 0.221{248.0}{756.9}/{1004.8}) × (1.0 − 0.282[42.8] − 0.455[123.1] −0.217[591.7])
1274.4	(1.0 + 0.014{692.4]}{582.0}/{1274.4}) × (1.0 − 0.281[42.8] − 0.455[123.1])
1596.5	(1.0 + 5.568{873.2}{723.3}/{1596.5} + 2.094{1004.8}{591.7}/{1596.5} +0.052{1118.5}{478.3}/{1596.5} + 0.275{692.4}{904.1}/{1596.5}) ×(1.0 − 0.281[42.8] − 0.455[123.1])

Consideration: Dead time

The random nature of radioactive decay implies that some true events that occur too quickly following a prior event may be lost, due to the associated *dead time* of the counting or detection systems. The dead time is the amount of time that separates two events for them to be recorded as separate pulses. Unlike high-count rate experiments where "dead time losses" can become severe [27], the losses were negligible for E16032 due to the low count rates, although they were still applied. The ratio of accepted to total triggers for each digitizer that read out signals from the HPGe detectors that made up SeGA was used to calculate the dead-time correction.

With all these factors taken into consideration, the simulated detection efficiencies could then be compared to the experimental values as shown in Figure 3.17.

Simulating ion implantation

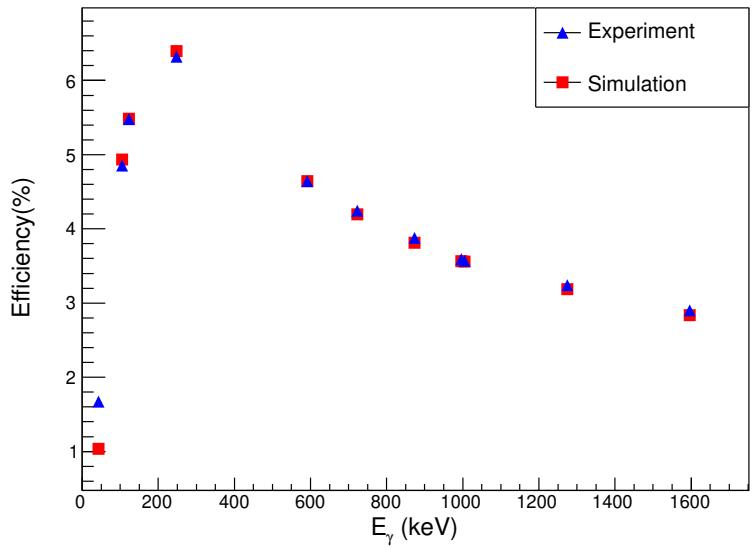

Figure 3.17: ***Benchmarking***: Simulated SeGA detection efficiencies (red boxes) compared to experimental detection efficiencies (blue triangles) for γ rays emitted by NIST-calibrated SRM source. Statistical error bars are unidentifiable as they are small relative to the squares and triangles representing the data points.

The excellent agreement between the simulation and experiment as described in Section 3.2.3.1 indicated that the model of the experimental setup was successfully benchmarked in GEANT4, and γ-ray emission following the decay of ions implanted within the $CeBr_3$ could be simulated for efficiency calibrations — the motivation of the simulation exercise. A mono-energetic, isotropically emitting point γ-ray source was placed within the volume of the $CeBr_3$ detector. The placement of the source was determined based on the implantation and depth profiles of ^{33}Na, which served as a reference for the secondary cocktail beam delivered to the experimental end station. Specifically, the x and y positions of the implanted point source were extracted from the 2D Lorentzian fit of the ion implantation profile of ^{33}Na, as described in Figure 3.12. The z position was defined as the midpoint of the implantation depth of ^{33}Na within the volume of the $CeBr_3$ implantation detector as calculated in LISE++, and shown in Figure 3.8.

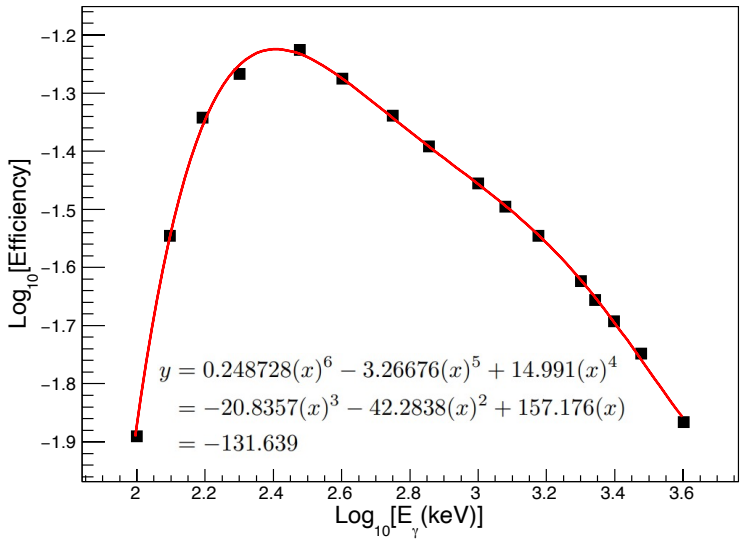

Figure 3.18: ***Implantation***: Simulated efficiency curve for γ rays with energies between 100 and 4000 keV emitted by a point source implanted in the $CeBr_3$ detector. Ease of fit was achieved by plotting the curve in log-log scale. The statistical errors are significantly smaller than the squares representing the data points (See text for details.)

The procedure described above was employed to determine the detection efficiency of the SeGA array for fifteen specific γ rays spanning energy values from 100 keV[4] to 4000 keV, as illustrated in Figure 3.18. γ-ray detection efficiencies for E16032 were then obtained by evaluating the sixth-order polynomial fit function represented by the red curve in Figure 3.18, and the mathematical expression superimposed on the plot, such that

$$Eff[E_\gamma](\%) = 100 \times 10^{[a(x)^6+b(x)^5+c(x)^4+d(x)^3+e(x)^2+f(x)+g]} \tag{3.7}$$

where E_γ is the γ-ray energy in keV, $x = \log_{10}[E_\gamma]$, and coefficients $a - g$ are the fit parameters associated with the corresponding fit function shown in Figure 3.18. A uniform 5% uncertainty was applied to the detection efficiencies for γ rays with energies exceeding 100 keV[5]. This uncertainty

[4]The transmission of γ rays with energy less than 100 keV from within the volume of the $CeBr_3$ detector was approximately less than 1%.

[5]It is worth noting that the γ-ray detection efficiency below 100 keV is uncertain for E16032.

assignment was based on information obtained during the benchmarking stage, during which the most substantial statistical uncertainties observed were below 5%, and found to be independent of the γ-ray energy.

Consideration: Implanted point versus volume γ-ray sources

The "beta-SeGA" configuration, as depicted in Figure 3.16(a), results in an averaging-out of the detection efficiencies between the upstream and downstream components of SeGA, positioned at uniform radial distances on opposite sides of the $CeBr_3$ implantation detector. Consequently, there is a negligible variance in the detection efficiencies for γ rays emitted from sources placed within the volume of the $CeBr_3$ implantation detector, whether it is a point or volume source as evident in Figure 3.19. To check this, an isotropically emitting volume γ-ray source was modeled after the implantation and depth distribution profiles of the secondary cocktail beam centered around ^{33}Na ions as shown in Figure 3.12 and Figure 3.8, respectively. This was achieved by creating a cylindrical γ-ray source in GEANT4, with its dimensions defined using the General Particle Source (GPS) functionality as

```
/gps/pos/type Volume
/gps/pos/shape Cylinder
/gps/pos/centre x y z cm
/gps/pos/radius r cm
/gps/pos/halfz z cm.
```

Specifically, the x and y values were obtained by subtracting the center of the pixelized PSPMT grid (8,8) from the position parameters of the 2D Lorentzian function used to fit the ion implantation profile, before converting to cm. The z position was taken as the magnitude of the distance from the face of the $CeBr_3$ detector to the center of the ion depth profile, added to the distance from center of the world to the face of the $CeBr_3$ implantation detector. "`/gps/pos/halfz`" represented half

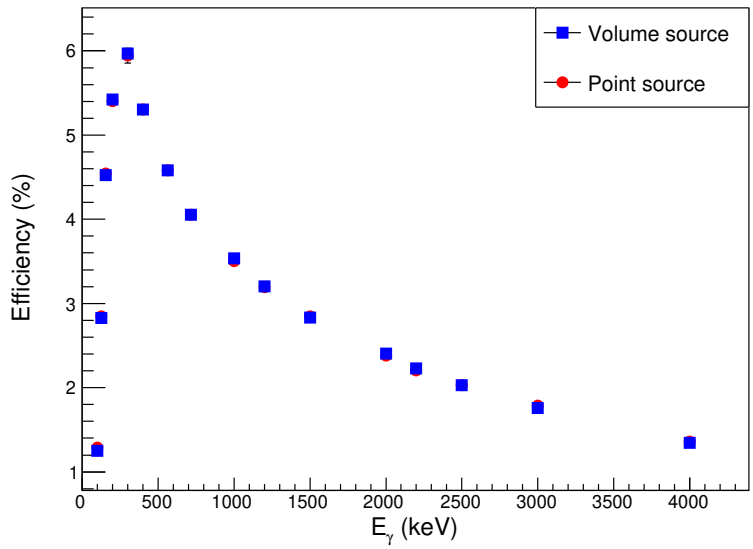

Figure 3.19: Simulated SeGA detection efficiencies for γ rays with energies between 100 and 4000 keV emitted by a point source (red circles) compared to a volume source (blue boxes) implanted within the $CeBr_3$ detector.

the height of the cylinder, taken from the implantation depth divided by 2. The radius, r of the cylinder was defined as

$$r = \sqrt{\Gamma_x^2 + \Gamma_y^2} \tag{3.8}$$

where Γ_x^2 and Γ_y^2 are the widths of the 2D Lorentzian fit function along the x and y axes, respectively.

It is important to note that each detector was treated independently in the analysis. In fact, the utilization of specific characteristics of individual detectors, such as their positions, proved to be crucial for achieving accurate efficiencies. Moreover, energy calibrations for source measurements were conducted utilizing the same photopeaks as those mentioned for efficiency calibrations. It should be noted that these photopeaks are distinct from the ones used during data runs.

SeGA energy calibrations

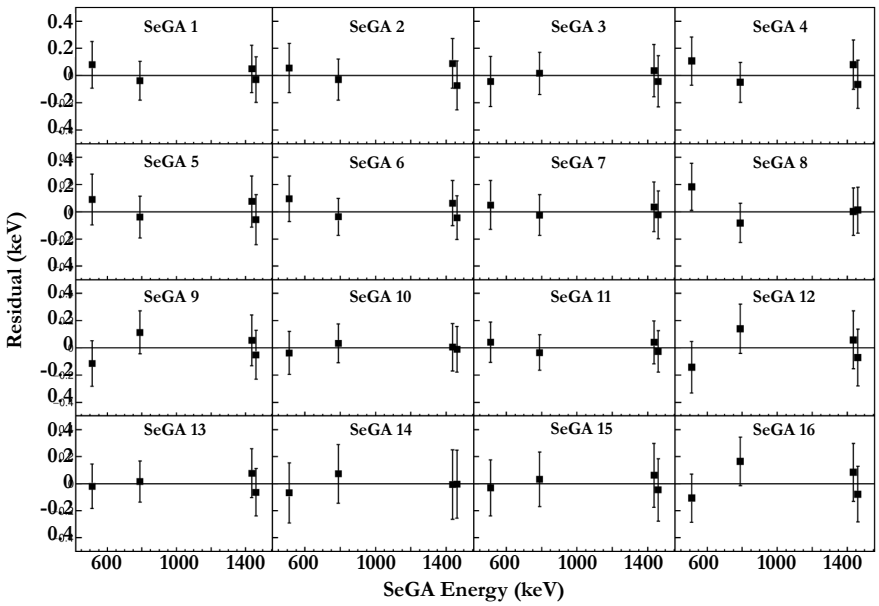

Figure 3.20: Energy calibration residuals for individual HPGe detectors in the SeGA array for a representative E16032 data run. The uncertainty in the centroid position from Gaussian fits to each uncalibrated photopeak is shown by the error bars.

A characteristic of the HPGe detectors is their excellent energy resolution which is necessary for γ-ray spectroscopy and allows for reliably separating closely lying peaks in a γ-ray spectrum. An additional appeal of HPGe detectors is the capability to extend their application over a wide range of energies from a few keV to several MeV [15].

A linear energy calibration was performed on the HPGe detectors that make up SeGA given their small degree of non-linearity [27]. This was achieved for every data run in E16032 using photopeaks corresponding to four well-known γ-ray energies including 511.00 keV from electron-positron annihilation, 788.74 keV and 1434.80 keV from ^{138}La intrinsic activity, and 1460.82 keV from ^{40}K decay. Specifically, calibrations were performed by extracting the centroid location from the Gaussian fits to the four photopeaks in the uncalibrated γ-ray energy spectrum, then plotting

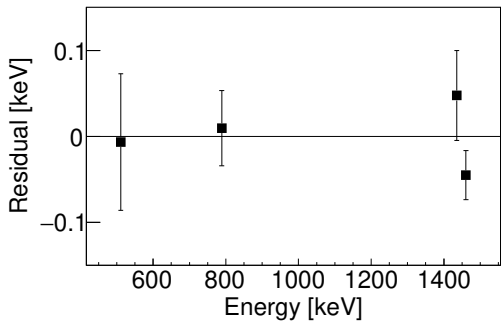

Figure 3.21: Energy calibration residuals of the summed spectrum of all detectors that make up SeGA for a typical experiment E16032 data run.

the centroids against their known γ-ray energies. The slope, m and intercept, c of the linear fit for each detector in the SeGA array was extracted and applied for calibration such that

$$E_\gamma(keV) = mx + c \tag{3.9}$$

where x is the channel number or uncalibrated photopeak centroid in arbitrary units.

Residuals for each HPGe detector that makes up the SeGA array are shown for a typical E16032 data run in Figure 3.20, while those for the sum spectrum of all SeGA detectors for the same run are shown in Figure 3.21. The residuals ensure confidence in the calibration applied for experiment E16032 given that the distributions are not energy dependent. Notably, the residuals consistently measured below 0.1 keV, as illustrated for a typical run in Figure 3.21, informing the application of an energy calibration uncertainty of ± 0.2 keV for all measured γ-ray energies in experiment E16032.

3.2.3.2 Cerium-doped lanthanum bromide ($LaBr_3$(Ce)) scintillators

The second array of γ-ray detectors consisted of 15 $LaBr_3$(Ce) detectors placed in rings at 90° with respect to the beam axis. Each detector was made up of a 1.5 × 1.5-inch right-cylindrical

$LaBr_3$(Ce) crystal, each placed around the $CeBr_3$ implantation detector in a ring perpendicular to the beam direction. The $LaBr_3$(Ce) detectors have reasonable timing and energy resolution optimal for fast-timing measurements [32]. Energy calibrations were carried out using a similar technique and well-known photopeaks as discussed in Section3.2.3.1.

$LaBr_3$(Ce) - PSPMT dynode time alignment

The time difference distributions presented in Chapter IV of this dissertation represent the cumulative time differences between each $LaBr_3$(Ce) detector and the PSPMT dynode. These time differences were calculated for events where a β-decay electron correlated to an implant of interest was detected in the $CeBr_3$ implantation detector (start time), and a γ-ray transition from an isomeric state of interest was detected in one of the surrounding $LaBr_3$(Ce) detectors (stop time). The intrinsic timing properties of each $LaBr_3$(Ce) detector used in the E16032 setup must therefore be taken into account. By determining the time difference for each $LaBr_3$(Ce) detector with respect to the PSPMT dynode time, all detectors can be aligned to a common time reference, such as setting them to zero as shown in Figure 3.22(a) and (b)[6].

A ^{60}Co source run was used for the alignment, allowing for a majority of events to be prompt true coincidences. The main structure appearing as prompt in the time difference distribution in Figure 3.22(a) and (b) reflects this characteristic. Additional information on the reasoning behind its use is presented in Section 4.3 of Chapter IV. The structures observed to the left and right of the prompt distribution in Figure 3.22(a), (b), and (c) are a result of the energy-dependent time walk effects originating from the PSPMT dynode and individual $LaBr_3$(Ce) detectors, respectively. Addressing the treatment of these timewalk effects is beyond the scope of this dissertation. Consequently, only the prompt timing responses were incorporated into the alignment process.

[6]It should be noted that an arbitrary offset of 1000 ns was added to the time differences for data runs.

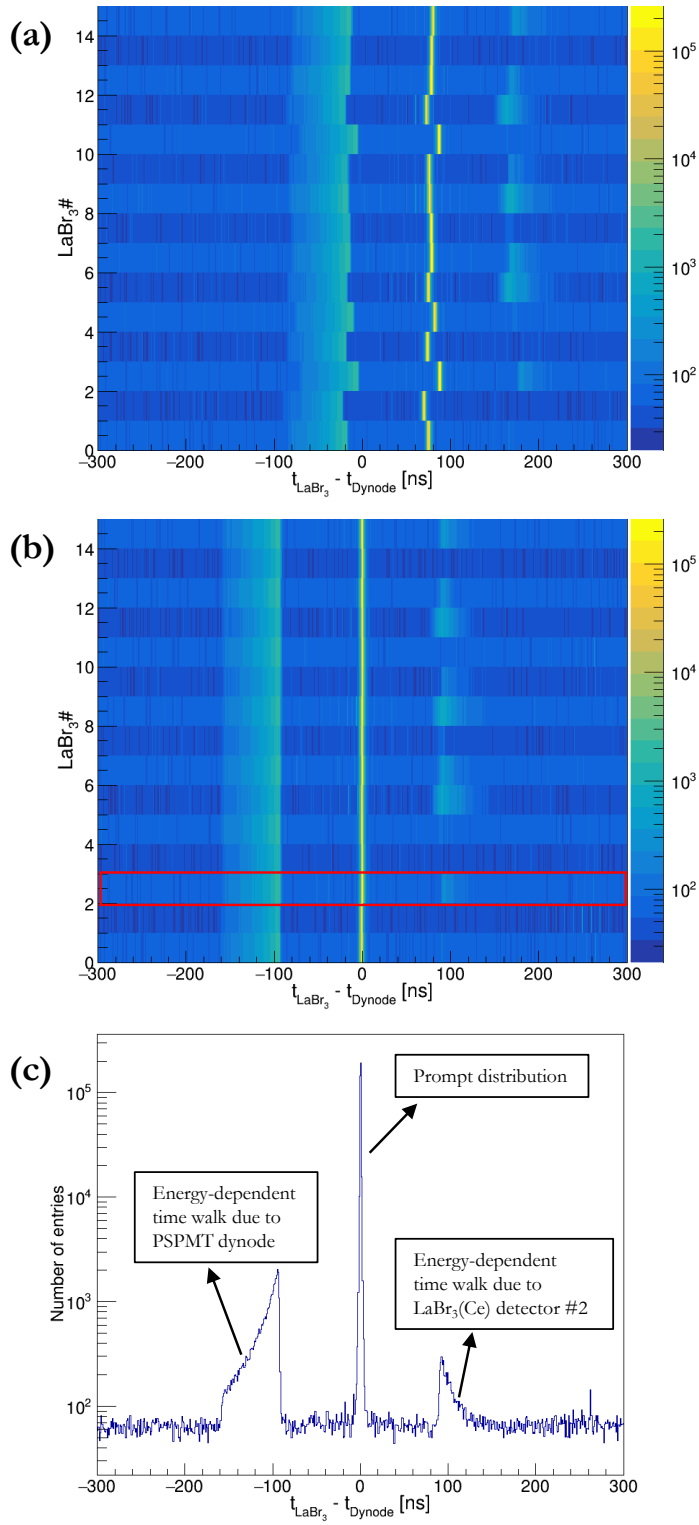

Figure 3.22: Two-dimensional histogram of the $LaBr_3(Ce)$ detector number plotted against the $LaBr_3(Ce)$ - PSMPT dynode time difference **(a)** before and **(b)** after alignment using a ^{60}Co source. **(c)** 1D projection of $LaBr_3(Ce)$ #2 - PSPMT Dynode pair defined by the red graphical cut in (b). (See text for additional information.)

CHAPTER IV

RESULTS AND DISCUSSION: HALF-LIFE MEASUREMENT OF ISOMERIC STATES IN ^{37}SI ACCESSED VIA BETA DECAY

Low-lying excited ($7/2^-_1$) and ($3/2^-_1$) states at 68 and 156 keV were first established in the level scheme of ^{37}Si through previous studies involving the β^- [65, 4] and β^-n [65] decays of ^{37}Al and ^{38}Al, respectively. The ($3/2^-_1$) state was subsequently characterized as a nanosecond isomer in a further investigation of the structure of ^{37}Si in a ^{9}Be(^{38}Si, ^{37}Siγ) reaction, with its half-life measured as 3.0(7) ns [67]. One of the objectives of this experiment was to investigate the ($7/2^-_1$) state in ^{37}Si and determine its half-life, which has not been measured previously. The ($7/2^-_1$) state, along with the ($3/2^-_1$) state in ^{37}Si, was predicted to be an isomeric state according to Ref. [67].

These isomeric states were accessed via the β^- and $\beta^- n$ decay of implanted ^{37}Al and ^{38}Al ions, respectively. In this chapter, analysis that led to the determination of the half-life of the ($3/2^-_1$) state is first discussed. This preliminary analysis served as a validation of the novel fast-timing measurement method employed in this study. Alternative methods for performing the half-life measurement of the ($3/2^-_1$) state are also presented. Subsequently, the half-life measurement of the ($7/2^-_1$) state is presented, providing crucial information about its decay properties. Additionally, these excited states were further characterized by extracting the reduced transition probabilities for the aforementioned isomeric transitions to the ($5/2^-_1$) ground state of ^{37}Si, as reported in Ref. [47].

Lastly, a comparison of experimental measurements with theoretical predictions obtained from shell model calculations using the SDPF-MU [72], SDPF-U-SI [44], and FSU [34] interactions are presented, and inferences on the shell structure implications of the findings are provided.

4.1 ^{37}Al decay

Figure 4.1 shows the level scheme of ^{37}Si adapted from experimental results of previous β-decay studies of ^{37}Al in Refs. [65, 4]. The level scheme, constructed using β-delayed γ-ray spectroscopy shows that the low-lying negative-parity states in ^{37}Si are not fed directly in ^{37}Al β^- decay. Instead, they are populated following γ-ray decay from higher-lying positive-parity states which are preferentially fed in ^{37}Al β^- decay. This is consistent with expectations outlined in Section 2.2.2 of Chapter II such that β-decay selection rules dictate what states are populated in ^{37}Si following the β decay of the positive-parity ($5/2^+$) ground state of ^{37}Al. These rules limit the population of states in ^{37}Si such that those with the same parity as the ground state of the ^{37}Al parent nucleus are preferentially populated as depicted in Figure 4.1.

4.1.1 β-delayed γ-ray spectrum following ^{37}Al decay

Constructing nuclear level schemes and inferring nuclear structure properties of radioactive nuclei heavily relies on γ-ray spectroscopy. This technique involves the study of β-delayed γ rays and plays a vital role in the analysis presented in this chapter. Additionally, the fast-timing method utilized in this dissertation to extract the half-lives of interest requires the application of γ-ray spectroscopy. In order to generate a β-delayed γ-ray spectrum correlated to ^{37}Al implants and optimize the observation of γ rays originating from de-excitations in ^{37}Si, the following conditions were satisfied:

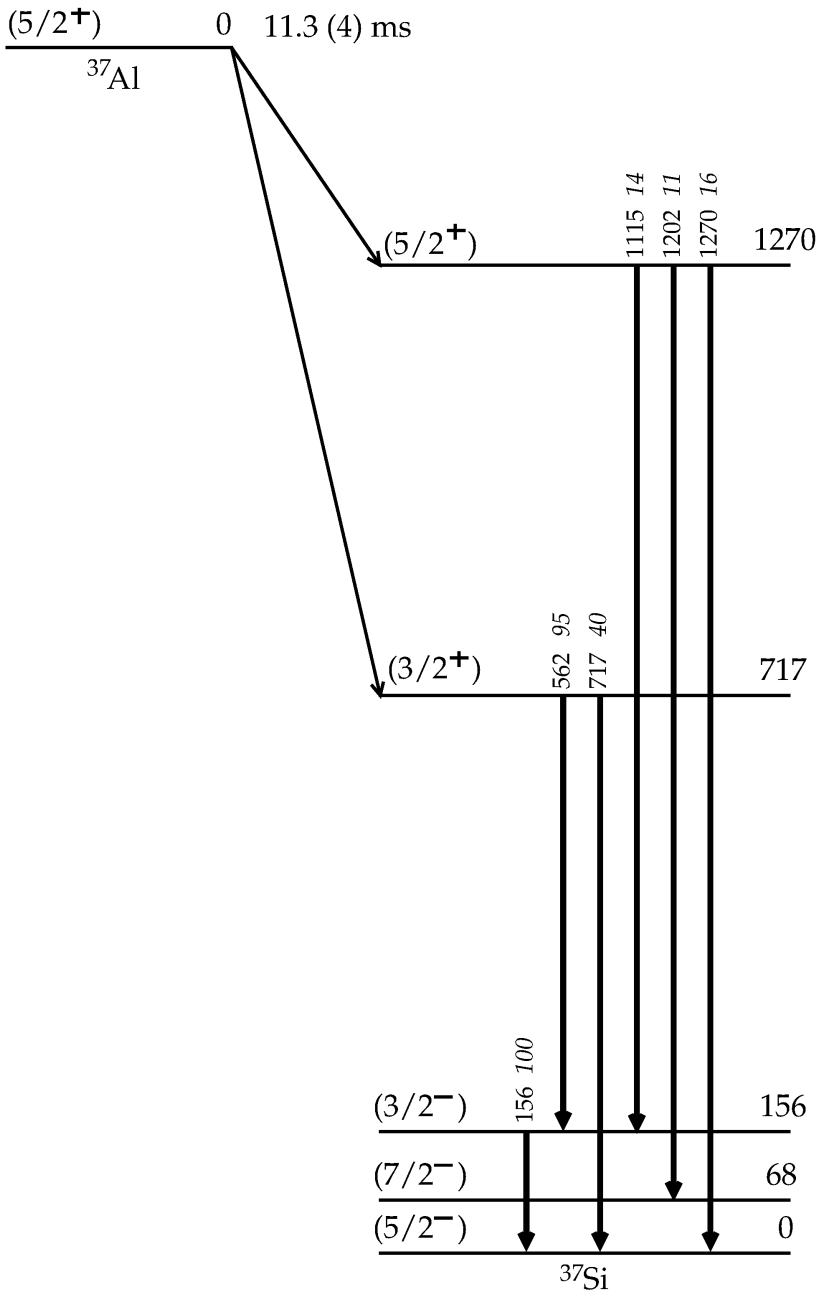

Figure 4.1: Experimental level scheme of ^{37}Si following the decay of ^{37}Al. β decay preferentially populates the higher-lying positive-parity states which de-excite to lower-lying negative-parity states via γ-ray decay. γ-ray transitions are represented by downward pointing arrows between states defined by their tentative spins and parities (left) and energies (right) on the horizontal lines. The figure is adapted from Refs. [65, 4]

I Graphical cut corresponding to "*good*" ^{37}Al implants on particle identification plot. The PID is shown in Figure 3.7 of Chapter III.

II *"Good"* correlations where "*good*" decays were correlated to "*good*" ^{37}Al implants.

III *Reasonable β decay - ^{37}Al ion correlation window* of 33.9 ms which corresponds to three ^{37}Al β-decay half-lives ($T_{1/2}$ = 11.3 ms). The "*good*" implant and decay conditions are described in Subsection 3.2.2.2 of Chapter III.

IV *Random correlation identification and subtraction* to isolate β-delayed γ rays arising from ^{37}Al decay using methods described in Refs. [65, 28].

For this dataset, a β-delayed γ-ray spectrum "*reverse-correlated*" to ^{37}Al implants was subtracted from a "*forward-correlated*" spectrum with the same conditions listed above fulfilled. "*Forward correlation*" will limit the population of a β-delayed γ ray spectrum to transitions that are observed in the SeGA array after the decay of ^{37}Al implants (in positive times only). Transitions that arise from ^{37}Al decay as well as background γ rays are observed in such spectra. In a "*reverse-correlated*" spectrum however, transitions that arise following ^{37}Al decay will be absent (negative times only), while random γ rays from before the correlation will remain present. Therefore, a photopeak like the 1460-keV background γ ray that arises from ^{40}K decay, observed in the superimposed *forward-* and *reverse-correlated* spectra in Figure 4.2(b) will be dramatically reduced in a random correlation subtracted spectrum as shown in Figure 4.3. Other examples include background transitions due to e^-e^+ annihilation (511 keV), and $LaBr_3$ internal activity (788 and 1435 keV). These photopeaks can be compared to the 1409-keV photopeak, for example, which corresponds to a transition in the ^{36}Si β^-n daughter of ^{37}Al, is absent in the spectrum "*reverse-correlated*"

to ^{37}Al, and retains its intensity in the random correlation subtracted histogram as shown in Figure 4.2(b) and Figure 4.3, respectively.

The random correlation subtracted β-delayed γ-ray spectrum following ^{37}Al decay is shown in Figure 4.3. The transitions attributed to ^{37}Si in this work are in agreement with measurements from previous β-decay experiments in Refs. [65, 4]. These include γ-γ coincidences between the 562- and 1115-keV transitions and the 156-keV transition, as shown in Figure 4.4, confirming the presence of the 717- and 1270-keV positive-parity states preferentially populated in the β decay of ^{37}Al. These positive-parity states de-excite by γ rays that feed the negative-parity, low-lying states at 156 and 68 keV. They also correspond to crossover γ-ray transitions with energies, 717 and 1270 keV, respectively.

Consideration: Non-observation of the 68-keV transition in ^{37}Si following decay of ^{37}Al.

The observation of γ rays that de-excite isomeric states of interest is necessary for the application of the fast-timing method discussed in this chapter. The very intense 156-keV γ ray observed in Figure 4.3 is attributed to the de-excitation of the $(3/2^-_1)$ state at 156 keV. A 68-keV γ ray which would correspond to a ground-state transition from the $(7/2^-_1)$ state is, however, not observed in the γ-ray spectrum correlated to ^{37}Al, similar to findings in Refs. [65, 4] and may be due to a confluence of reasons explained below:

I ***$(7/2^-_1)$ state population mechanism***: Primarily, the direct population of the $(7/2^-_1)$ state at 68 keV may be hindered in the β^- decay of ^{37}Al. The state is expected to be weakly fed by the 1202-keV γ-ray transition that de-excites the 1270-keV state as discussed in Ref. [65]. This consequently impedes the observation of the 68-keV γ ray in the spectrum correlated

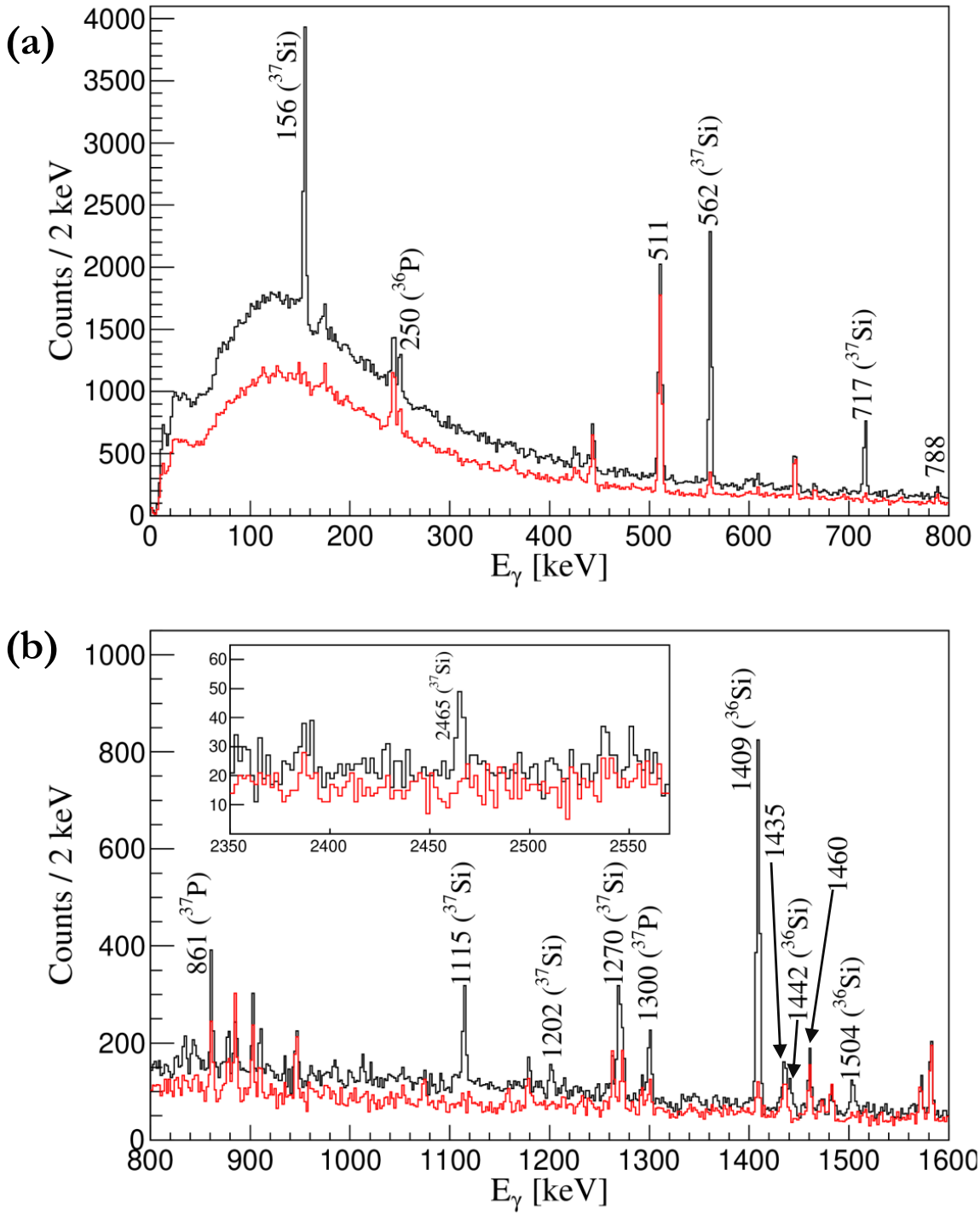

Figure 4.2: **(a,b)** Superimposition of *forward-correlated* (black) and *reverse-correlated* (red) β-delayed γ-ray spectra following ^{37}Al decay. (See text and Figure 4.3 for additional information.)

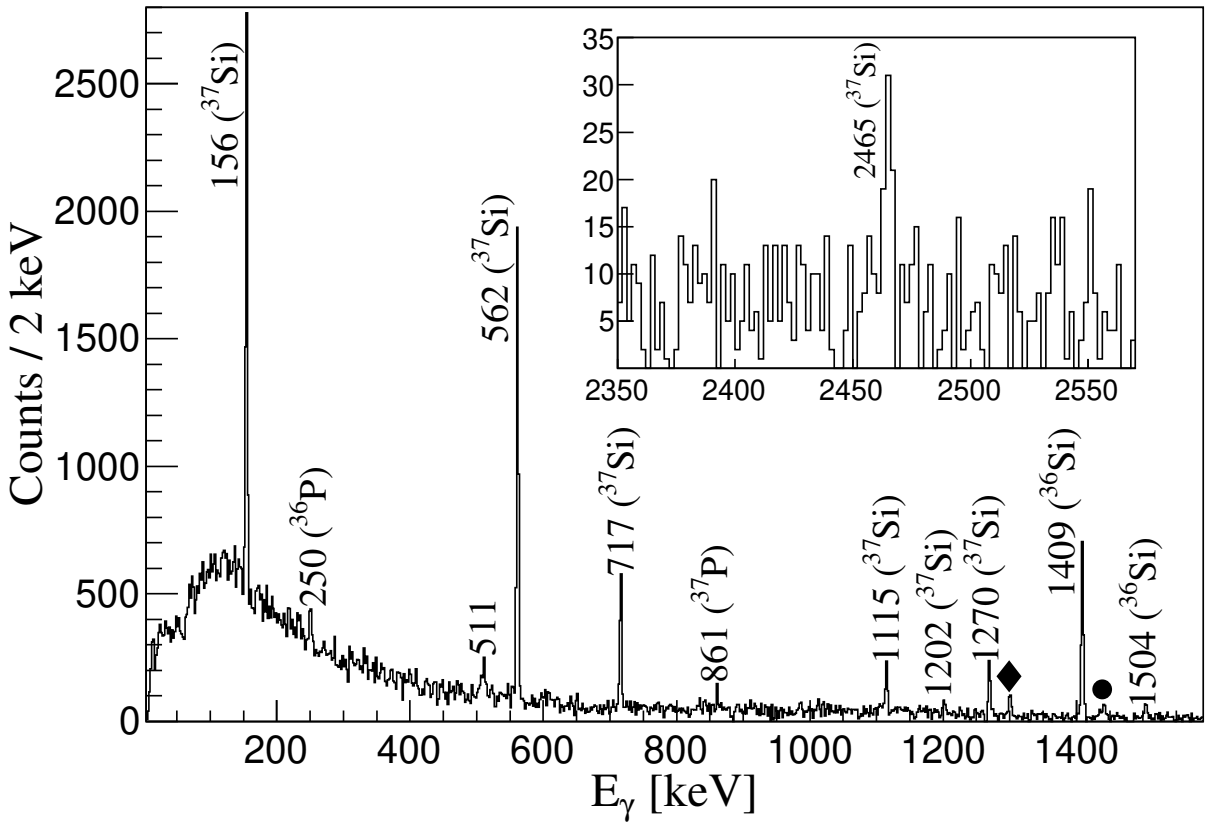

Figure 4.3: β-delayed γ-ray spectrum for γ rays detected in the SeGA detectors within a correlation window of 33.9 ms, which corresponds to three ^{37}Al β-decay half-lives ($T_{1/2}$ = 11.3 ms.) Previously observed γ-ray transitions in the ^{37}Si daughter [67, 65, 4] are labeled with their respective energies, as well as transitions in the β-delayed one-neutron emission ^{36}Si daughter and ^{36,37}P granddaughters. Other identified γ-ray transitions include the 1300 keV in ^{37}P (black diamond), the 1442 keV in ^{36}Si (black circle) and the 511 keV due to e^-e^+ annihilation. ***Inset***: Region around newly observed 2465-keV γ-ray transition.

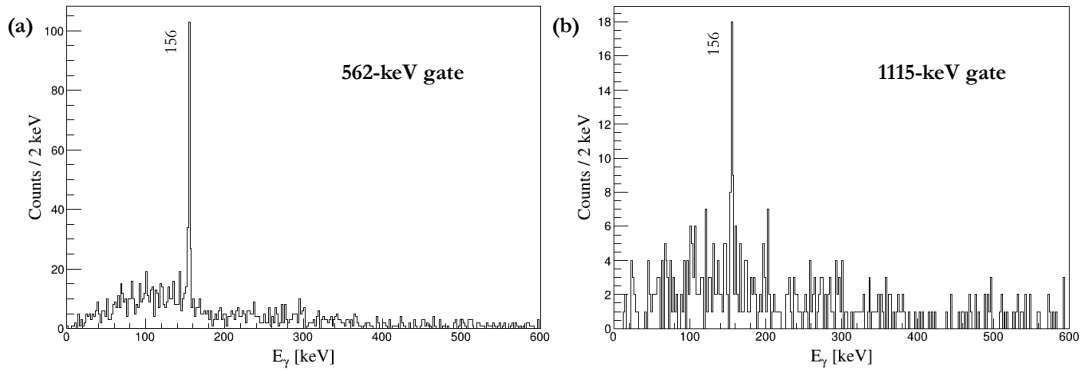

Figure 4.4: γ-ray spectra in coincidence with the 562-keV (a) and 1115-keV transitions in ^{37}Si.

to ^{37}Al, unlike the 156-keV γ-ray transition whose corresponding state is strongly populated via both intense 562- and 1115-keV transitions.

II ***Attenuation in the high-Z $CeBr_3$ implantation detector***: The high sensitivity of the $CeBr_3$ implantation detector to low-energy γ rays will most probably impede the detection of such a weakly fed transition like the 68-keV in ancillary γ-ray detectors. This is confirmed by GEANT4 Monte Carlo simulation [5] results which show that the detection efficiency of the $CeBr_3$ implantation detector exceeds 95% for γ rays less than 100 keV. While it is expected that nearly all of the 68-keV γ rays will be stopped within the $CeBr_3$ implantation detector, β-decay electrons also depositing an appreciable amount of energy in the detector will prevent the observation of a distinct 68-keV γ-ray peak in a corresponding $CeBr_3$ energy spectrum, as the two energy depositions will sum together.

Consideration: Unplaced 2465-keV transition

None of the other transitions observed in the one-neutron knockout reaction in Ref. [67] were identified in the γ-ray spectrum correlated to ^{37}Al implants in this work. However, a 2465-keV γ ray was observed as shown in the inset of Figure 4.3. The 2465-keV γ-ray transition is attributed to

^{37}Si, primarily due to the fact that shell model calculations using the FSU interaction [34] predict candidate excited states close in excitation energy that can be populated by allowed transitions in the β decay of ^{37}Al. Moreover, no coincident γ ray was observed for the 2465-keV transition, as illustrated in Figure 4.5. However, it is important to note that the low intensity of this transition introduces statistical limitations to the analysis, and therefore, definitive conclusions cannot be drawn.

Another detail worth considering is the 2.21(13)-MeV one-neutron separation energy, S_n of ^{37}Si [74], compared to a probable 2465-keV candidate excited state that may decay to the $(5/2^-_1)$ ground state. Excited states above the S_n will decay via γ or neutron emission, the latter likely winning the competition and resulting in the population of states in a $\beta^- n$ daughter with energy values of $E_x - S_n$, where E_x is the excitation energy of the state decaying via neutron emission. However, neutron emission is expected to be less favored in a spin-parity mismatch, especially considering that the 0^+ ground state in ^{36}Si is the only energetically accessible state in this scenario. This is because there are no excited states with energies within the vicinity of ~200 keV available for population in ^{36}Si, indicating that the 2465-keV γ-ray transition is most-likely attributable to ^{37}Si. Further investigations can be conducted in future experiments with sufficiently high statistics and the utilization of arrays specifically designed for β-delayed neutron emission measurements.

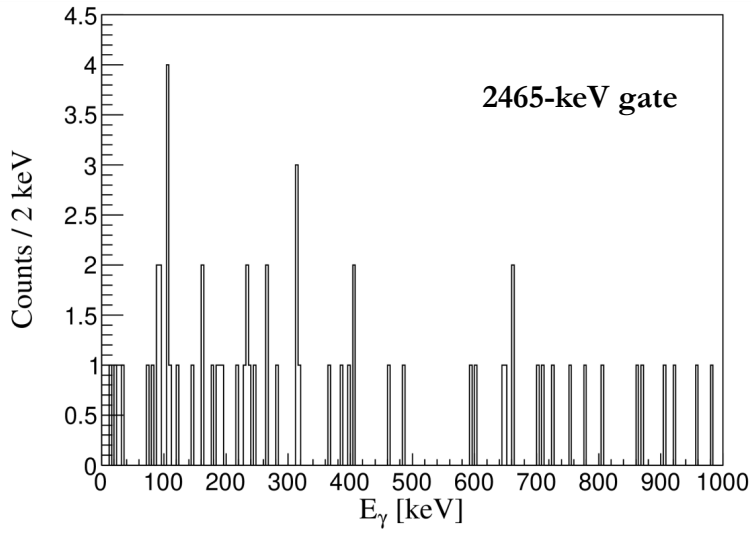

Figure 4.5: γ-ray spectrum in coincidence with the 2465-keV transition in ^{37}Si.

Consideration: Relative intensities of γ-ray transitions in ^{37}Si; validation of γ-ray spectroscopy measurements.

The consistency of γ-ray spectroscopy measurements in this work was assessed by comparing the intensities of the observed γ rays with those reported in a previous study in Ref. [65]. This is shown in Table 4.1 for γ rays attributed to ^{36}Si and ^{37}Si following the decay of ^{37}Al. The intensities were corrected for the detection efficiencies of the SeGA array in this experiment as discussed in Section 3.2.3.1 of Chapter III, and normalized relative to the intensity of the 156-keV transition in ^{37}Si. The table demonstrates that the intensities obtained in this experiment are in agreement with the measurements reported in previous studies.

4.2 ^{38}Al decay

The 68-keV state in ^{37}Si is strongly populated in the β^-n decay of ^{38}Al. As depicted in the level scheme in Figure 4.6 adapted from Ref. [65], the β-decaying states in ^{38}Al responsible for populating the low-lying states in ^{37}Si have not been disentangled. However, γ rays at 68 and 156

Table 4.1: Relative intensities of γ rays attributed to ^{36,37}Si observed in the SeGA detectors following the β decay of implanted ^{37}Al ions. The intensities are normalized to the intensity of the 156-keV transition in ^{37}Si and have been corrected for the SeGA detection efficiency simulated in GEANT4[5]. γ-ray transitions in the ^{36}Si β^-n daughter have been identified with an asterisk. The intensities are compared with results presented in Ref. [65].

E_γ (keV)	$I_{\gamma,exp.}$	$I_{\gamma,lit.}$ [65]
155.8(2)	100(6)	100(4)
562.8(2)	88(5)	95(6)
716.6(2)	31(2)	40(4)
1115.0(3)	15(1)	14(4)
1201.5(3)	7(1)	11(4)
1269.6(2)	16(2)	16(4)
1409.2(2)*	59(4)	71(7)
1441.5(4)*	4(1)	9(3)
1503.8(3)*	4(1)	10(3)
2464.9(4)	2(1)	-

keV are attributed to ground-state transitions from the $(7/2^-_1)$ and $(3/2^-_1)$ states in ^{37}Si, respectively. The attribution of these transitions to ^{37}Si follow discussions proposed in Ref. [65].

4.2.1 β-delayed γ-ray spectrum following ^{38}Al decay

Figure 4.7 shows the random correlation subtracted β-delayed γ-ray spectrum following ^{38}Al decay. The spectrum was produced using the same technique discussed in Section 4.1.1, with a β decay - ^{38}Al ion correlation window of 27 ms, which corresponds to three ^{38}Al β-decay half-lives ($T_{1/2}$ = 9 ms). As highlighted in Figure 4.7, a 68-keV photopeak is clearly observed in the γ-ray spectrum correlated to the ^{38}Al ions. Arguments have been made in Section 4.1.1 and Refs. [65, 4] concerning the placement of a corresponding 68-keV state in ^{37}Si, as well as the non-observation of a 68-keV photopeak in the β-delayed γ-ray spectrum correlated to ^{37}Al. The non-observation of transitions assigned to the ^{38}Si daughter in γ-γ coincidence measurements with the 68-keV

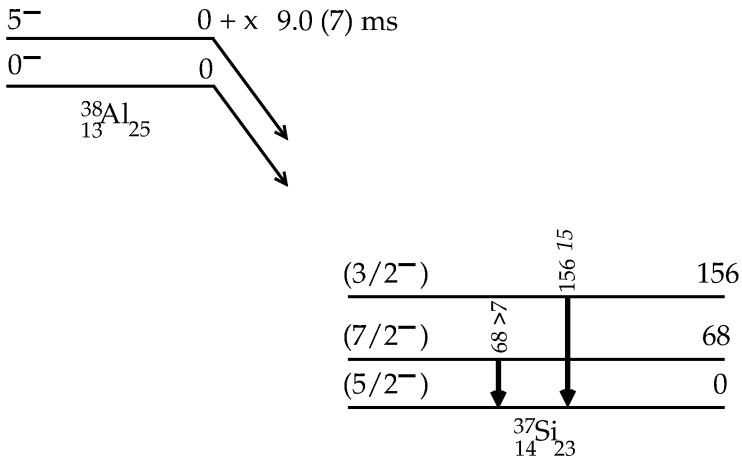

Figure 4.6: Experimental level scheme of ^{37}Si following $\beta^- n$ decay of ^{38}Al, adapted from Ref. [65].

transition following the β^-n decay of ^{38}Al in this work supports the attribution of this γ ray to the ground-state transition from the $(7/2^-_1)$ state in ^{37}Si as its most probable origin. This is shown in Figure 4.8(a). A similar argument can also be made for the placement of the $(3/2^-_1)$ state at 156 keV following ^{38}Al β^-n decay (see Figure 4.8(b)).

Table 4.2 shows the relative intensities of the γ rays observed in the SeGA detectors and attributed to the ^{38}Si β^- and ^{37}Si β^-n daughters, respectively. The intensities were efficiency-corrected and normalized to that of the 1074-keV γ ray in ^{38}Si. They also appear consistent with measurements reported in Ref. [65].

4.3 Half-life measurement of the $(3/2^-_1)$ state in ^{37}Si and validation of the β-γ fast-timing method

The half-life of the $(3/2^-_1)$ state was previously extracted by broadened line shape analysis of the Doppler-reconstructed γ-ray spectrum in coincidence with ^{37}Si residues following a ^{9}Be(^{38}Si, ^{37}Siγ) reaction [67]. The utilization of the fast $CeBr_3$ implantation detector and ancillary $LaBr_3$(Ce)

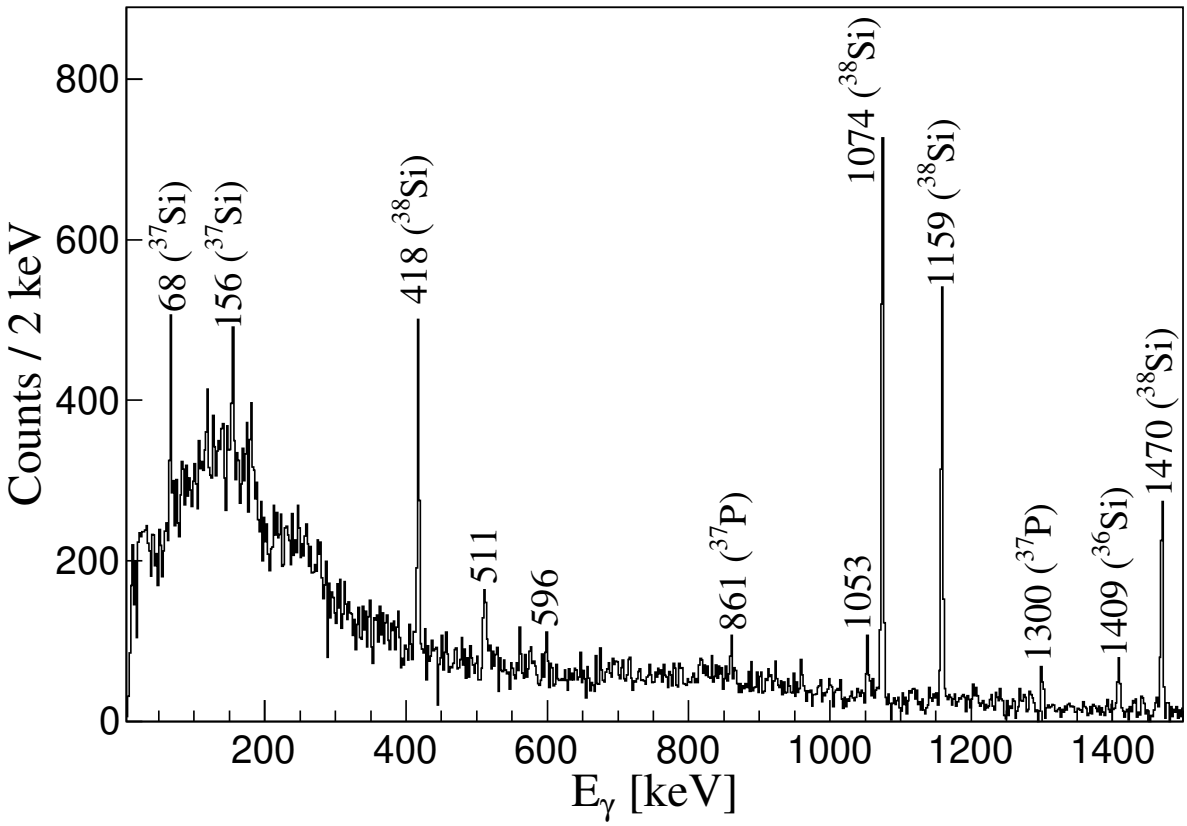

Figure 4.7: β-delayed γ ray spectrum for γ rays detected in the SeGA detectors within a correlation window of 27 ms, which corresponds to three ^{38}Al β-decay half-lives ($T_{1/2}$ = 9 ms). Previously observed γ-ray transitions in the ^{38}Si daughter and the ^{37}Si β-delayed one-neutron emission daughter are labeled with their respective energies. Transitions attributed to ^{36}Si and ^{37}P are also identified as well as the 511 keV due to e^-e^+ annihilation and 596 keV due to (n,n',γ) reactions on ^{74}Ge nuclei of the HPGe detectors. A currently unplaced 1053-keV γ-ray transition is also observed.

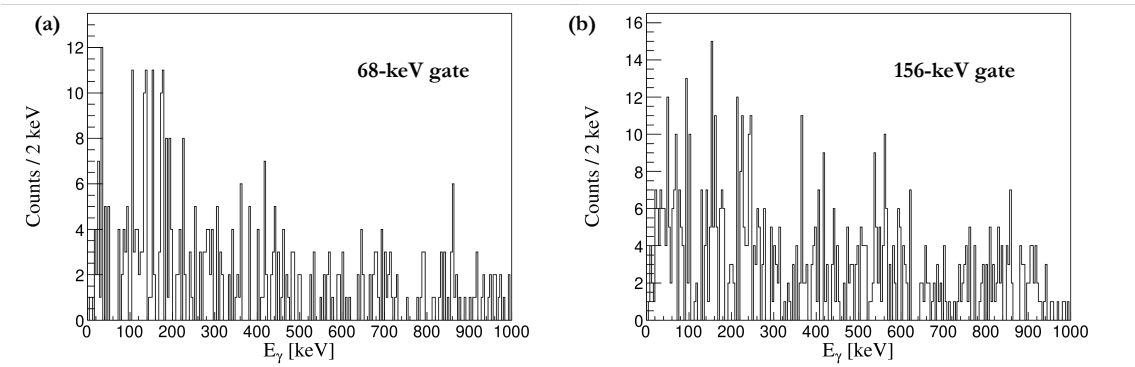

Figure 4.8: γ-ray spectra in coincidence with the (**a**) 68-keV and (**b**) 156-keV transitions in ^{37}Si, respectively following the β decay of ^{38}Al.

detectors in this experimental setup allowed for the direct measurement of half-lives of isomeric states populated following the β decay of implanted ions, including the $(3/2^-_1)$ state that decays to the $(5/2^-_1)$ ground state in ^{37}Si via the emission of a corresponding 156-keV γ ray. The β-γ fast-timing method established in Ref. [36] and further discussed in Refs. [56, 14] was applied to carry out this measurement by calculating the time difference for events where a β-decay electron correlated to a ^{37}Al ion was detected in the $CeBr_3$ implantation detector (start time) and a 156-keV γ ray was detected in one of the surrounding $LaBr_3$(Ce) detectors (stop time).

Figure 4.9(a) shows the time difference distribution between the $LaBr_3$(Ce) array and the $CeBr_3$ implantation detector — readout by the PSPMT dynode, and referred to as the dynode going forward — as a function of energy in the $LaBr_3$(Ce) detectors using the same conditions outlined in Sec. 4.1.1. A time difference distribution to the right of the prompt distribution at 1000 ns is evident for the 156-keV γ-ray transition[1]. Other γ-ray transitions with measurable half-lives are also observable at different intensities. These γ rays likely correspond to transitions associated with isomeric states in daughter nuclei resulting from the decay of ^{37}Al, or they may originate from

[1]It should be noted that the time difference axis was arbitrarily offset by 1000 ns.

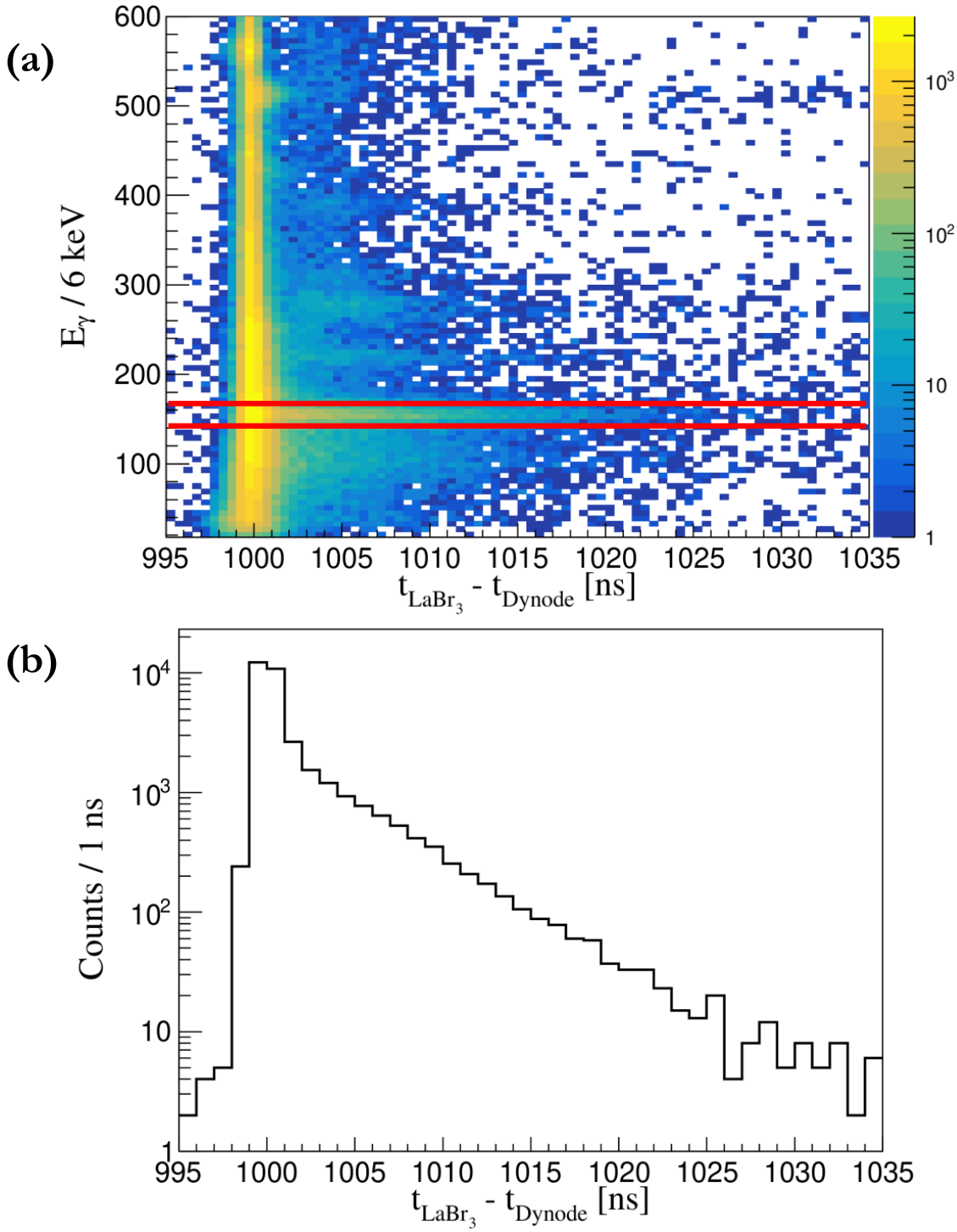

Figure 4.9: **(a)** 2D plot of energies of γ rays detected in the $LaBr_3(Ce)$ detectors within 33.9 ms of ^{37}Al ion implantation versus time difference between the $LaBr_3(Ce)$ and PSPMT dynode. **(b)** 1D projection of the 156-keV photopeak (red graphical cut in (a)) on the time difference axis.

Table 4.2: Relative intensities of γ rays attributed to ^{37,38}Si observed in the SeGA detectors following the β decay of implanted ^{38}Al ions. The intensities are normalized to the intensity of the 1074-keV transition in ^{38}Si and have been corrected for the SeGA detection efficiency simulated in GEANT4. The γ-ray transitions in ^{37}Si are identified with an asterisk and intensities are compared with results presented in Ref. [65]. It should be noted that γ-ray detection efficiency below 100 keV is uncertain.

E_γ (keV)	$I_{\gamma,exp.}$	$I_{\gamma,lit.}$ [65]
67.9(2)*	500(200)	>7
155.5(3)*	12(3)	15(7)
417.9(2)	33(4)	32(5)
1074.3(2)	100(7)	100(12)
1158.7(2)	74(7)	59(7)
1470.0(2)	46(5)	42(5)

randomly correlated long-lived daughters. Additionally, there may be contributions from other internal sources based on the experimental data.

Half-life measurement technique

The exponentially decaying characteristic of the time difference distribution due to the 156-keV transition can be better observed in one-dimension by placing a graphical cut on the 156-keV energy region and making a projection along the time difference axis, as shown in Figure 4.9(b). Although the half-life of the $(3/2^-_1)$ state of interest is sufficiently long such that it appears as (and may be defined solely by) the slope of the delayed portion of the time difference distribution, a precise half-life measurement necessitates a model that considers contributions from both the prompt and delayed portions of the distribution. This modeling approach becomes particularly vital when applied to the $(7/2^-_1)$ state in E16032, where the associated time difference distribution exhibits low statistics. The half-life measurement technique outlined in Ref. [14] was adapted for application in the context of E16032, starting with the $(3/2^-_1)$ state for validation of the method,

before employing it to measure the half-life of the $(7/2^-_1)$ state. The time difference distribution associated with the 156-keV transition in Figure 4.9(b) can be deconstructed into two distinct components, as explained below:

- ***Prompt component***: This component of the time difference distribution represents the prompt Gaussian response of the fast-timing measurement setup. In this region, there are also distributions involving half-lives much shorter than the timing resolution of the detectors used in the experimental setup. The prompt component is characterized with the Gaussian function

$$f(t, t_0, E_\gamma, E_D) = \exp\left[-\frac{1}{2}\left(\frac{(t - t_0)}{\sigma(E_\gamma, E_D)}\right)^2\right] \tag{4.1}$$

  where t_0 is the centroid and $\sigma(E_\gamma, E_D)$ is time response width, which is implicitly dependent on the γ-ray energy of interest, E_γ, and the distribution of the dynode energy, E_D, corresponding to the coincidentally detected β-decay electron.

- ***Delayed component***: This is the component of the time difference distribution that represents the exponential decay of the isomeric state of interest. It is characterized by the exponential function

$$g(t, t_0, \tau) = \exp\left[-\frac{(t - t_0)}{\tau}\right] \tag{4.2}$$

  where t_0 is the centroid, and τ is the lifetime of the isomeric state. τ is related to the half-life $T_{1/2}$ with the expression

$$T_{1/2} = 0.693\tau. \tag{4.3}$$

Therefore, the time difference distribution associated with the decay of the $(3/2^-_1)$ state of interest can be modeled with a response function defined by the convolution of a prompt Gaussian response function and an exponential decay of the 156-keV state.

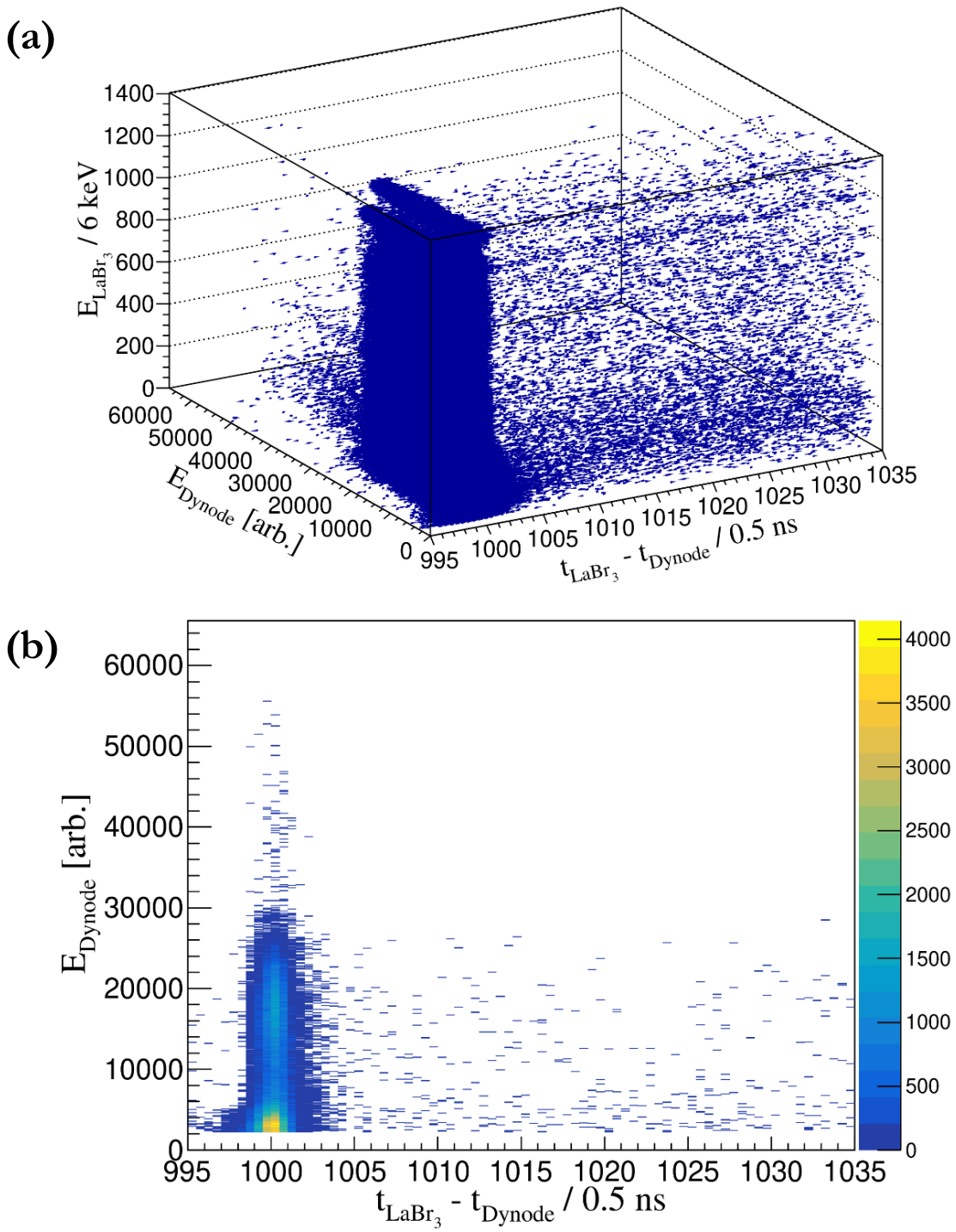

Figure 4.10: **(a)** 3D spectrum of energy deposition in the $LaBr_3$(Ce) and $CeBr_3$ implantation detectors plotted against the time difference between the $LaBr_3$(Ce) and the dynode using a ^{60}Co source. **(b)** 2D projection of the 156-keV photopeak onto the dynode energy and time difference axes.

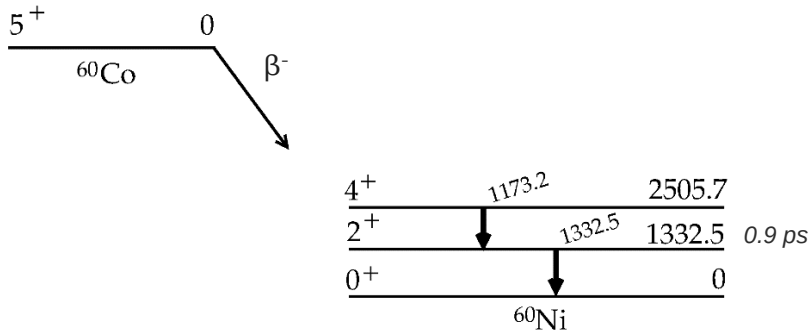

Figure 4.11: ^{60}Ni level scheme following the β^- decay of ^{60}Co adapted from Ref. [2]

Consideration: Implicit dependence of the time response width, σ, on E_γ and E_D

It must be emphasized that the goal to measure the half-lives of isomeric states in this work using the β-γ timing method involves calculating time differences for events where a β-decay electron correlated to the specific ion of interest was detected in the $CeBr_3$ implantation detector and the γ ray of interest was detected in one of the $LaBr_3$(Ce) detectors. Characterizing the prompt component of the resulting convolution involves isolating events corresponding to the detection of radiation in the $CeBr_3$ implantation detector associated with the detection of the 156-keV γ ray in one of the $LaBr_3$(Ce) detectors.

The prompt time response characterization and the relationship between the time response width, σ, and E_γ and E_D can be effectively demonstrated using a 3D histogram. This histogram captures the time difference between the dynode and $LaBr_3$(Ce) detectors, the energy deposition in the $LaBr_3$(Ce) detectors, and the energy deposition in the $CeBr_3$ implantation detectors. An example of such a histogram, obtained from a ^{60}Co source, is shown in Figure 4.10(a). The use of a ^{60}Co source is relevant for characterizing the prompt time response because the 2^+ state at 1332.5

keV in ^{60}Ni, which is populated following the β^- decay of ^{60}Co, undergoes de-excitation to the 0^+ ground state by emitting a 1332.5-keV γ ray with a half-life of 0.9 ps, as depicted in Figure 4.11.

The 0.9-ps half-life is below the sensitivity of the fast-timing measurement setup used in this experiment, resulting in prompt distributions for the time differences across the dynode and $LaBr_3$(Ce) energy distributions. The ^{60}Co source measurement was utilized to characterize the prompt distribution in the 156-keV energy region. A 2D projection of the $LaBr_3$(Ce) energy region associated with the 156-keV γ ray was created on the dynode energy and time difference axes, employing the same graphical cut as shown in Figure 4.9(a).

The sensitivity of the prompt time response width to the dynode energy, E_D distribution which is implicitly dependent on the γ-ray energy of interest, E_γ, can be observed in Figure 4.10(b). It is worth mentioning that the full E_D distribution is not captured in Figure 4.10(b) due to the energy range limitation of the intense 1173.2- and 1332.5-keV γ rays emitted following the decay of the ^{60}Co source. Nonetheless, characterizing the prompt response using the photopeaks, Compton distribution, and back-scatter peaks resulting from their interactions with detector materials is sufficient for the analysis.

A comprehensive method to account for the sensitivity of σ on E_D (and E_γ) in reality involves discretizing the E_D distribution, allowing for the extraction of σ values from 1D projections of each discrete bin on the time difference axis. These σ values were obtained from Gaussian fits to the prompt time difference distributions. The truncated E_D distribution due to the ^{60}Co energy range calls for an extrapolation of σ values for regions in the distribution not accounted for. The distribution of σ values as a function of E_D, shown in Figure 4.12, was fit using a power law function, and used for extrapolation.

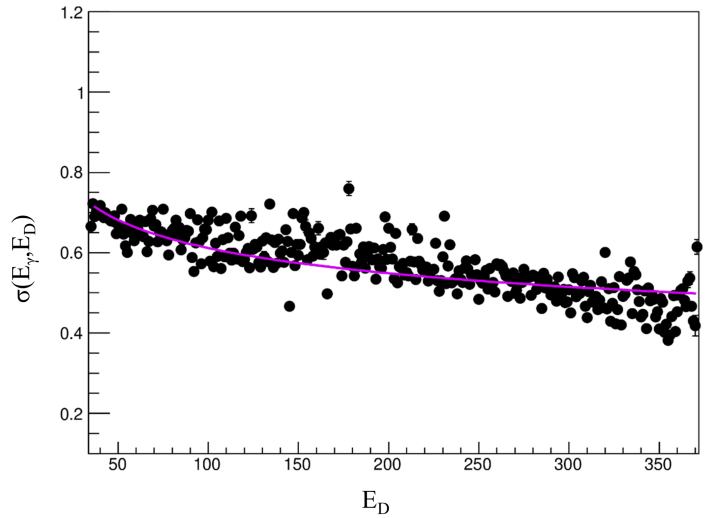

Figure 4.12: $\sigma(E_\gamma, E_D)$ values over a discretized dynode energy, E_D distribution using a ^{60}Co source. A power law fit (violet) was used to extrapolate σ values for higher-energy bins.

Accurately measuring the half-life therefore involves fitting the time difference distribution shown in Figure 4.9 such that the prompt response is defined by σ, fixed at individual values extracted from the step described in the preceding paragraph. The full time difference distribution due to the 156-keV γ-ray transition was then modeled by a response function consisting of a linear combination of the individual convolutions of prompt Gaussian functions with an exponential decay, added to a nearby background distribution, $B(t)$, histogrammed and scaled by the number of counts in the $LaBr_3$(Ce) energy region associated with the 156-keV γ-ray transition.

Mathematically, the response function can be written as

$$R(t, t_0, \sigma, \tau) = C_{E_D E_\gamma} \left[\Sigma_{E_D=E_0}^{E_F} \left[\exp\left[-\frac{1}{2} \left(\frac{(t-t_0)}{\sigma(E_\gamma, E_D)} \right)^2 \right] \otimes \exp\left[-\frac{(t-t_0)}{\tau} \right] \right] + sB(t) \right] \quad (4.4)$$

where $C_{E_D E_\gamma}$ is the number of counts in $LaBr_3$(Ce) energy region associated with the 156-keV γ-ray transition, and $\Sigma_{E_D=E_0}^{E_F}$ represents the sum over the discretized dynode energy distribution, E_D. The background time difference distribution, $B(t)$, is approximated by the distribution above

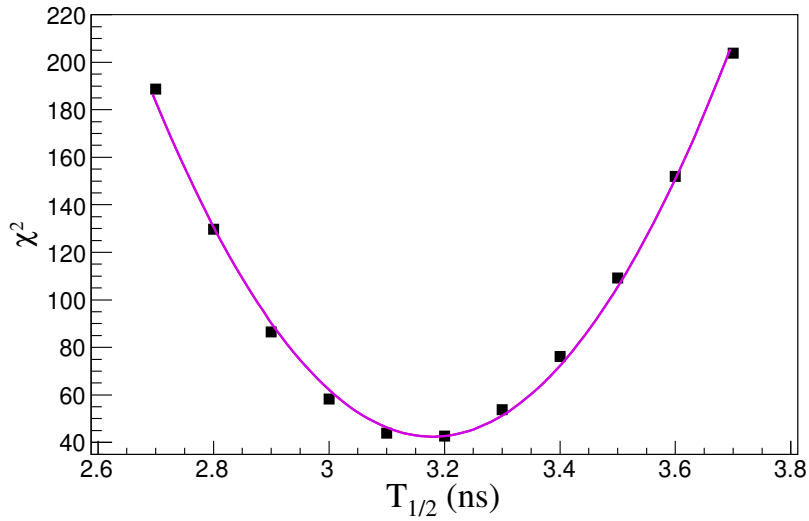

Figure 4.13: χ^2 values for eleven time response functions defined in Eq. 4.4, generated with fixed $T_{1/2}$ values distributed about the minimum. The distribution of $T_{1/2}$ values was fit with a second-order polynomial function (violet) such that the $T_{1/2}$ value corresponding to the best fit was defined by the minimum of the distribution. The statistical uncertainty at 1σ from the minimum was found to be 0.04 ns.

the peak of interest, using a gate size that matches the one used for defining the peak region. It is scaled by a factor, s, which is close to one. It should be noted that the energy dependence of the centroid, t_0 was also investigated and found to be inconsequential in modeling the prompt timing response.

To create the most accurate response function that effectively characterizes the time difference distribution associated with the 156-keV γ-ray transition, eleven distinct functions were generated as described above, each varying in terms of their fixed τ values, defined by the half-lives. These response functions were then compared with the experimental data, and χ^2 values were calculated for each response function as shown in Figure 4.13. The distribution of these χ^2 values was fitted using a second-order polynomial function, and the half-life corresponding to the minimum χ^2 value ($\chi^2 min$) was determined. This value was used to generate the best time response function or

total fit as shown in Figure 4.14. The statistical uncertainty associated with measuring the half-life was extracted using the χ^2_{min} + 1 graphical method of assigning confidence intervals [60].

The half-life of the $(3/2^-_1)$ state at 156 keV in ^{37}Si was determined to be 3.20(4) ns, with a corresponding statistical uncertainty at 1σ. This value is in agreement with the previously measured half-life of 3.0(7) ns [67], and it represents a significant reduction in the statistical uncertainty by a factor of ∼18. The successful reproduction of the half-life of the 156-keV state serves as a validation of the measurement technique employed for this dataset.

4.4 First half-life measurement of the $(7/2^-_1)$ state in ^{37}Si using the β-γ fast-timing method

Building upon the successful validation of the technique discussed in Section 4.3, the same methodology was applied to extract the half-life of the $(7/2^-_1)$ state. This was made possible by the observation of a corresponding 68-keV ground-state transition attributed to ^{37}Si following the $\beta^- n$ decay of implanted ^{38}Al ions, as discussed in Section 4.2. This case involved calculating the time difference between the detection of a β-decay electron in the $CeBr_3$ implantation detector (start time) and the detection of the 68-keV γ ray in one of the surrounding $LaBr_3$(Ce) detectors (stop time), as illustrated in Figure 4.15(a) and (b).

In a similar fashion as in Section 4.3, the half-life of the $(7/2^-_1)$ state in ^{37}Si at 68 keV and its associated statistical uncertainty at 1σ was measured as 9.1(7) ns, corresponding to the minimum of the second-order polynomial fit on the χ^2 distribution shown in Figure 4.16. The measured half-life represents the most accurate response function used to describe the time difference distribution due to the half-life of the $(7/2^-_1)$ state as shown in Figure 4.17.

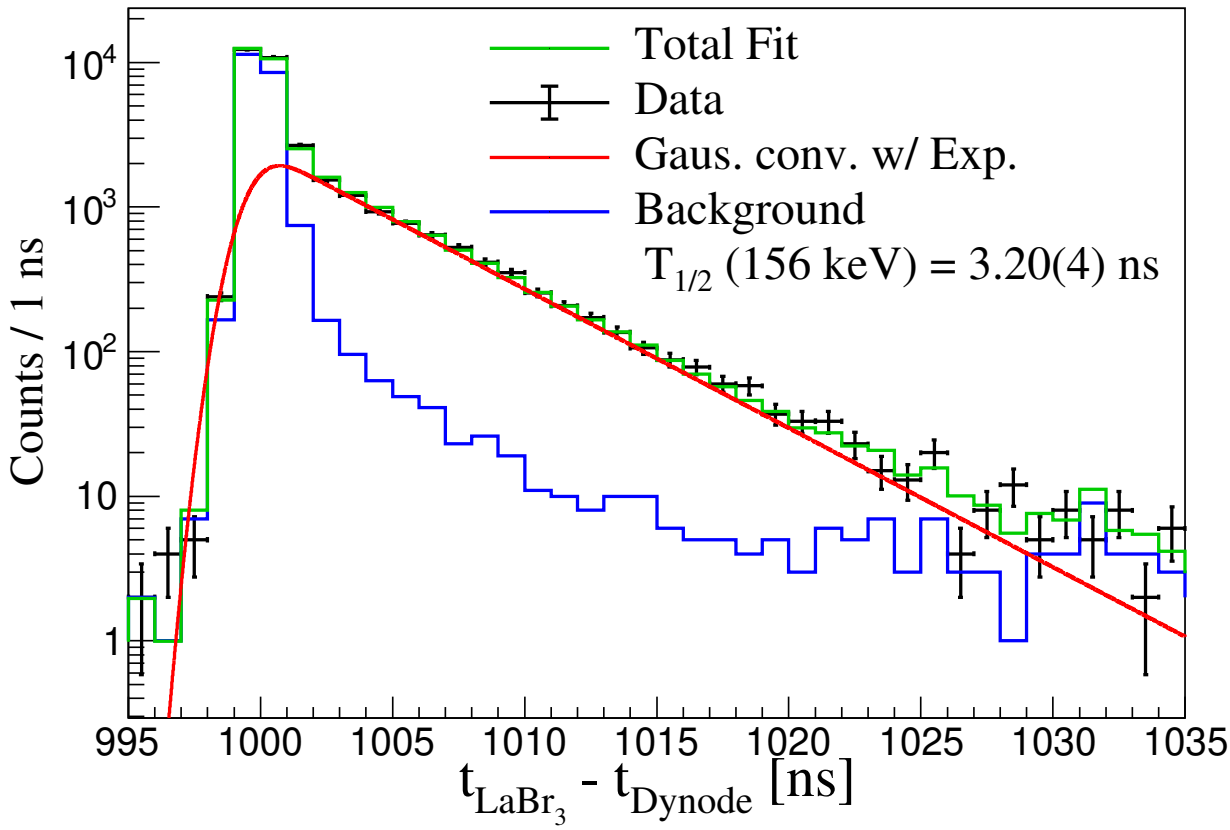

Figure 4.14: Time difference distribution due to the half-life of the $(3/2^-_1)$ state in ^{37}Si (black), following ^{37}Al β decay. The best fit corresponding to a half-life of 3.20(4) ns shown in green is a linear combination of multiple convolutions (red) and a background region taken above the 156-keV transition (blue), scaled to the number of counts in the $LaBr_3$(Ce) energy region associated with the 156-keV γ-ray transition.

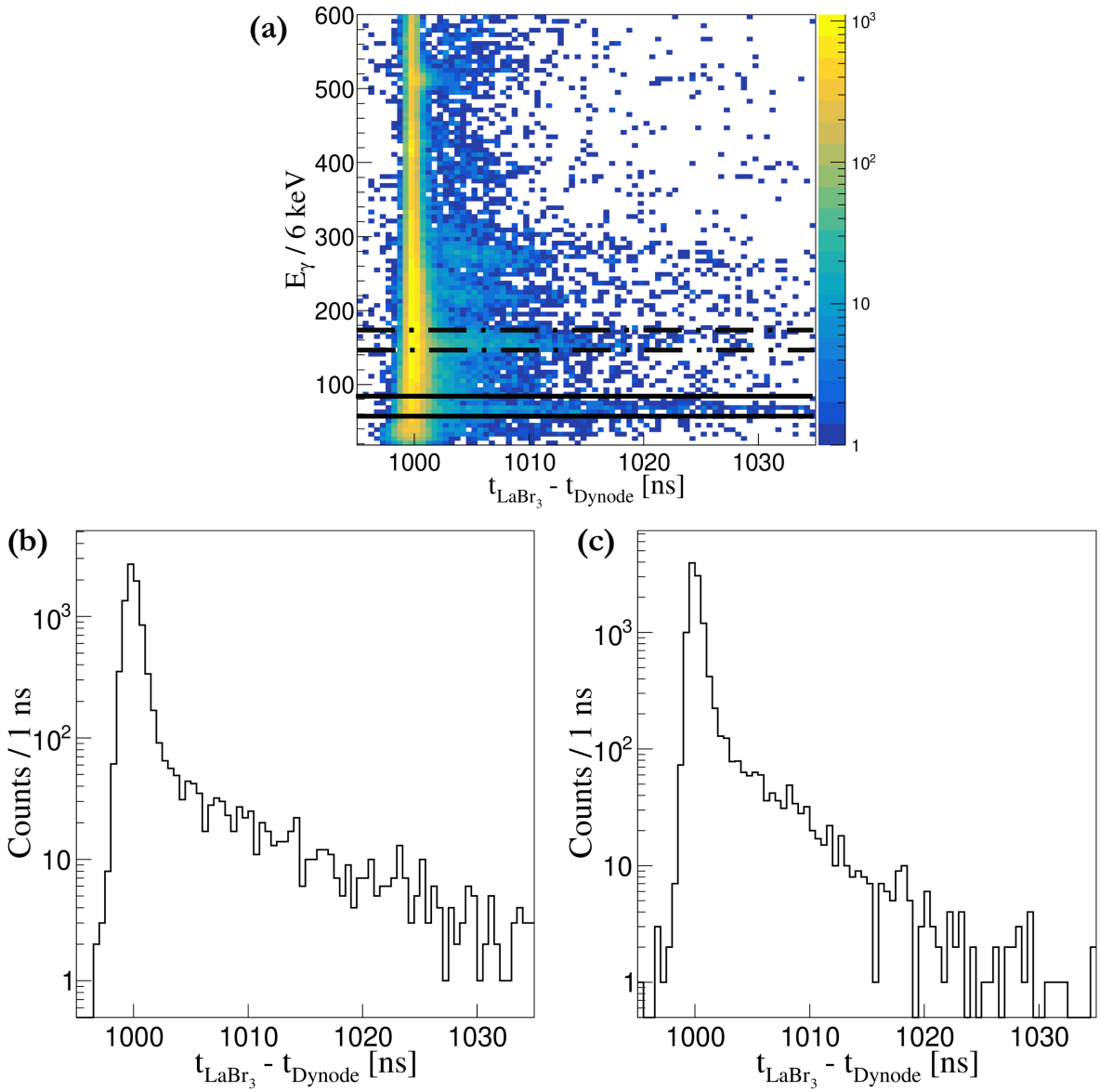

Figure 4.15: **(a)** 2D plot of β-delayed γ-rays detected in the $LaBr_3$(Ce) detectors within 27 ms of ^{38}Al ion implantation versus time difference between the $LaBr_3$(Ce) detectors and PSPMT dynode. **Bottom panel**: 1D projection of the 68-keV photopeak (graphical cut bordered by solid lines, **(b)**) and 156-keV photopeak (graphical cut bordered by dashed lines, **(c)**) on the time difference axis.

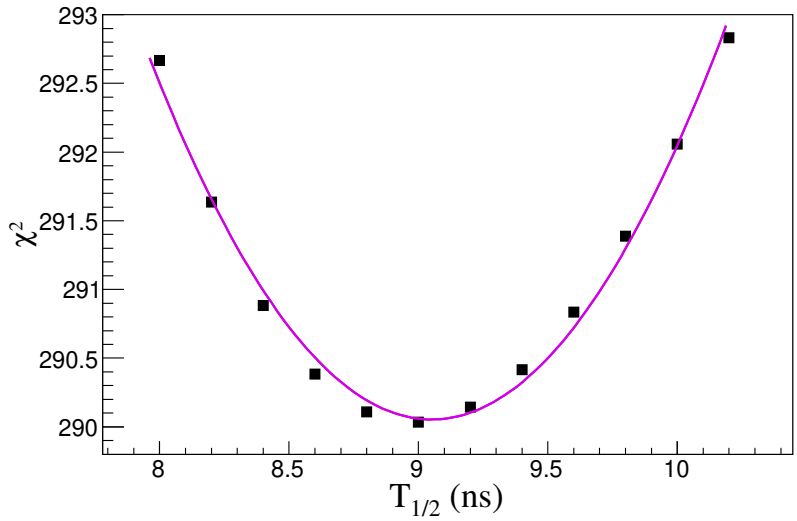

Figure 4.16: χ^2 values for twelve time response functions defined in Eq. 4.4, generated with fixed $T_{1/2}$ values to measure the half-life of the 68-keV state.

4.5 Half-life measurement of the $(3/2^-_1)$ state following ^{38}Al $\beta^- n$ decay using the β-γ fast-timing method

It is interesting to consider the measurement of the half-life of the $(3/2^-_1)$ state in ^{37}Si at 156 keV following the $\beta^- n$ decay of implanted ^{38}Al ions. This is due to the observation of a 156-keV photopeak in the γ-ray spectrum correlated to ^{38}Al, alongside the 68-keV transition attributed to ^{37}Si as discussed in Section 4.2. This is also evident in the 2D $LaBr_3$(Ce) energy versus time difference spectrum and the 1D projection along the 156-keV photopeak on the time difference axis shown in Figure 4.15(a) and (c), respectively. The measurement technique outlined in Section 4.3 can also be utilized to determine the half-life of the $(3/2^-_1)$ state by fitting the time difference distribution associated its decay, as shown by the best-fit in Figure 4.18.

The measured half-life of the 156-keV state, determined as 3.1(2) ns following the $\beta^- n$ decay of ^{38}Al ions, is in agreement with the measurement of 3.20(4) ns obtained from the β decay of ^{37}Al. Given the improved statistical data, it is not surprising to observe a five-fold reduction in

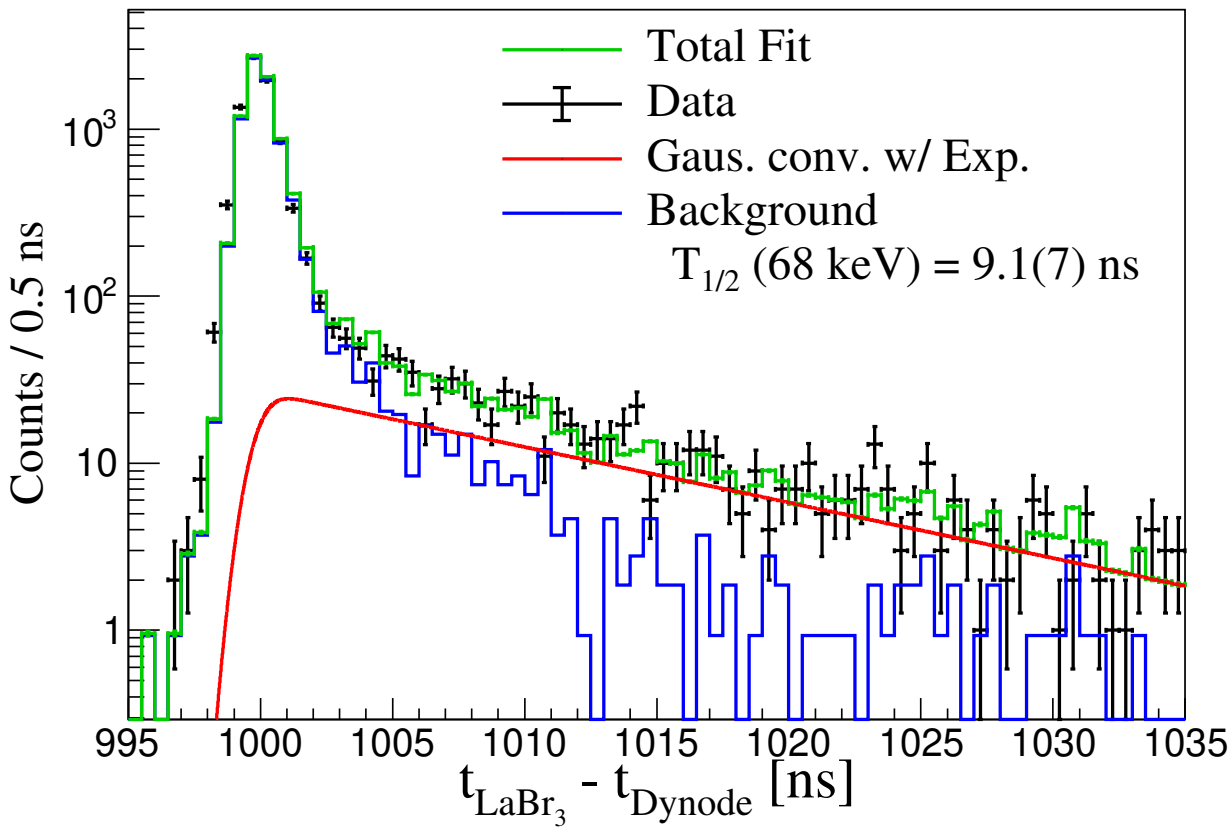

Figure 4.17: Time difference distribution due to the half-life of the $(7/2^-)$ isomeric state in ^{37}Si (black, shown in Figure 4.15)(b)), following ^{38}Al $\beta^- n$ decay. The best fit corresponding to a half-life of 9.1(7) ns shown in green is a linear combination of multiple convolutions (red) and a background region above the 68-keV transition (blue), scaled to the number of counts in the $LaBr_3$(Ce) energy region associated with the 68-keV γ-ray transition.

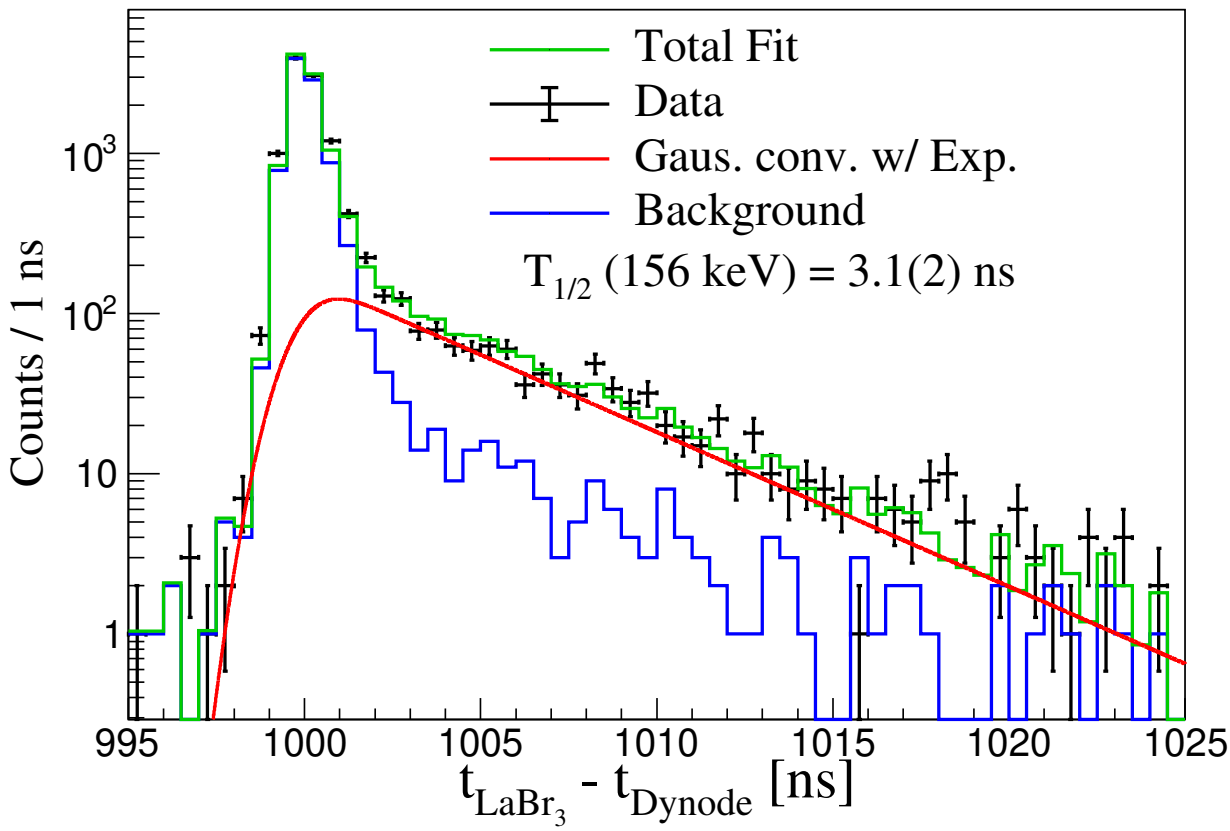

Figure 4.18: Time difference distribution due to the half-life of the $(3/2^-)$ state in ^{37}Si (black), following ^{38}Al $\beta^- n$ decay. The best fit corresponding to a half-life of 3.1(2) ns shown in green is a linear combination of multiple convolutions (red) and a background region above the 156-keV transition (blue), scaled to the number of counts in the $LaBr_3$(Ce) energy region associated with the 156-keV γ-ray transition.

the statistical uncertainties associated with the half-life measurement following ^{37}Al decay. The limited statistics informed the fit range shown in Figure 4.18.

4.6 Half-life measurement of the $(3/2^-_1)$ state following ^{37}Al decay using β-γ-γ timing method

The β-γ-γ timing method offers an alternative approach to the standard β-γ timing method, particularly when studying long-lived states in a cascade of γ rays [36, 35]. This method involves incorporating an additional set of γ-ray detectors capable of identifying and gating on a specific γ ray that feeds into the isomeric state of interest. For E16032, the experimental setup at the end station includes a separate γ-ray detection array — the SeGA array — which allows for the implementation of the β-γ-γ timing method. This method enables the isolation of the time difference distribution associated with the isomeric state of interest in the $LaBr_3$(Ce) energy versus $LaBr_3$(Ce) − PSPMT dynode time difference spectrum after gating on a coincident transition in SeGA.

The $(3/2)^-$ state at 156 keV is associated with two γ-ray cascades in ^{37}Si. It is fed by two specific γ rays, namely 1115 keV and 562 keV. These γ rays originate from the de-excitation of the $(5/2)^+$ state at 1270 keV and the $(3/2)^+$ state at 717 keV, respectively[2]. The half-life of the $(3/2)^-$ state at 156 keV was determined using the β-γ-γ timing method by calculating the time difference between events where a β-decay electron correlated with a ^{37}Al ion was detected in the $CeBr_3$ implantation detector, a 562-keV γ-ray transition was recorded in one of the SeGA detectors, and a 156-keV γ ray was detected in one of the adjacent $LaBr_3$(Ce) detectors.

Analogous to Figure 4.9(a) and Figure 4.15(a), the two-dimensional spectrum in Figure 4.19(a) exclusively displays the time difference distribution associated with the 156-keV isomeric state

[2]The relatively more intense 562-keV γ-ray transition was used as a gate for this measurement.

of interest. The selectivity of γ-γ coincidence measurements involved in the application of the β-γ-γ timing method ensures reliable half-life measurements through slope fitting alone, as time difference distributions originating from background radiation or random correlations are largely absent. This is shown in Figure 4.19(b) where the delayed time difference distribution attributed to the 156-keV gate is characterized by an exponential function. By employing this method, the half-life of the $(3/2)^-$ state at 156 keV was determined to be 3.22(1) ns. This measurement closely reproduces the meticulously determined half-life of 3.20(4) ns previously reported in Section 4.3.

The application of the β-γ-γ timing method for measuring half-lives of isomeric states is subject to certain limitations arising from statistics, detection efficiencies, and the relevant population modes. One significant limitation is the requirement for sufficiently intense transitions that can serve as γ-ray gates in the SeGA detectors, for example. These transitions must be intense enough such that coincident γ rays of interest in the $LaBr_3$(Ce) detectors can be observed after gating on them. Additionally, the $LaBr_3$(Ce) detectors themselves must possess reasonable detection efficiency at the relevant energies of the γ rays under investigation.

When considering the limitations imposed by the mode of population, it is important to note that isomeric states in a daughter nucleus may not participate in a γ-ray cascade but can be directly populated through the β decay of the parent nucleus. This situation is demonstrated in the measurement of the half-lives of the $(7/2)^-$ state at 68 keV and the $(3/2)^-$ state at 156 keV in ^{37}Si following the $\beta^- n$ decay of ^{38}Al, as discussed in Sections 4.4 and 4.5.

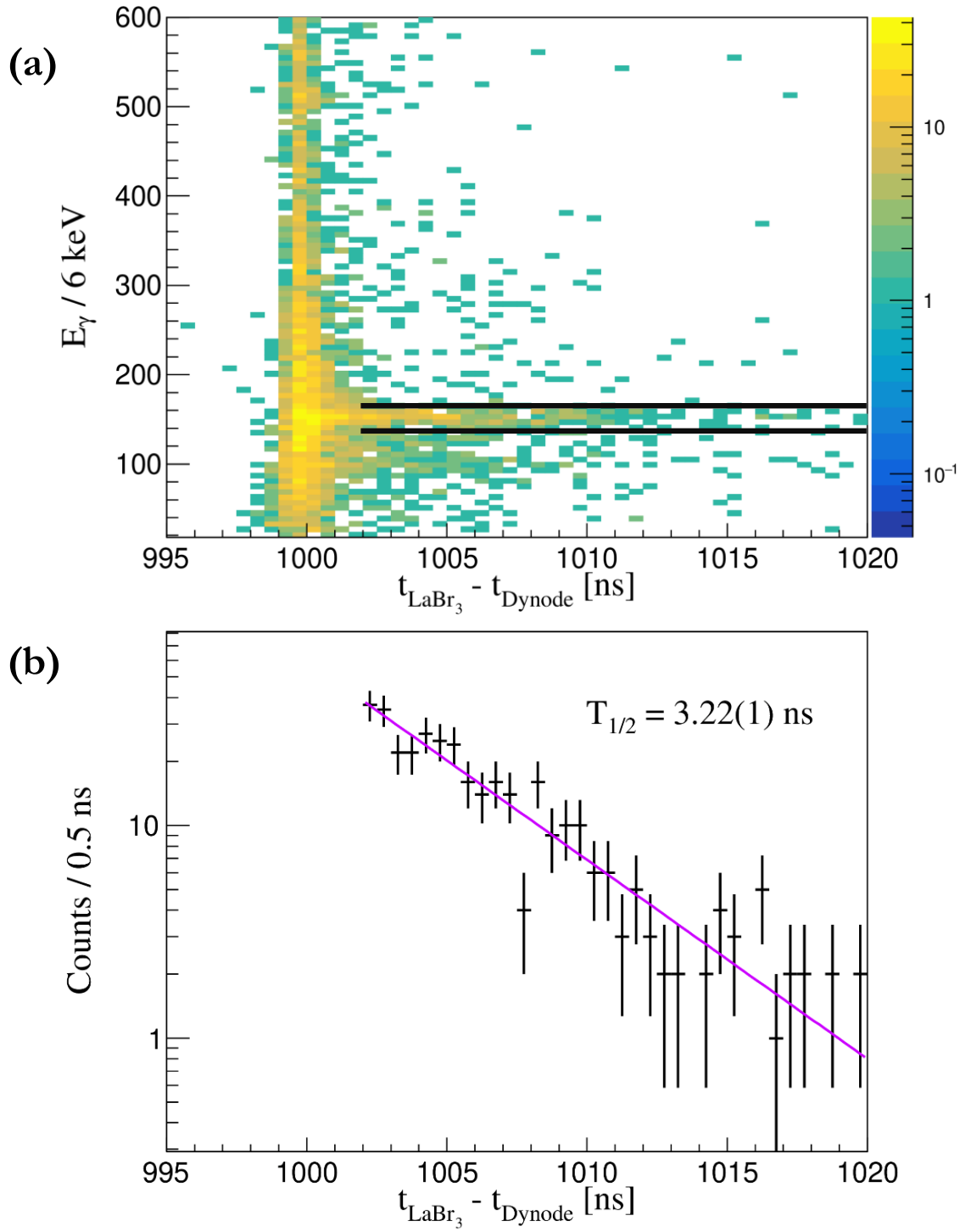

Figure 4.19: **(a)** 2D plot of β-delayed γ-rays detected in the $LaBr_3$(Ce) array within 33.9 ms of ^{37}Al implantation versus time difference between the $LaBr_3$(Ce) and PSPMT dynode. The distribution was gated on the 562-keV γ ray in SeGA. **(b)** 1D projection of the 156-keV photopeak (graphical cut bordered by solid lines in (a)) on the time difference axis. The half-life is obtained from the exponential fit in violet.

4.7 Discussion: Theoretical comparisons and shell structure implications of half-life measurements

An important aspect of nuclear structure studies is in the comparison between experimental measurements and theoretical predictions of observables used to characterize nuclei in a bid to improve theoretical models. Such comparisons are particularly important for exotic nuclei that lie far away from stability, where changes in shell structure challenge theoretical shell model predictions made. Prior to this work, the low-lying excited $(7/2^-_1)$ and $(3/2^-_1)$ states in ^{37}Si have been characterized using their excitation energies, as well as their tentative spins and parities. The half-life and reduced transition probability of the $(3/2^-_1)$ state was previously reported in Ref. [66]. The new half-life measurement of the $(7/2^-_1)$ state provides additional context to its characterization, and confirms its isomerism as predicted with theoretical calculations [67].

4.7.1 Selective calculation of states in ^{37}Si

The experimental level scheme of ^{37}Si is shown in Figure 4.20 using information from this work as well as Refs. [4, 65]. It is compared to predictions from shell model calculations using the SDPF-MU [72], SDPF-U-SI [44] and FSU [34] Hamiltonians up to the one-neutron separation energy of 2.21(13) MeV [74]. The SDPF-MU and SDPF-U-SI calculations were performed using NUSHELLX[8] while the FSU calculations were performed using CoSMo [73]. The measured half-lives are included to the right of the experimental level scheme in italics while tentative experimental spin-parity assignments taken from Refs.[4, 65] are included to the left of the level scheme. The relative intensities for transitions observed following the β decay of ^{37}Al are included above the transition energies.

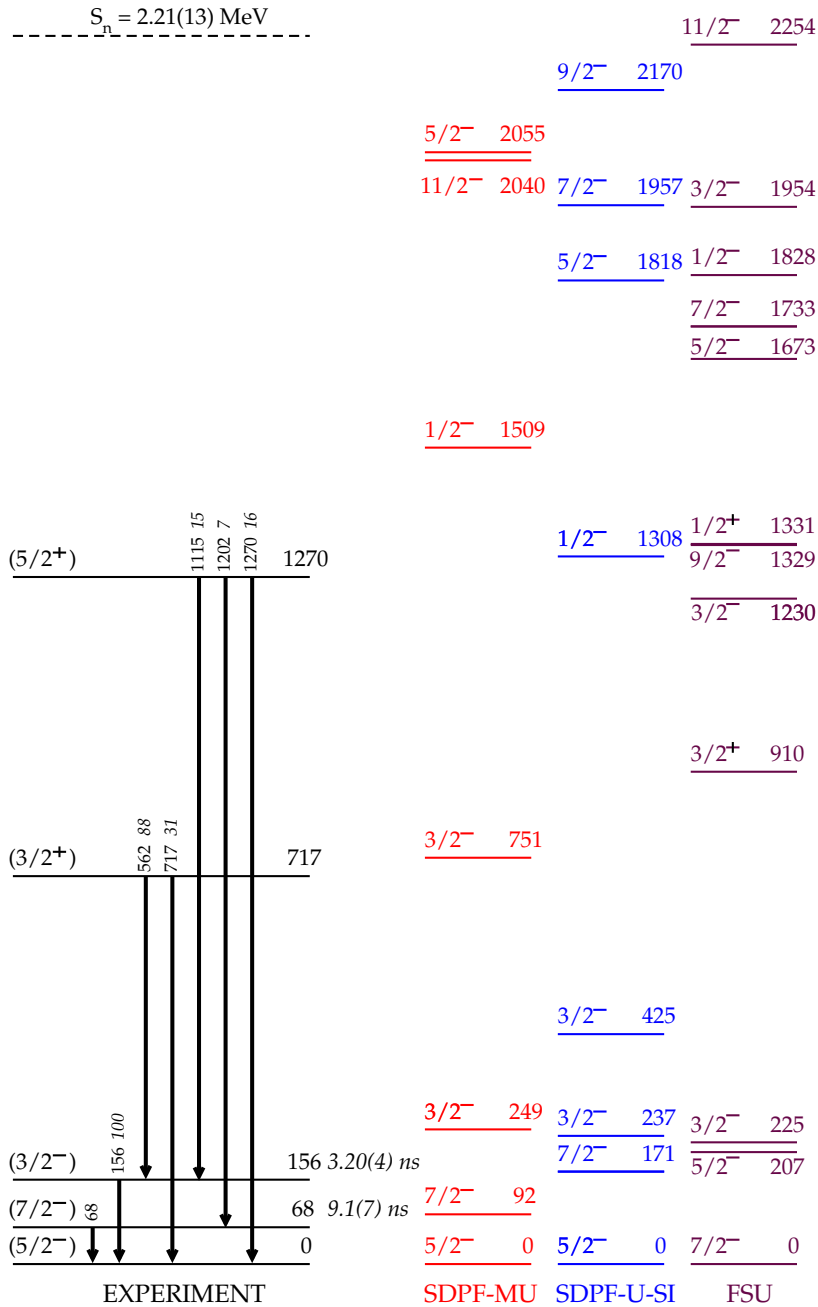

Figure 4.20: Comparison of the ^{37}Si experimental level scheme (black) to theoretical schemes predicted by shell model calculations using the SDPF-MU (red), SDPF-U-SI (blue) and FSU (maroon) interactions up to the S_n of ^{37}Si. (See text for additional information.)

The SDPF-MU Hamiltonian [72] was constructed to explain shape transitions in neutron-rich Si and S isotopes, such that its valence space includes the protons in the sd shell and the neutrons in the pf shell. Monopole interactions within the sd and pf shells were based on SDPF-M, while all other interactions within both shells were built on existing USD [8] interactions. The cross-shell part of the Hamiltonian is beyond the scope of this dissertation as protons (neutrons) were restricted to the sd (pf) shells. The SDPF-U-SI is one of the versions of the SDPF-U[44] interaction tuned for $Z > 14$ and $N = 20 - 40$. The USD interaction is used for protons in the sd shell while a variant of the KB3[54] interaction was used for neutrons in the pf shell. The cross-shell part of the Hamiltonian is also beyond the scope of this dissertation, similar to the SDPF-MU Hamiltonian. The FSU Hamiltonian is a modification of the WBP [75] interaction with a model space that treats protons and neutrons equivalently. The model space is made of the p shell, the full sd shell, and the lower mass region of the fp shell for both proton and neutrons.

For the SDPF-MU and SDPF-U-SI calculations, protons were restricted to the sd shell, and neutrons to the fp shell, such that no particle-hole excitations were allowed across the $N = 20$ shell gap. This resulted in the calculations of only negative-parity states in ^{37}Si, as shown in Figure 4.20. On the other hand, positive-parity states were calculated with the FSU Hamiltonian by allowing $1p1h$ excitations from the sd to fp shell. All three shell model calculations successfully reproduced the energy levels, especially those of the low-lying excited states, in good agreement with experimental measurements.

4.7.2 Reduced transition probabilities

Table 4.3 provides a comparison of the measured $B(M1)$ values to those obtained in the shell model calculations. The measured half-lives of the $(7/2^-_1)$ and $(3/2^-_1)$ states are also provided in

Table 4.3: Half-lives and reduced ground-state transition probabilities from the $(7/2^-_1)$ and $(3/2^-_1)$ states in ^{37}Si.

			$B(M1)$		
Transition	E_γ (keV)	Exp. $T_{1/2}$ (ns)	Exp. (μ_N^2)	SDPF-MU (μ_N^2)	SDPF-U-SI (μ_N^2)
$(7/2^-_1) \rightarrow (5/2^-_{g.s.})$	67.9(2)	9.1(7)	0.0137(11)	0.0369	0.0007
$(3/2^-_1) \rightarrow (5/2^-_{g.s.})$	155.8(2)	3.20(4)	0.00325(4)	0.0178	0.0005

its third column. The comparison reveals that the experimental and theoretical $B(M1)$ values for both transitions are in agreement, with the experimental results falling between the predictions of the SDPF-MU and SDPF-U-SI models.

Consideration: Mixing of the lowest allowed multipoles of electric and magnetic transitions

The lowest allowed multipoles of the electric and magnetic transitions associated with the $(7/2^-_1) \rightarrow (5/2^-_{g.s.})$ and $(3/2^-_1) \rightarrow (5/2^-_{g.s.})$ decays in ^{37}Si are $M1$ and $E2$. The theoretical $B(M1)$ values presented in Table 4.3 are based on the assumption of pure $M1$ decay for these transitions, as it is uncommon for low-energy transitions to exhibit significant $E2/M1$ mixing [7]. This is further suggested by the mixing ratios and branching factors calculated for both transitions, as extracted from the theoretical results provided in Table 4.4.

From the SDPF-MU calculation, the branching factor of an $M1$ decay from the $(7/2^-_1)$ state to the $(5/2^-)$ ground state will result in a partial half-life of 1.367 ns, compared to the $\sim$ 1 μs half-life due to $E2$ decay. The half-life on the ns scale due to an $M1$ decay is consistent with the experimental half-life of the $(7/2^-_1)$ state shown in the third column of Table 4.3, suggesting that a pure $M1$ assumption is reasonable. The same logic can be used to explain the $M1$ decay being dominant for the $(3/2^-_1)$ state to the $(5/2^-)$ ground state transition using the SDPF-MU shell model calculation, as well as both transitions using the SDPF-U-SI calculation. Therefore, a pure $M1$

Table 4.4: Mixing ratios (δ) and branching fractions (b) associated with the $(7/2^-_1) \rightarrow (5/2^-_{g.s.})$ and $(3/2^-_1) \rightarrow (5/2^-_{g.s.})$ transitions in ^{37}Si using SDPF-MU and SDPF-U-SI shell model calculations. $B(M1)$ and $B(E2)$ values are shown in units of μ_N^2 and e^2fm^4, respectively. Branching factors were calculated using Eqs. 2.23 and 2.24.

Interaction	Transition	$T_{1/2}$ (ns)	δ	$B(M1)$	$b(M1)$	$B(E2)$	$b(E2)$
SDPF-MU	$(7/2^-_1) \rightarrow (5/2^-_{g.s.})$	1.367	-0.03	0.0369	0.9991	46.69	0.0008992
	$(3/2^-_1) \rightarrow (5/2^-_{g.s.})$	0.141	-0.09	0.0178	0.9920	33.33	0.008035
SDPF-U-SI	$(7/2^-_1) \rightarrow (5/2^-_{g.s.})$	9.450	-0.37	0.0007	0.8796	49.94	0.1204
	$(3/2^-_1) \rightarrow (5/2^-_{g.s.})$	4.058	0.71	0.0005	0.6649	61.91	0.3352

decay was assumed for both transitions given theoretical expectations of small $E2/M1$ mixing, and as such, the experimental $B(M1)$ values are considered as upper limits.

Consideration: Experiment versus theory comparisons

A closer look at Table 4.3 reveals that the experimentally measured $B(M1; (7/2^-_1) \rightarrow (5/2^-_{g.s.}))$ is in better agreement with the SDPF-MU shell model calculation, which over-predicts the value by a factor of ∼3. On the other hand, the SDPF-U-SI calculation under-predicts the $B(M1)$ value by a factor of ∼20. In contrast, both the SDPF-MU and SDPF-U-SI calculations exhibit similar deviations from experimental $B(M1; (3/2^-_1) \rightarrow (5/2^-_{g.s.}))$ values. Specifically, the SDPF-MU calculation over-predicts the $B(M1; (3/2^-_1) \rightarrow (5/2^-_{g.s.}))$ value by a factor of ∼6, while the SDPF-U-SI calculation under-predicts it by a similar factor of 6.

Further investigation of these results in light of a survey of similar experiment versus theory comparisons for low-lying excited to ground-state $M1$ transitions is presented in Appendix C, drawing from findings in Ref. [59]. Such comparisons were made for ground-state $M1$ transition matrix elements evaluated for sd-shell nuclei between $A = 16$ and $A = 40$. As discussed in Appendix C, the experimental $B(M1)$ values were converted into $M(M1)$ values and compared to

theoretical predictions. The experimental and theoretical results were found to be in agreement, taking into account the relatively small magnitudes of the values being compared as discussed in Ref. [59].

4.7.3 Tentative spin assignments and half-life measurements

The spins and parities of interest in ^{37}Si remain tentative as shown in Figure 4.20. Theoretical expectations suggest that the ground and first-excited states of ^{37}Si can have either a spin-parity of $7/2^-$ or $5/2^-$. Particularly, the FSU shell model predicts a $7/2^-$ ground state and $5/2^-$ first-excited state in ^{37}Si, different from the SDPF-MU and SDPF-U-SI predictions. A flipped ordering of spins and parities is worth considering, although this may well be as a result of the states lying very closely within a theoretical energy uncertainty of 150 keV [59]. Assuming the ordering of states as presented in the FSU level scheme, a $(3/2^-_1) \rightarrow (7/2^-_{g.s.})$ decay would most likely be an $E2$ transition with a calculated half-life on the order of 2 ms, which is not representative of the experimentally measured half-life of 3.20(4) ns, and can be ruled out. Although a $(5/2^-_1) \rightarrow (7/2^-_{g.s.})$ transition will remain dominated by $M1$ decay, the previous argument in the preceding sentence on the $(3/2^-_1) \rightarrow (7/2^-_{g.s.})$ decay oppose a $(7/2^-)$ ground state spin-parity assignment in ^{37}Si.

4.7.4 Structure of low-lying isomeric states in ^{37}Si

The structure of the $(7/2^-_1)$ and $(3/2^-_1)$ isomeric states in ^{37}Si can be compared to each other. Table 4.5 contains the fp-shell neutron occupation numbers calculated for both isomeric states and the ground state in ^{37}Si using the SDPF-MU and SDPF-U-SI interactions. Both calculations predict the $(5/2^-_{g.s.})$ and $(7/2^-_1)$ states to be dominated by the $(\nu f_{7/2})^3$ configuration. The $(3/2^-_1)$ state is predicted to have a mixing of the $(\nu f_{7/2})^3$ and $(\nu f_{7/2})^2 \otimes (\nu p_{3/2})^1$ configurations which is a

Table 4.5: Neutron occupation numbers calculated for the $5/2^-_{g.s.}$, $7/2^-_1$ and $3/2^-_1$ states in the fp-shell.

Interaction	J^π	$0f_{7/2}$	$0f_{5/2}$	$1p_{3/2}$	$1p_{1/2}$
SDPF-MU	$5/2^-_{g.s}$	2.63	0.14	0.21	0.02
	$7/2^-_1$	2.68	0.12	0.18	0.02
	$3/2^-_1$	2.30	0.08	0.58	0.05
SDPF-U-SI	$5/2^-_{g.s}$	2.61	0.08	0.28	0.03
	$7/2^-_1$	2.73	0.10	0.14	0.02
	$3/2^-_1$	2.16	0.06	0.74	0.04

result of the state being formed by particle excitation across the $N = 28$ shell gap from the $\nu f_{7/2}$ into the $\nu p_{3/2}$ orbital.

CHAPTER V

RESULTS: HALF-LIFE INVESTIGATIONS OF ISOMERIC 0_2^+ STATES IN ^{34}SI AND ^{32}MG ACCESSED VIA BETA DECAY

5.1 The 0_2^+ state in ^{34}Si

The presence of the 0_2^+ state in ^{34}Si offers valuable insights into the interplay between normal and intruder configurations, as well as the phenomenon of shape coexistence in nuclei neighboring the $N = 20$ "island of inversion" [25]. This is particularly interesting as ^{34}Si is known to lie at the edge [6] of the "island of inversion" due to its ground state having a normal closed-shell configuration, and its lowest-excited states, including the 0_2^+ and 2_1^+ states having deformed configurations. This is different from neighbouring even-even nuclei in the region, like ^{32}Mg, whose ground and excited-state configurations are flipped.

The 0_2^+ state in ^{34}Si was first predicted to lie above the 2_1^+ state [6]. This was later refuted [24] and subsequently found to lie below the 2_1^+ state, such that it is located between the 2_1^+ and 0_1^+ states [26, 19, 50, 9]. An experimental investigation of the 0_2^+ state in ^{34}Si was first reported in the β-decay spectroscopy of ^{34}Al [46].

The 0_2^+ state in ^{34}Si was established at 2719(3) keV following its investigation in the β decay of ^{34}Al using electron spectroscopy coupled to β-decay spectroscopy, due to the expected $E0$ decay from the 0_2^+ state to the 0_1^+ state through internal pair formation, with the assumption that the 0_2^+ lies below the 2_1^+ state [61]. The half-life of the 0_2^+ state was measured as 19.4(7) ns, resulting

in the extraction of the electric monopole strength $\rho^2(E0 : 0_2^+ \rightarrow 0_1^+)$ of $13.0(9) \times 10^{-3}$, which is important for probing shape coexistence in nuclei and dependent on the half-life measurement. Furthermore, the existence of two β-decaying states in ^{34}Al — the 4^- ground state and an excited 1^+ state — was proven [61], with the 0_2^+ state preferentially fed in the decay of the 1^+ isomer.

The structure of ^{34}Si was further investigated in Ref. [30] with states separately populated in the decay of ^{34}Al and ^{34}Mg. This follows the identification of the β-decaying $4^-_{g.s}$ and 1_1^+ states in ^{34}Al [31, 61, 30]. Comprehensive level schemes in ^{34}Si following the different population mechanisms were built, and the half-life of the 0_2^+ state was measured as 19.4(5) ns. A branching ratio $R(2_1^+ \rightarrow 0_1^+ \,/\, 2_1^+ \rightarrow 0_2^+)$ of 1779(182) was obtained; and reduced transition probability $B(E2; 2_1^+ \rightarrow 0_2^+) = 47(19)e^2fm^4$ was measured. Specifically, the $2_1^+ \rightarrow 0_1^+$ transition was observed in the β decay of the $4^-_{g.s.}$.

5.2 Double-pulse analysis and characterization of the 0_2^+ state in ^{34}Si

A key objective of the E16032 experiment was to study the properties of the 0_2^+ state in ^{34}Si, from measuring its half-life to identifying other transitions built on top of it. Although a comprehensive investigation of the structure of ^{34}Si is presented in Ref. [30], which was published after this analysis began on the E16032 dataset, the half-life measurement technique employed for this analysis remains interesting, particularly due to its enhanced selectivity as seen in coincident spectra, making for reduced statistical uncertainties. Details peculiar to the analysis are discussed below.

5.2.1 Signature of the $0_2^+ \rightarrow 0_1^+$ $E0$ transition

The 0_2^+ state in ^{34}Si de-excites to the 0_1^+ state via $E0$ decay, accompanied by the emission of mono-energetic electrons that relate to the energy difference of the two 0^+ states. The mono-energetic electrons due to $E0$ decay are detected within the volume of the $CeBr_3$ detector some characteristic amount of time after electrons due to the β decay of the relevant implanted parent nuclei are detected. Such events are referred to as double-pulse events, characterized by traces with two pulses representing each decay type, separated in time. It should be noted that electrons from other types of radiation are also detected by the $CeBr_3$. Additionally, the $CeBr_3$ implantation detector exhibits significant sensitivity to low-energy γ rays which may de-excite isomeric states. However, the discussions in this subsection are specifically limited to the detection of $E0$ electrons following the corresponding transition in ^{34}Si. Furthermore, it is worth noting that not all time separations between decay types will lead to two distinct peaks that can be accurately characterized in terms of their amplitudes and timestamps. This aspect is currently being investigated and it falls outside the scope of this dissertation.

As discussed in Section 3.2.2.1 of Chapter III, relevant traces were modeled using "good" double-pulse fit functions from which pulse characteristics including amplitudes (energies) and time stamps were extracted. "Good" double-pulse fits were defined using the condition

$$\frac{\chi^2_{single}}{\chi^2_{double}} > 10 \tag{5.1}$$

where χ^2_{single} and χ^2_{double} represent the χ^2 values of the fit distributions using the single- and double-pulse fit functions, respectively. These characteristics were used to further investigate the traces and extract additional information for such $E0$ transitions, like the $0_2^+ \rightarrow 0_1^+$ decay in ^{34}Si.

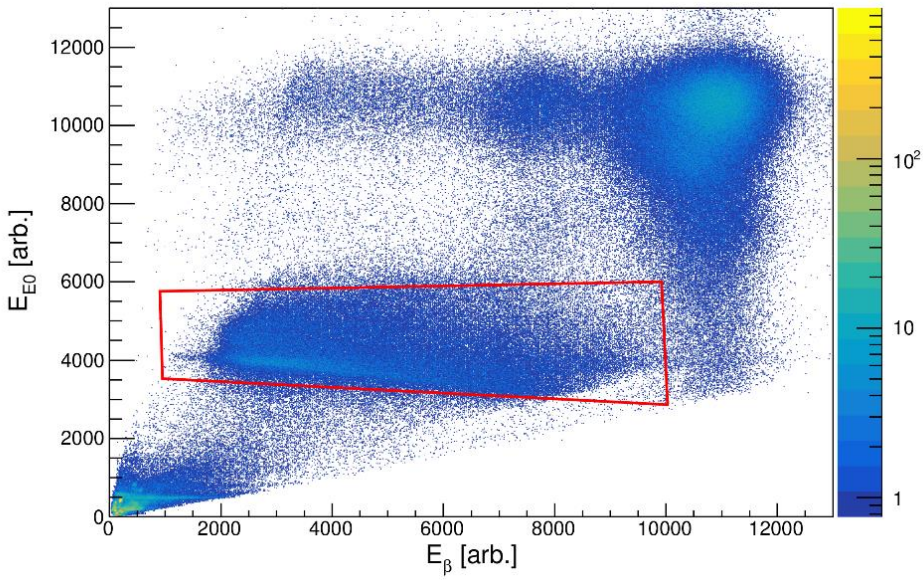

Figure 5.1: Distribution of pulse amplitudes extracted from "good" double-pulse fits, with the first due to β decay (E_β on the x-axis) plotted against the second pulse due to $E0$ transitions (E_{E0} on the y-axis.) The 2D graphical cut represents the $E0$ decay in ^{34}Si. (See text for additional information.)

The distribution of the energy of the $E0$ electrons (E_{E0}) as a function of the energy of the β-decay electrons (E_β)[1] is shown in Figure 5.1. These energies were obtained from parameters of "good" double-pulse fits. The mono-energetic nature of electrons emitted via $E0$ decay contrasted with the energies of electrons emitted via β decay result in an $E0$ decay signature such that a constant value of E_{E0} can be observed over a range of E_β values relevant to the decay of the parent isotope. These $E0$ decay signatures are, however, not distinct enough in Figure 5.1, as there appears to be smearing along the E_{E0} entries in the spectrum. It should be noted that the high-energy artifacts that persist for both pulses at the top-right portion of Figure 5.1 are atypical of β and $E0$ decays or fitting algorithm limitations, and are instead due to beam production, showing up at a frequency of ~250 MHz, as seen in Figure 5.2(a).

[1]The amplitudes of the first and second pulses in a "good" double-pulse trace are referred to as E_β and E_{E0}, respectively, for the sake of analysis discussed in this section.

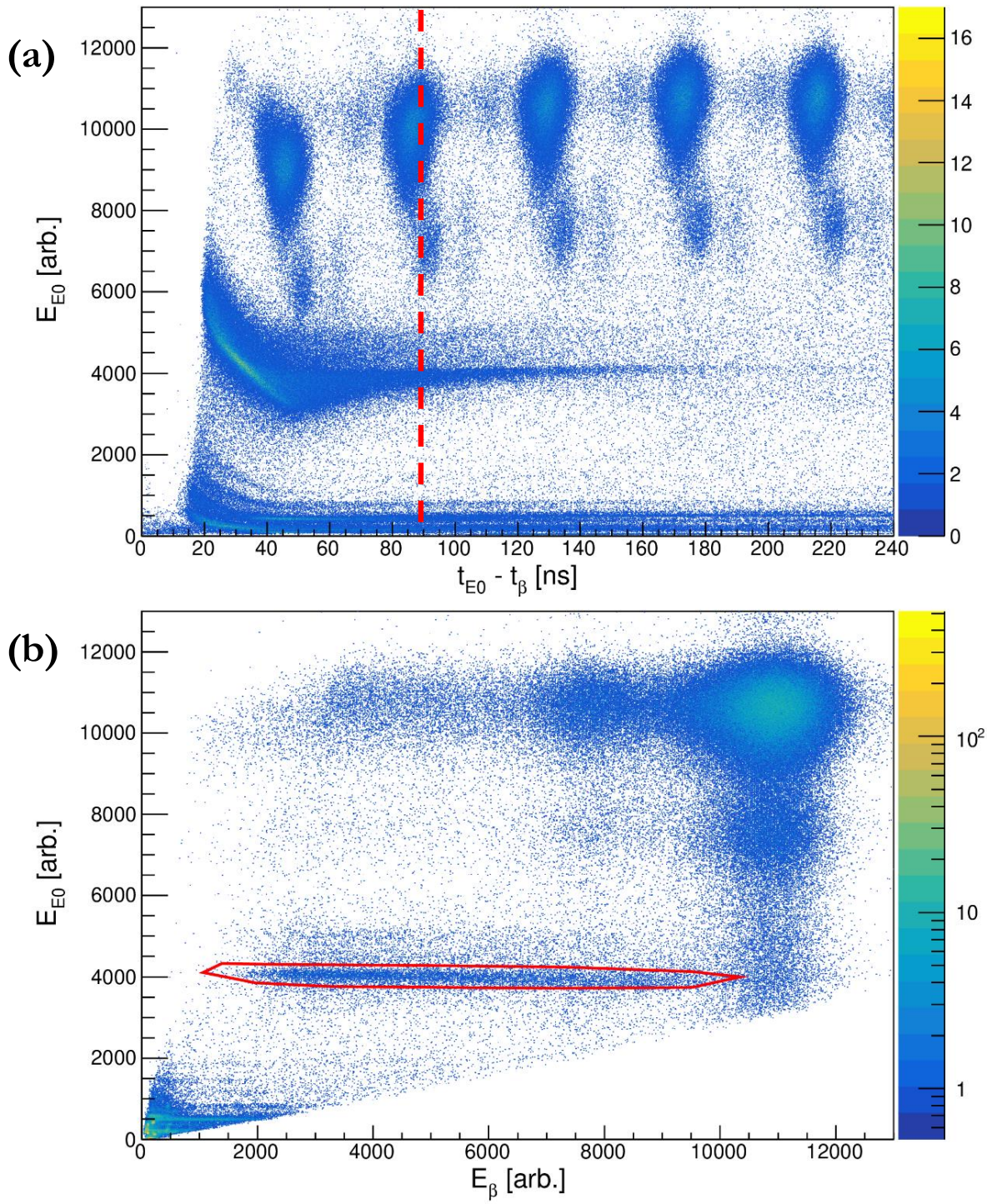

Figure 5.2: **(a)**: Dependence of $E0$ decay electron energies extracted from "*good*" double-pulse fits on the time difference between the β-decay and $E0$ electron timestamps. The dashed red line represents the time difference threshold applied for this analysis. **(b)**: E_{E0} versus E_β distribution gated on time difference cut. $0_2^+ \rightarrow 0_1^+$ decay in ^{34}Si is isolated using the 2D graphical cut in red.

The smearing of the $E0$ decay signatures, particularly the strongly populated $0_2^+ \rightarrow 0_1^+$ decay in ^{34}Si bordered by the 2D graphical cut in Figure 5.1 is not necessarily surprising. This is primarily due to limitations associated with the fitting procedure which sometimes fails to properly extract $E0$ electron amplitudes for double-pulse events not well-separated in time. To further explore this effect, the analysis focused on examining the performance of the fits in extracting the amplitudes of $E0$ decay electrons as a function of the time difference between the timestamps of the $E0$ and β-decay electron pulses. The results are illustrated in Figure 5.2(a). Well-pronounced smearing at small time difference values can be seen for the $E0$ decay signatures across the energy continuum, informing the application of a time difference threshold as an additional condition to populate the E_{E0} versus E_β distribution shown in Figure 5.2(b). It should be noted that various time difference thresholds were considered, but a balance between the clarity of the resulting spectrum shown in Figure 5.2(b) and amount of statistics had to be struck. The high-energy artifacts referenced in the previous paragraph can be identified in this spectrum as well, and are separated by ~40 ns.

5.2.2 Half-life Measurement of the 0_2^+ state

Figure 5.3 shows the time difference distribution corresponding to the detection of an $E0$ decay electron following the detection of a β-decay electron, with the 2D graphical cut in Figure 5.2(b) applied as a gate. A half-life of 20.5(3) ns was extracted from the exponential fit, in agreement with the 19.4(7) ns and 19.4(5) ns values reported in Ref. [61] and Ref. [30], respectively. The successful reproduction of the half-life provides validation for the double-pulse analysis technique established to measure the half-lives of excited isomeric states in this dataset.

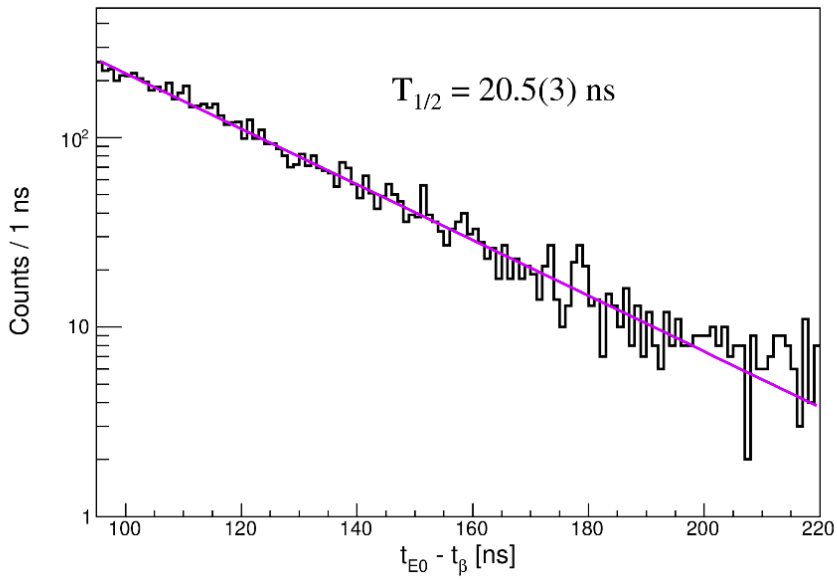

Figure 5.3: Exponential decay peculiar to the $0_2^+ \rightarrow 0_1^+$ decay in ^{34}Si (defined by the 2D graphical cut in Figure 5.2(b).) The half-life was extracted using the exponential fit (violet curve.)

5.2.3 Search for transitions built on top of the 0_2^+ state

The observation of the $2_1^+ \rightarrow 0_2^+$ and $2_1^+ \rightarrow 0_1^+$ transitions in ^{34}Si is necessary to extract the branching ratios from the decay of the 2_1^+ state as well as information about the mixing between the 0^+ states. A weak 607-keV γ-ray transition is expected to de-excite the 2_1^+ state at 3325 keV and feed the 0_2^+ state at 2718 keV. This transition was previously reported in Refs. [61, 30] in the decay of the $4^-_{g.s.}$ of ^{34}Al, while the 3325-keV $2_1^+ \rightarrow 0_1^+$ crossover transition was strongly observed in the decay of both β-decaying 1^+ and 4^- states in ^{34}Al [30].

The $0_2^+ \rightarrow 0_1^+$ $E0$ decay is strongly observed in the decay of the 1^+ isomer in ^{34}Al, which is preferentially populated in the decay of the $0^+_{g.s}$ of ^{34}Mg [30]. These observations are consistent in this analysis, given the implantation of ^{34}Mg ions labelled in Figure 3.7. The hinderance of the population of the $4^-_{g.s.}$ state in ^{34}Al by the $0^+_{g.s.}$ state of ^{34}Mg similarly informs the non-observation

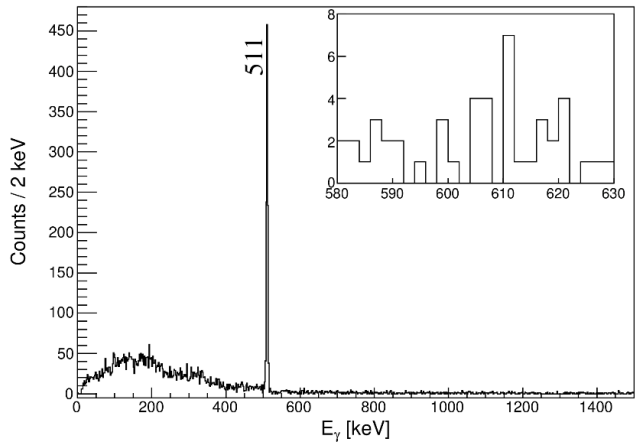

Figure 5.4: γ-ray spectrum in coincidence with the $0_2^+ \rightarrow 0_1^+$ $E0$ transition in ^{34}Si following β decay of the 1^+ isomeric state of ^{34}Al fed by ^{34}Mg β decay. ***Inset***: Energy region around the 607-keV γ-ray transition of interest.

of the 607-keV $2_1^+ \rightarrow 0_2^+$ γ-ray transition in coincidence with the $E0$ decay as shown in Figure 5.4. Infact, no other transitions except the very-intense 511-keV γ rays produced in the annihilation of electrons and positrons due to $E0$ decay via internal pair formation can be observed in the coincidence spectrum, indicating that the 0_2^+ state is strongly fed in the decay of the 1^+ isomer in ^{34}Al.

The presence of ^{34}Si was further investigated by generating a γ-ray spectrum correlated to ^{34}Mg implants as shown in Figure 5.5, using similar methods outlined in Section 4.1 of Chapter IV. Only the intense 1193- and 3325-keV transitions reported in Ref. [30] can be identified in the resulting spectrum, while the 607-keV $2_1^+ \rightarrow 0_2^+$ transition is unobserved.

5.3 Double-pulse analysis and opportunities for future work: Intense low-energy structures and identifying isomeric transitions

The signature of an $E0$ isomeric transition observed following β decay is discussed in Section 5.2 where the energy of the $E0$ electrons (second pulse) remains constant regardless of the energy

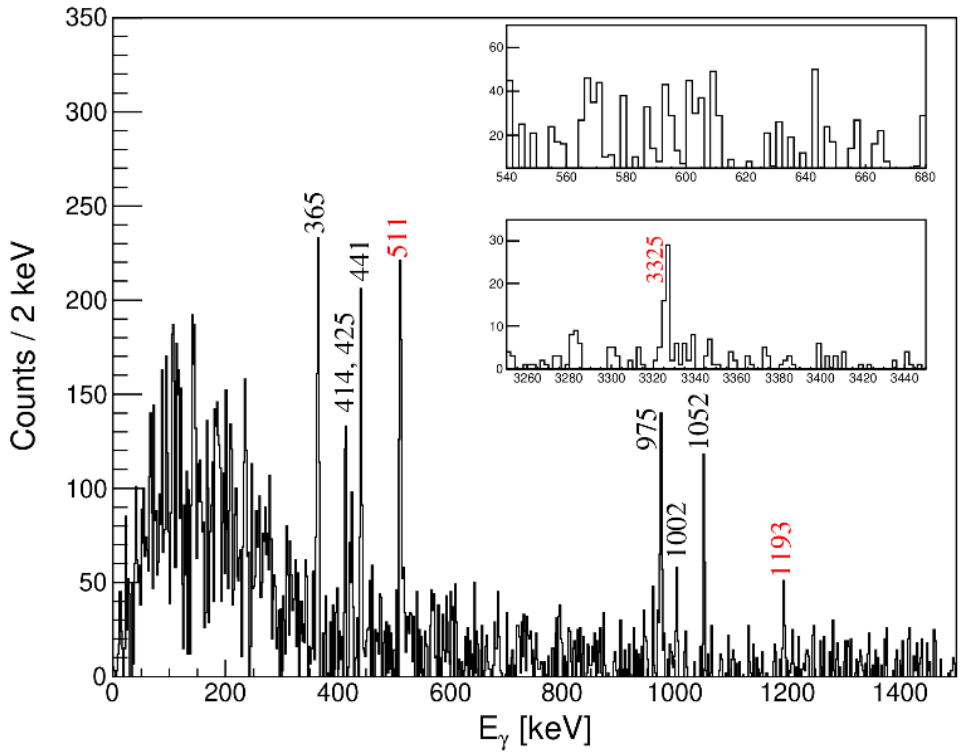

Figure 5.5: β-delayed γ ray spectrum for γ rays detected in the SeGA detectors within a correlation window of 45 ms which corresponds to one ^{34}Mg β-decay half-life. The most intense γ-ray transitions in the ^{34}Al daughter are labelled (black) as well as transitions in the ^{34}Si granddaughter (red). **Top inset**: Region around the 607-keV γ ray corresponding to the $2_1^+ \rightarrow 0_2^+$ transition. **Bottom inset**: Region around the 3325-keV γ ray corresponding to the $2_1^+ \rightarrow 0_2^+$ transition.

of the β-decay electrons (first pulse). By taking a closer look at the lower-energy distribution in Figure 5.2(b), other transition types detected by the $CeBr_3$ detector can be observed, most of which allow for characterization and extraction of measurable observables.

The distributions highlighted in Figure 5.6(a) and Figure 5.7(a) are two of the most-intense low-energy distributions in the double-pulse energy spectrum[2]. These distributions appear to correspond to two transitions characterized by individual mono-energetic pulses, which may indicate that both pulses recorded in the double-pulse trace originate from separate isomeric transitions. Valuable information can be extracted using the existing analytical capabilities, similar to the characterization of the distribution related to the isomeric transition involving the $0_2^+ \rightarrow 0_1^+$ $E0$ transition in ^{34}Si discussed, in Section 5.2.

Exponentially decaying time difference distributions between the two pulses in each distribution are shown in Figure 5.6(b) and Figure 5.7(b). The distributions were fit with an exponential function and the corresponding half-lives have been extracted. The γ-ray spectra in coincidence with both signatures are also included in Figure 5.6(c) and Figure 5.7(c).

Important information about half-lives, transition energies of isomeric states and coincident transitions can be extracted using the double-pulse analysis method. Although challenges in data analysis, including distinguishing between different types of radiation and the impact of statistical limitations persist, ongoing efforts to improve the analysis technique, like machine learning prove promising.

[2]It should be noted that the axes labels have been slightly modified as the radiation types discussed in this section are unknown.

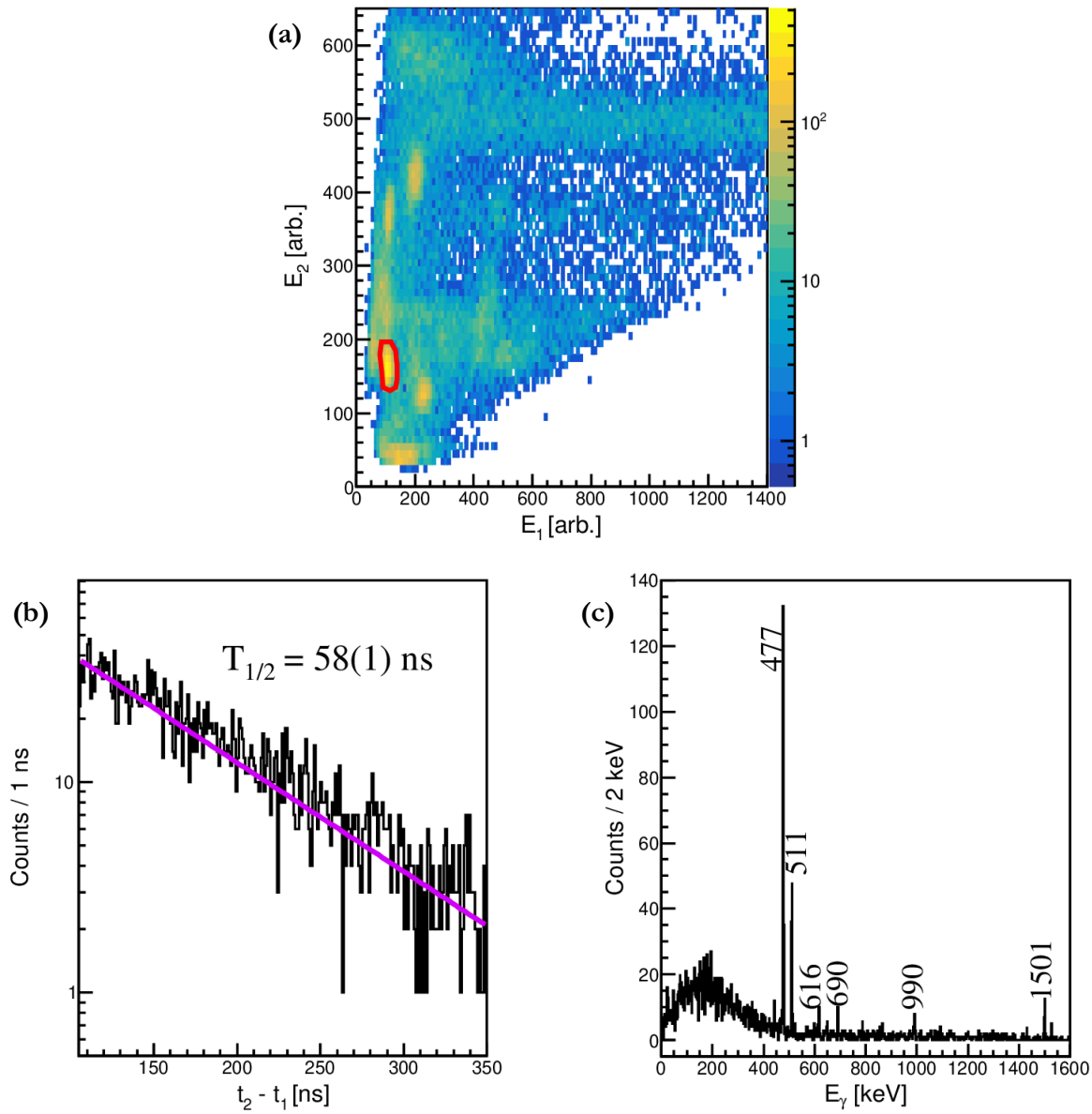

Figure 5.6: **Example 1**: Lower energy distribution of pulse amplitudes extracted from "good" double-pulse fits. **(a)**: 2D double-pulse distribution with graphical cut in red gated around structure representing two decay modes with mono-energetic characteristics. E_1 refers to the energy of the first peak, while E_2 represents the energy of the second peak in the corresponding double-pulse spectrum. **(b)**: Exponential decay curve peculiar to gated distribution, with a half-life extracted using the exponential fit in violet. **(c)**: γ-ray spectrum in coincidence with the gated distribution.

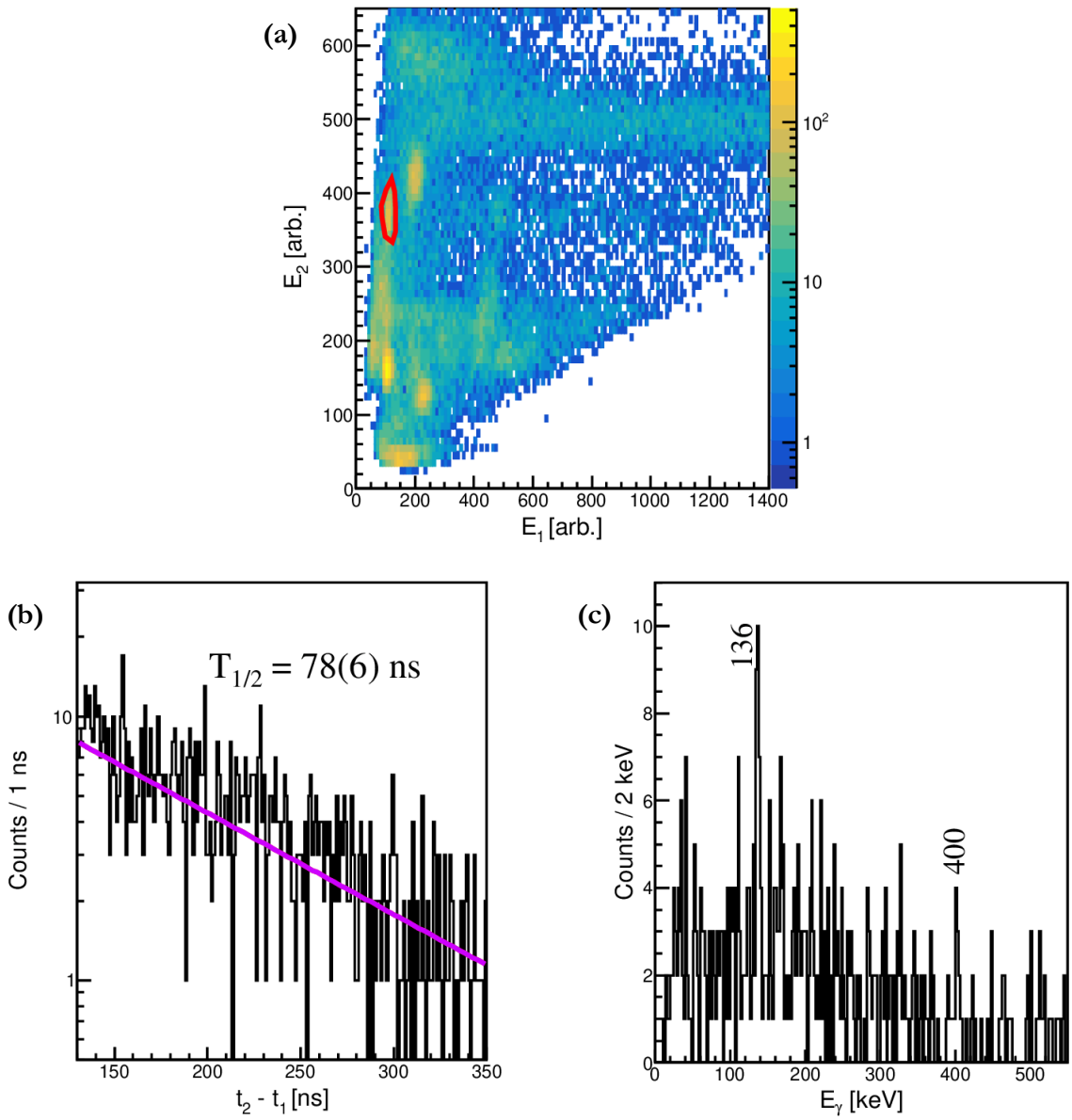

Figure 5.7: **Example 2**: Lower energy distribution of pulse amplitudes extracted from "good" double-pulse fits. **(a)**: 2D double-pulse distribution with graphical cut in red gated around structure representing two decay modes with mono-energetic characteristics. E_1 refers to the energy of the first peak, while E_2 represents the energy of the second peak in the corresponding double-pulse spectrum. **(b)**: Exponential decay curve peculiar to gated distribution, with a half-life extracted using the exponential fit in violet. **(c)**: γ-ray spectrum in coincidence with the gated distribution.

5.4 The 0_2^+ state in ^{32}Mg

^{32}Mg is known to be situated at the center of the $N = 20$ "island of inversion" [20] where excited states with intruder configuration become ground states, and the ground states with normal configuration become excited at low energies [25][3]. Characterizing low-lying 0^+ states as such is therefore a sensitive probe to understanding shell evolution in exotic nuclei, and as previously stated, can provide insights into the phenomena of shape coexistence and the mixing of intruder and normal configurations in these nuclei [9].

The 0_2^+ state in ^{32}Mg was first experimentally established at 1058(2) keV in a two neutron transfer reaction in inverse kinematics at REX-ISOLDE [76] based on comparisons of the outgoing proton angular distribution for the reaction populating the 0_2^+ state to optical model parameters for DWBA calculations. A 172(6)-keV γ-ray transition was observed in coincidence with the 885-keV $2_1^+ \rightarrow 0_1^+$ transition and attributed to the decay of the 0_2^+ state. A lower limit of 7 ns was placed on the half-life of the 0_2^+ due to the low intensity of the corresponding 172-keV $0_2^+ \rightarrow 2_1^+$ transition.

The 0_2^+ state was not directly observed until 2019, when it was investigated in Ref. [17] by identifying in-flight isomeric decays following its population in a ^{9}Be(^{34}Si, ^{32}Mgγ) reaction. The 2_1^+ state was verified at 885 keV, while the 0_2^+ was established at 1050 keV. The half-life of the 0_2^+ state was constrained to 7 ns $< T_{1/2} <$ 26 ns; as well as a reduced transition probability of 28 e^{2}fm^4 $< B(E2 : 2_1^+ \rightarrow 0_2^+) <$ 122 e^{2}fm^4 [17] using information from Ref. [76].

Experimental investigations into the structure of the 0_2^+ state in ^{32}Mg via β decay have not been previously reported. We sought to achieve this in experiment E16032, specifically in observing a corresponding $0_2^+ \rightarrow 2_1^+$ γ-ray transition and measuring its half-life following the $\beta^- n$ decay

[3] It is worth noting that a recent investigation into the structure of the 0_2^+ state in ^{32}Mg revealed that it is dominated by intruder configuration, pointing to a conclusion that an excited 0^+ state in ^{32}Mg with normal configuration has not been experimentally observed [17].

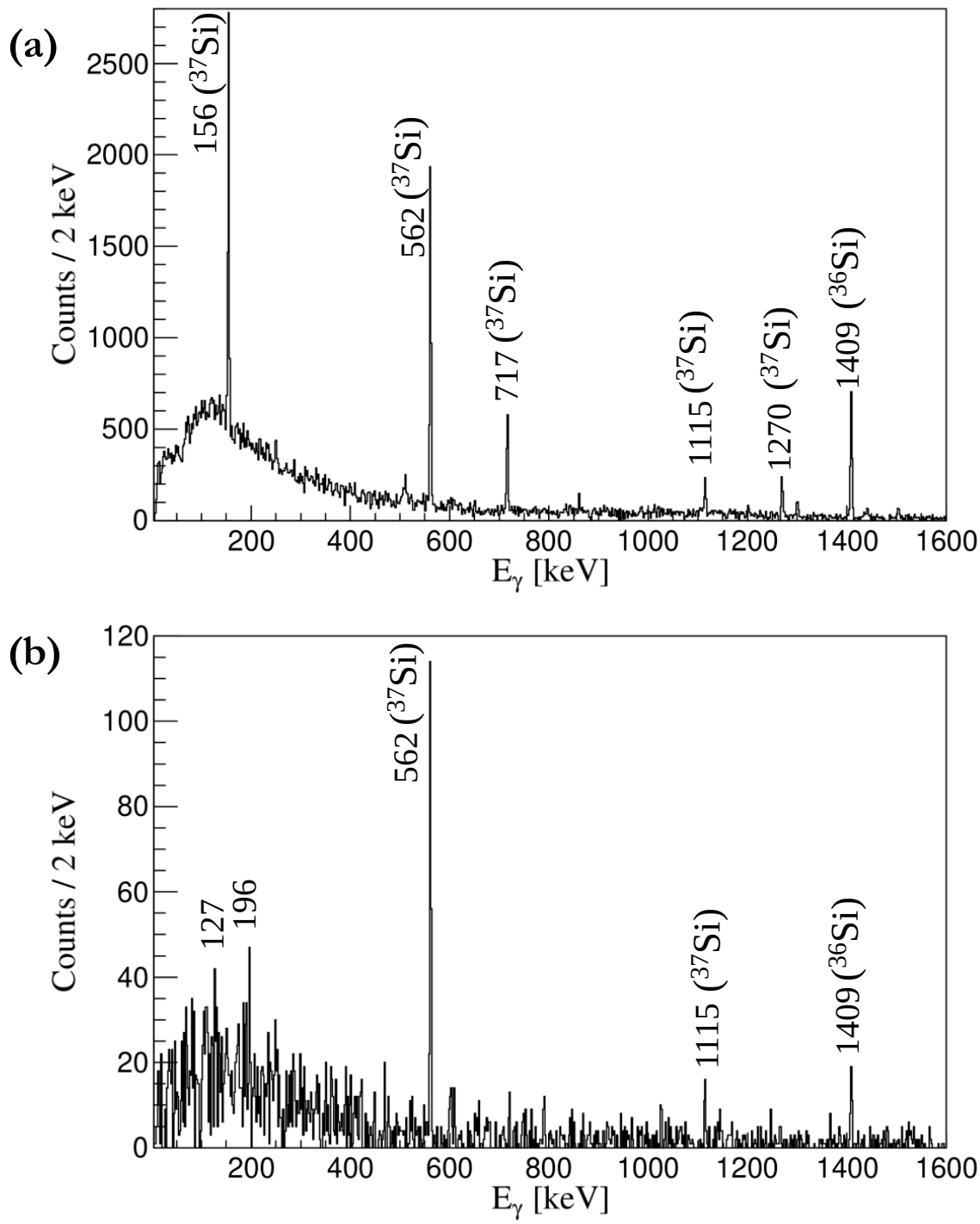

Figure 5.8: **(a)**: β-delayed γ-ray spectrum for γ rays detected in the SeGA detectors within a correlation window of 33.9 ms, corresponding to three ^{37}Al β-decay half-lives ($T_{1/2}$ = 11.3 ms). (γ rays at 156, 562 and 1115 keV associated with the $(3/2)^-$ state in ^{37}Si are of interest). **(b)**: γ ray spectrum in (a) filled with additional 3 ns < t_{LaBr_3} - $t_{PSPMT} \leq$ 20 ns condition.

of implanted ^{33}Na ions. Although the ~170-keV transition in ^{32}Mg was not observed in this experiment, the observation of the 885-keV $2^+_1 \rightarrow 0^+_{g.s}$ transition plays a key role in supporting the suggestion for identifying the isomeric 0^+_2 state using this technique.

5.5 β-γ-γ timing method and opportunities for future work: A case study to search for the isomeric 0^+_2 state in ^{32}Mg and identify coincident γ-ray transitions

The β-γ-γ timing method described in Section 4.6 of Chapter IV can be adapted to identify γ-ray transitions that directly feed an isomeric state, or are part of a γ-ray cascade involving the isomeric state. The technique can be validated by comparing the β-delayed γ-ray spectrum correlated to ^{37}Al shown in Figure 5.8(a) to a condensed version of the same spectrum where an additional condition of 3 ns < t_{LaBr_3} - $t_{PSPMT} \leq$ 20 ns was applied before filling the spectrum, as shown in Figure 5.8(b). This condition was set to isolate the presence of an isomer, which is expected to exhibit a delayed time difference distribution. The intense 562- and 115-keV γ rays, which are known to be in coincidence with the 156-keV γ ray that de-excites the isomeric $(3/2^-_1)$ state in ^{37}Si persist in the spectrum obtained with the additional timing condition. This observation provides further support for the presence of the isomeric state and its characteristic γ-ray transitions.

The observation of a ~170-keV γ ray in coincidence with the 885-keV $2^+_1 \rightarrow 0^+_1$ γ-ray transition served as experimental evidence of the presence of the 0^+_2 state in ^{32}Mg in Ref. [76]. Such γ ray was however unobserved in the β-delayed γ-ray spectrum correlated to implanted ^{33}Na ions as shown in Figure 5.9(a). The observation of the persisting 885-keV $2^+_1 \rightarrow 0^+_1$ transition in Figure 5.9(b) suggests that the cascade in ^{32}Mg, associated with the 885-keV γ ray, likely involved an isomer, probably the 0^+_2 state.

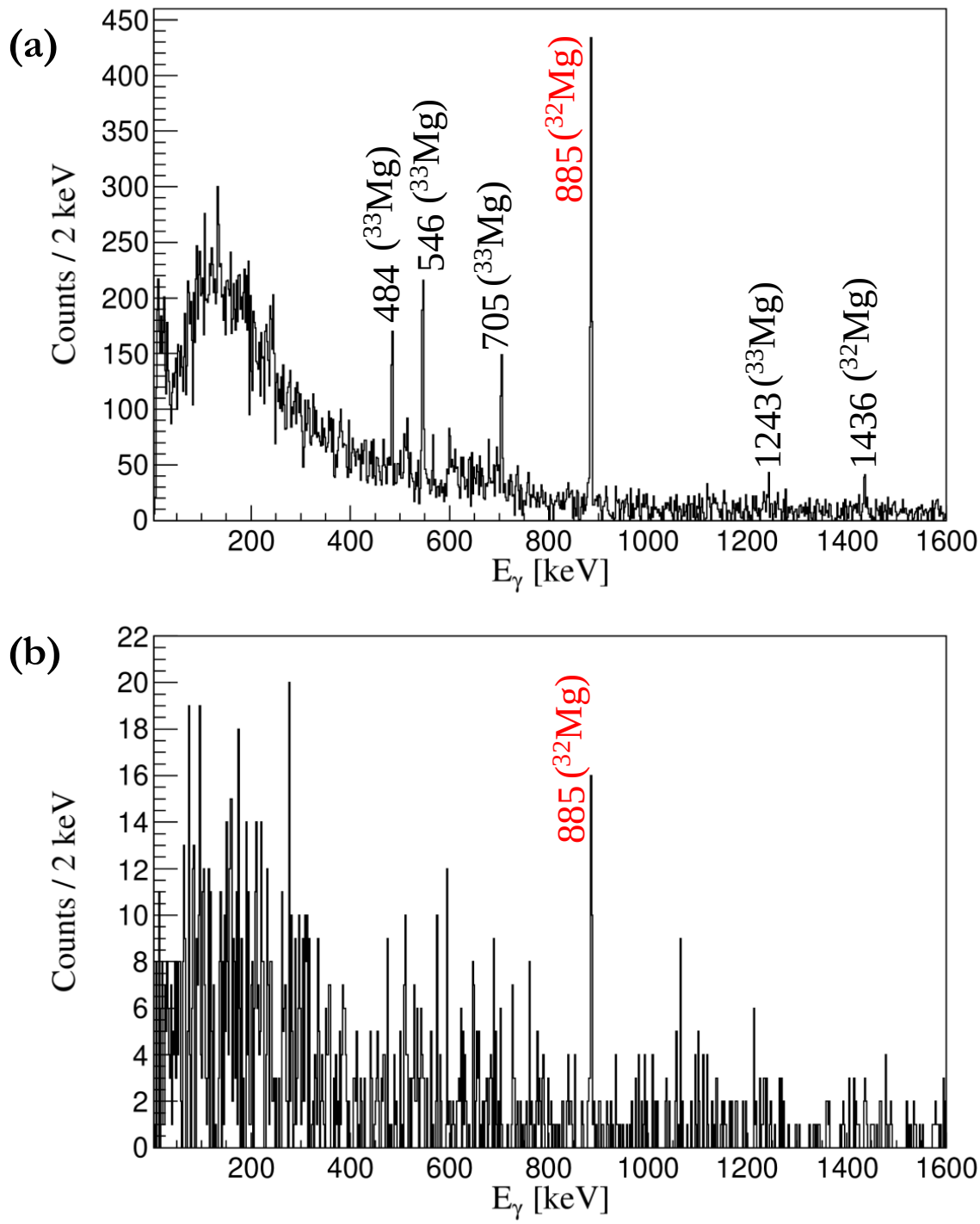

Figure 5.9: **(a)**: β-delayed γ-ray spectrum for γ rays detected in the SeGA detectors within a correlation window of 24 ms, corresponding to three ^{33}Na β-decay half-lives ($T_{1/2}$ = 8 ms). (The 885-keV γ ray that is in coincidence with the ~170-keV $0_2^+ \rightarrow 2_1^+$ transition is emphasized in red.) **(b)**: γ ray spectrum in (a) filled with additional 3 ns < t_{LaBr_3} - t_{PSPMT} ≤ 20 ns condition.

The association of the 885-keV γ-ray transition with the isomeric 0_2^+ state in ^{32}Mg can be further validated by investigating γ-ray spectra correlated to implanted ^{32}Na ions using a correlation window of three ^{32}Na β-decay half-lives (Figure 5.10(a)), and an additional 3 ns < t_{LaBr_3} - t_{PSPMT} $\leq$ 20 ns condition (Figure 5.10(b)). The observation of the 885-keV γ ray in Figure 5.10(a) proves consistent with the direct population of the 2_1^+ state in ^{32}Mg following the β decay of implanted ^{32}Na ions. Moreover, the non-observation of an 885-keV γ-ray in Figure 5.10(b) validates the attribution of the 0_2^+ state in ^{32}Mg following the $\beta^- n$ decay of ^{33}Na, indicating that the 885-keV transition will not be associated with an isomeric state following the decay of ^{32}Na, as reported in Refs. [71, 37].

The possibility of populating the 885-keV state in ^{32}Mg through the 0_2^+ isomeric state has been indirectly demonstrated. However, the absence of an observed ~170-keV γ-ray transition in the β-delayed γ-ray spectrum correlated to ^{33}Na limits the ability to make definitive conclusions. Despite this, the method described above opens up numerous possibilities for future investigations. It provides a means to identify unknown γ rays that could be associated with isomeric states populated in the β decay of implanted ions. It is important to note that this method is subject to statistical limitations, as discussed in Section 4.6 in Chapter IV.

The utilization of the $CeBr_3$ implantation detector in the E16032 experimental setup and its sensitivity to γ rays — particularly low-energy γ rays of interest associated with these isomeric states — proves reliable in extracting half-lives of the isomeric states that emit such γ rays, including the 68- and ~170-keV transitions attributed to ^{37}Si and ^{32}Mg, respectively, discussed in this chapter. The double-pulse method discussed in Section 5.2 is a useful method in achieving such measurements. However, there are still ongoing efforts to improve the analysis process. For

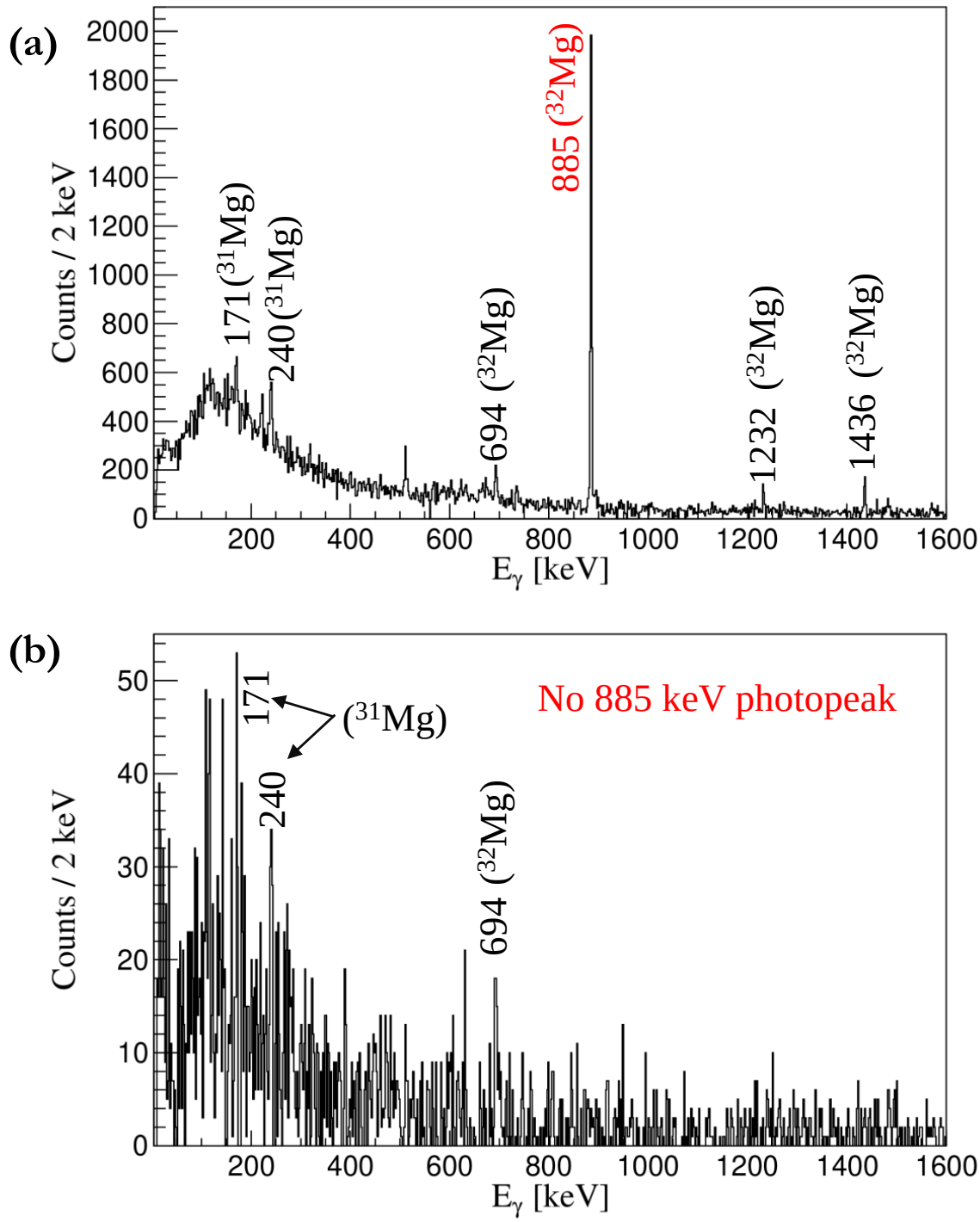

Figure 5.10: **(a)**: β-delayed γ-ray spectrum for γ rays detected in the SeGA detectors within a correlation window of 39.6 ms, corresponding to three ^{32}Na β-decay half-lives ($T_{1/2}$ = 13.2 ms). (The 885-keV γ-ray transition is emphasized in red.) **(b)**: γ ray spectrum in (a) filled with additional 3 ns < t_{LaBr_3} - t_{PSPMT} ≤ 20 ns condition.

one, distinguishing and identifying distinct peaks corresponding to individual γ-ray transitions in the $CeBr_3$ energy spectrum is challenging due to the combined energy deposition from both γ rays and β-decay electrons in the $CeBr_3$ implantation detector.

CHAPTER VI

SUMMARY AND OUTLOOK

A summary and opportunities for future work on the crux of this dissertation is discussed below. Other points specific to results presented on the investigation of the 0_2^+ states in ^{34}Si and ^{32}Mg, are discussed in Chapter V.

Low-lying $(7/2_1^-)$ and $(3/2_1^-)$ isomeric states at 68 and 156 keV in ^{37}Si were studied at the NSCL following their population in the β^-n and β^- decay of implanted ^{38}Al and ^{37}Al ions, respectively. New structure information including the half-life of the 68-keV state was measured as 9.1(7) ns as well as the ground-state transition strength, $B(M1)$ measured as 0.0137(11) μ_N^2, assuming a pure $M1$ transition. Similar measurements for the 156-keV transition were also carried out using various methods described in Chapter IV of this dissertation, with the half-life and $B(M1)$ transition strength measured as 3.20(4) ns and 0.00325(4) μ_N^2, respectively and found to be in agreement with a previous measurement of 3.0(7) ns [67]. The experimental results were found to be consistent with large-scale shell model predictions.

Theoretical calculations reported in Ref. [67] suggest the existence of two low-lying nanosecond isomers in ^{39}Si, including a $(7/2^-)$ state at 172 keV with a half-life of 0.97(7) ns [67] as shown in Figure 6.1. The other isomeric state has not yet been observed, and none of the states in ^{39}Si have been accessed via β decay. The 172-keV ground-state $M1$ transition established in Ref. [67] can be observed in Figure 6.2, alongside an 877-keV γ ray reported as 879(14) keV in Ref. [67], indicating

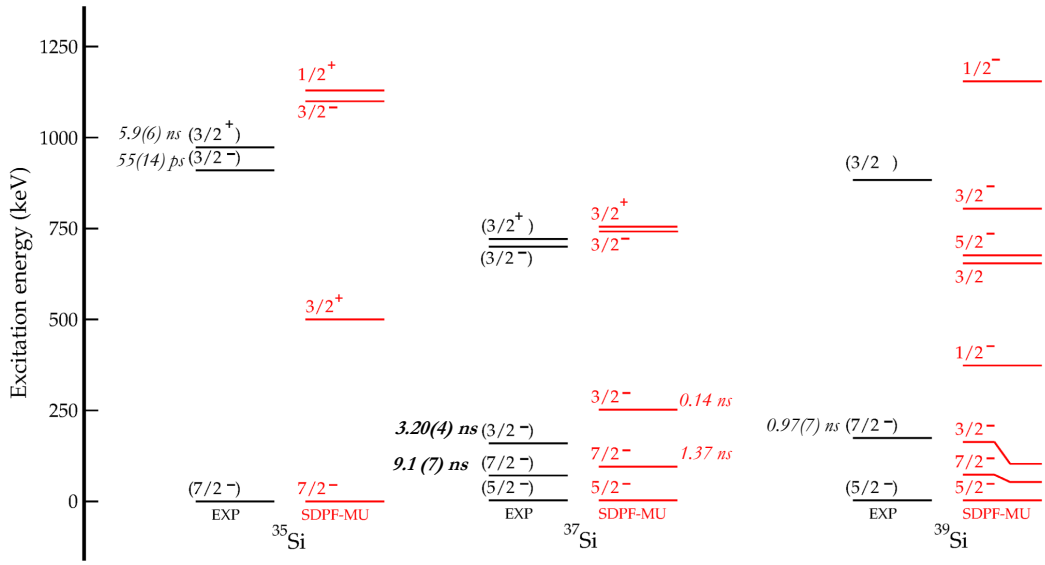

Figure 6.1: Experimental and theoretical level schemes for low-lying states in ^{35}Si, ^{37}Si, and ^{39}Si, including predicted nanosecond isomers in ^{37}Si and ^{39}Si. Experimental half-life data for isomers in ^{39}Si are from Ref. [67], and for the $(3/2^+_1)$ and $(3/2^-_1)$ states in ^{35}Si from Ref. [46] and Ref. [67], respectively. Newly measured half-lives are shown to the left of corresponding levels in ^{37}Si.

that states in ^{39}Si were accessed in E16032 due to the implantation of ^{39}Al ions as highlighted in Figure 3.7.

The prediction of a second low-lying isomeric state can be verified by using the methods discussed in Chapters IV and V to measure the half-life of a corresponding isomeric transition. The observation and characterization of isomeric states in Si isotopes will validate shell model predictions of closely-lying low-energy isomeric states in neutron-rich odd-A Si isotopes approaching the $N = 28$ shell gap as illustrated in Figure 6.1.

By pursuing these future research directions, including the exploration of isomeric states, analysis of decay pathways, investigation of shape coexistence, utilization of theoretical modeling, and advancements in experimental techniques, a more coherent and comprehensive understanding

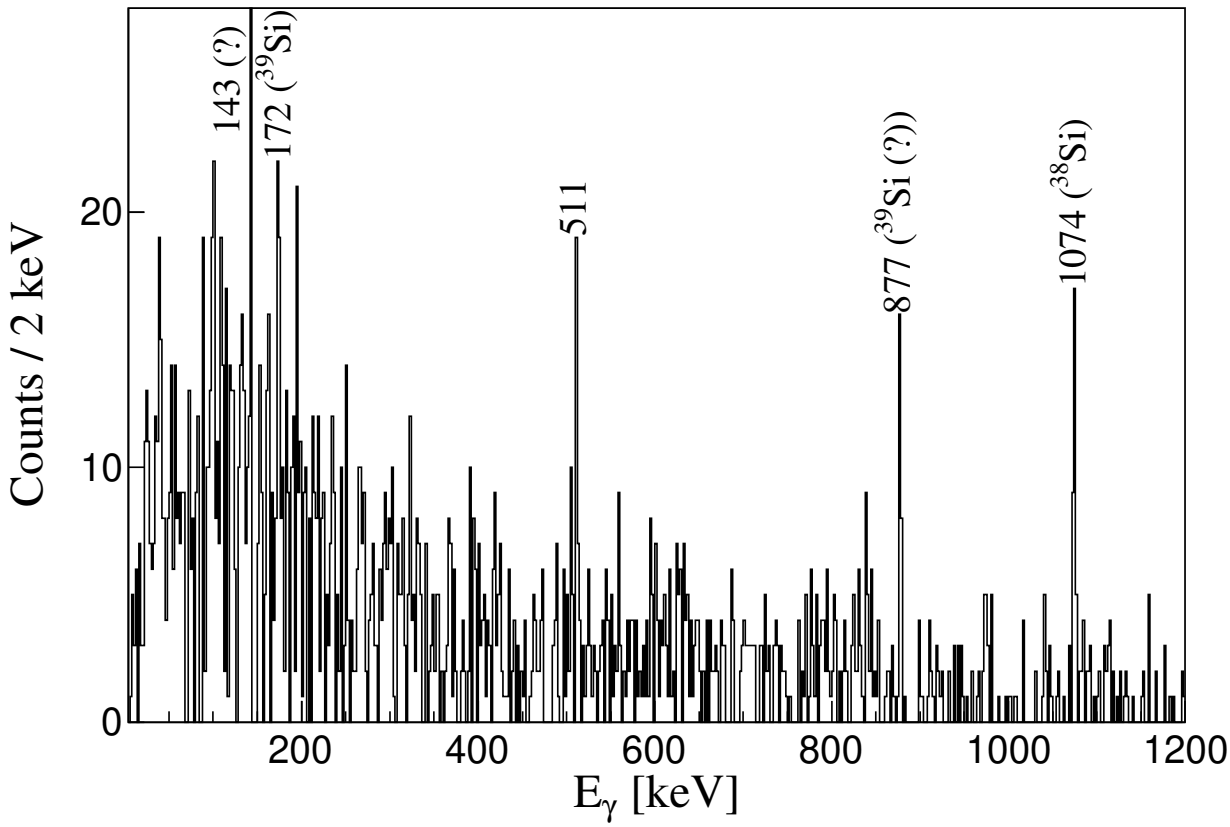

Figure 6.2: β-delayed γ-ray spectrum for γ rays detected in the SeGA detectors within a correlation window of 23 ms which corresponds to three ^{39}Al β-decay half-lives. Previously observed γ-ray transitions in the ^{39}Si daughter [67] are labeled with their respective energies, as well as transitions in the β-delayed one-neutron emission ^{38}Si daughter. The 143-keV transition is unplaced.

of the nuclear structure and properties of ^{37}Si can be achieved. These studies will contribute to the broader understanding of exotic nuclei and their evolution in the neutron-rich region.

REFERENCES

[1] "BrIcc Conversion Coefficient Calculator, Research School of Physics, ANU College of Science,", https://bricc.anu.edu.au/.

[2] "Evaluated nuclear structure data file (ENSDF),", https://www.nndc.bnl.gov/ensdf/.

[3] "National Nuclear Data Center (log ft),", https://www.nndc.bnl.gov/logft/.

[4] B. Abromeit, V. Tripathi, H. L. Crawford, S. N. Liddick, S. Yoshida, Y. Utsuno, P. C. Bender, B. P. Crider, R. Dungan, P. Fallon, K. Kravvaris, N. Larson, R. S. Lubna, T. Otsuka, C. J. Prokop, A. L. Richard, N. Shimizu, S. L. Tabor, and A. Volya, "β decay of $T_z = +\frac{11}{2}$ isotopes ^{37}Al and ^{39}Si: Understanding Gamow-Teller strength distribution in neutron-rich nuclei," *Physical Review C*, vol. 100, 2019, p. 014323.

[5] S. Agostinelli, J. Allison, K. Amako, J. Apostolakis, H. Araujo, P. Arce, M. Asai, D. Axen, S. Banerjee, G. Barrand, F. Behner, L. Bellagamba, J. Boudreau, L. Broglia, A. Brunengo, H. Burkhardt, S. Chauvie, J. Chuma, R. Chytracek, G. Cooperman, G. Cosmo, P. Degtyarenko, A. Dell'Acqua, G. Depaola, D. Dietrich, R. Enami, A. Feliciello, C. Ferguson, H. Fesefeldt, G. Folger, F. Foppiano, A. Forti, S. Garelli, S. Giani, R. Giannitrapani, D. Gibin, J. Gómez Cadenas, I. González, G. Gracia Abril, G. Greeniaus, W. Greiner, V. Grichine, A. Grossheim, S. Guatelli, P. Gumplinger, R. Hamatsu, K. Hashimoto, H. Hasui, A. Heikkinen, A. Howard, V. Ivanchenko, A. Johnson, F. Jones, J. Kallenbach, N. Kanaya, M. Kawabata, Y. Kawabata, M. Kawaguti, S. Kelner, P. Kent, A. Kimura, T. Kodama, R. Kokoulin, M. Kossov, H. Kurashige, E. Lamanna, T. Lampén, V. Lara, V. Lefebure, F. Lei, M. Liendl, W. Lockman, F. Longo, S. Magni, M. Maire, E. Medernach, K. Minamimoto, P. Mora de Freitas, Y. Morita, K. Murakami, M. Nagamatu, R. Nartallo, P. Nieminen, T. Nishimura, K. Ohtsubo, M. Okamura, S. O'Neale, Y. Oohata, K. Paech, J. Perl, A. Pfeiffer, M. Pia, F. Ranjard, A. Rybin, S. Sadilov, E. Di Salvo, G. Santin, T. Sasaki, N. Savvas, Y. Sawada, S. Scherer, S. Sei, V. Sirotenko, D. Smith, N. Starkov, H. Stoecker, J. Sulkimo, M. Takahata, S. Tanaka, E. Tcherniaev, E. Safai Tehrani, M. Tropeano, P. Truscott, H. Uno, L. Urban, P. Urban, M. Verderi, A. Walkden, W. Wander, H. Weber, J. Wellisch, T. Wenaus, D. Williams, D. Wright, T. Yamada, H. Yoshida, and D. Zschiesche, "Geant4—a simulation toolkit," *Nuclear Instruments and Methods in Physics Research Section A: Accelerators, Spectrometers, Detectors and Associated Equipment*, vol. 506, 2003, pp. 250–303.

[6] P. Baumann, A. Huck, G. Klotz, A. Knipper, G. Walter, G. Marguier, H. Ravn, C. Richard-Serre, A. Poves, and J. Retamosa, "^{34}Si: A new doubly magic nucleus?," *Physics Letters B*, vol. 228, 1989, pp. 458–462.

[7] B. A. Brown, *Lecture Notes in Nuclear Structure Physics*, Department of Physics and Astronomy, Michigan State University, 2005.

[8] B. A. Brown and B. H. Wildenthal, "Status of the Nuclear Shell Model," *Annual Review of Nuclear and Particle Science*, vol. 38, no. 1, 1988, pp. 29–66.

[9] E. Caurier, F. Nowacki, and A. Poves, "Shell model studies of neutron-rich nuclei," *Nuclear Physics A*, vol. 693, no. 1, 2001, pp. 374–382, Radioactive Nuclear Beams.

[10] A. Chester, B. A. Brown, S. P. Burcher, M. P. Carpenter, J. J. Carroll, C. J. Chiara, P. A. Copp, B. P. Crider, J. T. Harke, D. E. M. Hoff, K. Kolos, S. N. Liddick, B. Longfellow, M. J. Mogannam, T. H. Ogunbeku, C. J. Prokop, D. Rhodes, A. L. Richard, O. A. Shehu, A. S. Tamashiro, R. Unz, and Y. Xiao, "Identification of a new isomeric state in ^{76}Zn following the β decay of ^{76}Cu," *Phys. Rev. C*, vol. 104, Nov 2021, p. 054314.

[11] A. Chester, B. A. Brown, S. P. Burcher, M. P. Carpenter, J. J. Carroll, C. J. Chiara, P. A. Copp, B. P. Crider, J. T. Harke, D. E. M. Hoff, K. Kolos, S. N. Liddick, B. Longfellow, M. J. Mogannam, T. H. Ogunbeku, C. J. Prokop, D. Rhodes, A. L. Richard, O. A. Shehu, A. S. Tamashiro, R. Unz, and Y. Xiao, "Half-life measurement of the 199-keV isomeric state in ^{76}Ga," *Phys. Rev. C*, vol. 105, Feb 2022, p. 024319.

[12] H. D. Chuong, T. T. Thanh, L. T. Ngoc Trang, V. H. Nguyen, and C. V. Tao, "Estimating thickness of the inner dead-layer of n-type HPGe detector," *Applied Radiation and Isotopes*, vol. 116, 2016, pp. 174–177.

[13] E. L. Church and J. Weneser, "Electric-Monopole Transitions in Atomic Nuclei," *Phys. Rev.*, vol. 103, Aug 1956, pp. 1035–1044.

[14] B. Crider, C. Prokop, S. Liddick, H. Albers, M. Alshudifat, A. Ayangeakaa, M. Carpenter, J. Carroll, J. Chen, C. Chiara, A. Dombos, S. Go, R. Grzywacz, J. Harker, R. Janssens, N. Larson, T. Lauritsen, R. Lewis, S. Quinn, F. Recchia, D. Seweryniak, A. Spyrou, S. Suchyta, W. Walters, and S. Zhu, "New method for level-lifetime measurements with thick scintillators," *Nuclear Instruments and Methods in Physics Research Section A: Accelerators, Spectrometers, Detectors and Associated Equipment*, vol. 1055, 2023, p. 168525.

[15] J. dos Santos, C. Monteiro, R. Morgado, and C. Conde, "Energy linearity of high-purity germanium detectors in the region of the Ge K-absorption edge: Experimental results," *Applied Radiation and Isotopes*, vol. 53, no. 4, 2000, pp. 739–743.

[16] A. Elanique, O. Marzocchi, D. Leone, L. Hegenbart, B. Breustedt, and L. Oufni, "Dead layer thickness characterization of an HPGe detector by measurements and Monte Carlo simulations," *Applied Radiation and Isotopes*, vol. 70, no. 3, 2012, pp. 538–542.

[17] R. Elder, H. Iwasaki, J. Ash, D. Bazin, P. C. Bender, T. Braunroth, B. A. Brown, C. M. Campbell, H. L. Crawford, B. Elman, A. Gade, M. Grinder, N. Kobayashi, B. Longfellow, A. O. Macchiavelli, T. Mijatović, J. Pereira, A. Revel, D. Rhodes, J. A. Tostevin, and D. Weisshaar, "Intruder dominance in the 0_2^+ state of ^{32}Mg studied with a novel technique for in-flight decays," *Phys. Rev. C*, vol. 100, Oct 2019, p. 041301.

[18] C. Force, S. Grévy, L. Gaudefroy, O. Sorlin, L. Caceres, F. Rotaru, J. Mrazek, N. Achouri, J. Angélique, F. Azaiez, B. Bastin, R. Borcea, A. Buta, J. Daugas, Z. Dlouhy, Z. Dombrádi, F. de Oliveira santos, F. Negoita, Y. Penionzhkevich, and F. Nowacki, "Prolate-Spherical Shape Coexistence at $N = 28$ in ^{44}S," *Physical review letters*, vol. 105, 09 2010, p. 102501.

[19] N. Fukunishi, T. Otsuka, and T. Sebe, "Vanishing of the shell gap in $N = 20$ neutron-rich nuclei," *Physics Letters B*, vol. 296, no. 3, 1992, pp. 279–284.

[20] A. Gade and S. N. Liddick, "Shape coexistence in neutron-rich nuclei," *Journal of Physics G*, vol. 43, 2016, p. 024001.

[21] A. Gade and B. M. Sherrill, "NSCL and FRIB at Michigan State University: Nuclear science at the limits of stability," *Physica Scripta*, vol. 91, no. 5, Apr 2016, p. 053003.

[22] T. Glasmacher, B. Brown, M. Chromik, P. Cottle, M. Fauerbach, R. Ibbotson, K. Kemper, D. Morrissey, H. Scheit, D. Sklenicka, and M. Steiner, "Collectivity in ^{44}S," *Physics Letters B*, vol. 395, no. 3, 1997, pp. 163–168.

[23] O. Haxel, J. H. D. Jensen, and H. E. Suess, "On the Magic Numbers in Nuclear Structure," *Phys. Rev.*, vol. 75, Jun 1949, pp. 1766–1766.

[24] K. Heyde and J. L. Wood, "Intruder states and shape coexistence in the region N approximately 20, Z approximately 12," *Journal of Physics G: Nuclear and Particle Physics*, vol. 17, no. 2, feb 1991, p. 135.

[25] K. Heyde and J. L. Wood, "Shape coexistence in atomic nuclei," *Rev. Mod. Phys.*, vol. 83, Nov 2011, pp. 1467–1521.

[26] R. W. Ibbotson, T. Glasmacher, B. A. Brown, L. Chen, M. J. Chromik, P. D. Cottle, M. Fauerbach, K. W. Kemper, D. J. Morrissey, H. Scheit, and M. Thoennessen, "Quadrupole Collectivity in ^{32,34,36,38}Si and the $N = 20$ Shell Closure," *Phys. Rev. Lett.*, vol. 80, Mar 1998, pp. 2081–2084.

[27] G. F. Knoll, *Radiation Detection and Measurement*, 4th edition, Wiley, 2000.

[28] T. Kurtukian-Nieto, J. Benlliure, and K.-H. Schmidt, "A new analysis method to determine beta-decay half-lives in experiments with complex background," *Nuclear Instruments and Methods in Physics Research Section A: Accelerators, Spectrometers, Detectors and Associated Equipment*, vol. 589, no. 3, 2008, pp. 472–483.

[29] R. L. Lewis, "Indirect neutron-capture cross sections for the weak r-process," *Ph.D. Thesis, Michigan State University*, 2019.

[30] R. Lică, F. Rotaru, M. J. G. Borge, S. Grévy, F. Negoiţă, A. Poves, O. Sorlin, A. N. Andreyev, R. Borcea, C. Costache, H. De Witte, L. M. Fraile, P. T. Greenlees, M. Huyse, A. Ionescu, S. Kisyov, J. Konki, I. Lazarus, M. Madurga, N. Mărginean, R. Mărginean, C. Mihai, R. E. Mihai, A. Negret, F. Nowacki, R. D. Page, J. Pakarinen, V. Pucknell, P. Rahkila, E. Rapisarda, A. Şerban, C. O. Sotty, L. Stan, M. Stănoiu, O. Tengblad, A. Turturică, P. Van Duppen, N. Warr, P. Dessagne, T. Stora, C. Borcea, S. Călinescu, J. M. Daugas, D. Filipescu, I. Kuti, S. Franchoo, I. Gheorghe, P. Morfouace, P. Morel, J. Mrazek, D. Pietreanu, D. Sohler, I. Stefan, R. Şuvăilă, S. Toma, and C. A. Ur, "Normal and intruder configurations in ^{34}Si populated in the β^- decay of ^{34}Mg and ^{34}Al," *Phys. Rev. C*, vol. 100, Sep 2019, p. 034306.

[31] R. Lică, F. Rotaru, M. J. G. Borge, S. Grévy, F. Negoiţă, A. Poves, O. Sorlin, A. N. Andreyev, R. Borcea, C. Costache, H. De Witte, L. M. Fraile, P. T. Greenlees, M. Huyse, A. Ionescu, S. Kisyov, J. Konki, I. Lazarus, M. Madurga, N. Mărginean, R. Mărginean, C. Mihai, R. E. Mihai, A. Negret, R. D. Page, J. Pakarinen, S. Pascu, V. Pucknell, P. Rahkila, E. Rapisarda, A. Şerban, C. O. Sotty, L. Stan, M. Stănoiu, O. Tengblad, A. Turturică, P. Van Duppen, R. Wadsworth, and N. Warr, "Identification of the crossing point at $N = 21$ between normal and intruder configurations," *Phys. Rev. C*, vol. 95, Feb 2017, p. 021301.

[32] B. Longfellow, P. Bender, J. Belarge, A. Gade, and D. Weisshaar, "Commissioning of the $LaBr_3$(Ce) detector array at the National Superconducting Cyclotron Laboratory," *Nuclear Instruments and Methods in Physics Research Section A: Accelerators, Spectrometers, Detectors and Associated Equipment*, vol. 916, 2019, pp. 141–147.

[33] W. Loveland, D. J. Morrissey, and G. T. Seaborg, *Modern Nuclear Chemistry*, John Wiley & Sons, Inc., New Jersey, 2006.

[34] R. S. Lubna, K. Kravvaris, S. L. Tabor, V. Tripathi, E. Rubino, and A. Volya, "Evolution of the $N = 20$ and 28 shell gaps and two-particle-two-hole states in the FSU interaction," *Phys. Rev. Res.*, vol. 2, Dec 2020, p. 043342.

[35] H. Mach, L. M. Fraile, O. Tengblad, R. Boutami, C. Jollet, W. A. P lóciennik, D. T. Yordanov, M. Stanoiu, M. J. G. Borge, P. A. Butler, J. Cederkäll, P. Dessagne, B. Fogelberg, H. Fynbo, P. Hoff, A. Jokinen, A. Korgul, U. Köster, W. Kurcewicz, F. Marechal, T. Motobayashi, J. Mrazek, G. Neyens, T. Nilsson, S. Pedersen, A. Poves, B. Rubio, and E. Ruchowska, "New structure information on ^{30}Mg, ^{31}Mg and 32Mg," *The 4th International Conference on Exotic Nuclei and Atomic Masses*, Berlin, Heidelberg, 2005, pp. 105–109, Springer Berlin Heidelberg.

[36] H. Mach, R. Gill, and M. Moszyński, "A method for picosecond lifetime measurements for neutron-rich nuclei: (1) Outline of the method," *Nuclear Instruments and Methods in Physics Research Section A: Accelerators, Spectrometers, Detectors and Associated Equipment*, vol. 280, no. 1, 1989, pp. 49–72.

[37] C. M. Mattoon, F. Sarazin, G. Hackman, E. S. Cunningham, R. A. E. Austin, G. C. Ball, R. S. Chakrawarthy, P. Finlay, P. E. Garrett, G. F. Grinyer, B. Hyland, K. A. Koopmans, J. R. Leslie, A. A. Phillips, M. A. Schumaker, H. C. Scraggs, J. Schwarzenberg, M. B. Smith, C. E. Svensson, J. C. Waddington, P. M. Walker, B. Washbrook, and E. Zganjar, "Beta decay of ^{32}Na," *Phys. Rev. C*, vol. 75, Jan 2007, p. 017302.

[38] M. G. Mayer, "On Closed Shells in Nuclei. II," *Phys. Rev.*, vol. 75, Jun 1949, pp. 1969–1970.

[39] P. Miller, F. Marti, D. Poe, M. Steiner, J. Stetson, and X. Y. Wu, "Commissioning of the Coupled Cyclotron Facility at NSCL," *Proceedings of the IEEE Particle Accelerator Conference*, Feb 2001, vol. 4, pp. 2557–2559.

[40] M. Mocko, M. B. Tsang, L. Andronenko, M. Andronenko, F. Delaunay, M. Famiano, T. Ginter, V. Henzl, D. Henzlová, H. Hua, S. Lukyanov, W. G. Lynch, A. M. Rogers, M. Steiner, A. Stolz, O. Tarasov, M.-J. v. Goethem, G. Verde, W. S. Wallace, and A. Zalessov, "Projectile fragmentation of ^{40}Ca, ^{48}Ca, ^{58}Ni, and ^{64}Ni at 140 MeV/nucleon," *Phys. Rev. C*, vol. 74, Nov 2006, p. 054612.

[41] D. Morrissey, "The coupled cyclotron project at the NSCL," *Nuclear Physics A*, vol. 616, no. 1, 1997, pp. 45–55, Radioactive Nuclear Beams.

[42] S. A. Moszkowski, "A Rapid Method of Calculating log(ft) Values for β-Transitions," *Phys. Rev.*, vol. 82, Apr 1951, pp. 35–37.

[43] W. Mueller, J. Church, T. Glasmacher, D. Gutknecht, G. Hackman, P. Hansen, Z. Hu, K. Miller, and P. Quirin, "Thirty-two-fold segmented germanium detectors to identify γ rays from intermediate-energy exotic beams," *Nuclear Instruments and Methods in Physics Research Section A: Accelerators, Spectrometers, Detectors and Associated Equipment*, vol. 466, 07 2001, pp. 492–498.

[44] F. Nowacki and A. Poves, "New effective interaction for 0$\hbar\omega$ shell-model calculations in the *sd*−*pf* valence space," *Phys. Rev. C*, vol. 79, Jan 2009, p. 014310.

[45] *Segmented Germanium Array Service Level Description*, NSCL, 2007, Retrieved from: https://nscl.msu.edu/_files/documents/sega_sld_2007.pdf.

[46] S. Nummela, P. Baumann, E. Caurier, P. Dessagne, A. Jokinen, A. Knipper, G. Le Scornet, C. Miehé, F. Nowacki, M. Oinonen, Z. Radivojevic, M. Ramdhane, G. Walter, and J. Äystö, "Spectroscopy of ^{34,35}Si by β decay: $sd - fp$ shell gap and single-particle states," *Phys. Rev. C*, vol. 63, Mar 2001, p. 044316.

[47] T. H. Ogunbeku, B. P. Crider, S. N. Liddick, B. A. Brown, A. Chester, K. L. Childers, P. Chowdhury, E. Lamere, R. Lewis, B. Longfellow, R. S. Lubna, S. Lyons, S. K. Neupane, D. Perez-Loureiro, C. J. Prokop, A. L. Richard, U. Silwal, D. P. Siwakoti, D. C. Smith, M. K. Smith, and Y. Xiao, "First half-life measurement of a low-lying isomer in ^{37}Si," *Phys. Rev. C*, vol. 108, Sep 2023, p. 034304.

[48] T. Otsuka, "Exotic nuclei and nuclear forces," *Physica Scripta Volume T*, vol. T152, 01 2013, p. 4007.

[49] T. Otsuka, R. Fujimoto, Y. Utsuno, B. A. Brown, M. Honma, and T. Mizusaki, "Magic Numbers in Exotic Nuclei and Spin-Isospin Properties of the *NN* Interaction," *Phys. Rev. Lett.*, vol. 87, Aug 2001, p. 082502.

[50] T. Otsuka, R. Fujimoto, Y. Utsuno, B. A. Brown, M. Honma, and T. Mizusaki, "Magic Numbers in Exotic Nuclei and Spin-Isospin Properties of the *NN* Interaction," *Phys. Rev. Lett.*, vol. 87, Aug 2001, p. 082502.

[51] T. Otsuka, T. Suzuki, R. Fujimoto, H. Grawe, and Y. Akaishi, "Evolution of Nuclear Shells due to the Tensor Force," *Phys. Rev. Lett.*, vol. 95, Nov 2005, p. 232502.

[52] S. Paschalis, P. Fallon, A. O. Macchiavelli, M. Petri, P. C. Bender, M. P. Carpenter, X. Chen, C. J. Chiara, R. M. Clark, M. Cromaz, S. Gros, L. Hamilton, C. R. Hoffman, R. V. F. Janssens, T. Lauritsen, I. Y. Lee, C. J. Lister, E. A. McCutchan, L. Phair, W. Reviol, D. G. Sarantites, D. Seweryniak, S. L. Tabor, Y. Toh, M. Wiedeking, and S. Zhu, "The deformed 0^+ state in ^{34}Si," *Journal of Physics: Conference Series*, vol. 312, no. 9, sep 2011, p. 092050.

[53] M. Pfützner, M. Karny, L. V. Grigorenko, and K. Riisager, "Radioactive decays at limits of nuclear stability," *Rev. Mod. Phys.*, vol. 84, Apr 2012, pp. 567–619.

[54] A. Poves and A. Zuker, "Theoretical spectroscopy and the fp shell," *Physics Reports*, vol. 70, no. 4, 1981, pp. 235–314.

[55] B. Pritychenko, M. Birch, B. Singh, and M. Horoi, "Tables of $E2$ transition probabilities from the first 2^+ states in even–even nuclei," *Atomic Data and Nuclear Data Tables*, vol. 107, 2016, pp. 1–139.

[56] C. Prokop, "Shape Coexistence in the Neutron-Rich Nickel Isotopes near $N = 40$," *Ph.D. Dissertation, Michigan State University*, 2016.

[57] C. Prokop, S. Liddick, B. Abromeit, A. Chemey, N. Larson, S. Suchyta, and J. Tompkins, "Digital data acquisition system implementation at the National Superconducting Cyclotron Laboratory," *Nuclear Instruments and Methods in Physics Research Section A: Accelerators, Spectrometers, Detectors and Associated Equipment*, vol. 741, 2014, pp. 163–168.

[58] C. Prokop, S. Liddick, N. Larson, S. Suchyta, and J. Tompkins, "Optimization of the National Superconducting Cyclotron Laboratory Digital Data Acquisition System for use with fast scintillator detectors," *Nuclear Instruments and Methods in Physics Research Section A: Accelerators, Spectrometers, Detectors and Associated Equipment*, vol. 792, 2015, pp. 81–88.

[59] W. A. Richter, S. Mkhize, and B. A. Brown, "*sd*-shell observables for the USDA and USDB Hamiltonians," *Phys. Rev. C*, vol. 78, Dec 2008, p. 064302.

[60] D. Rogers, "Analytic and graphical methods for assigning errors to parameters in non-linear least squares fitting," *Nuclear Instruments and Methods*, vol. 127, no. 2, 1975, pp. 253–260.

[61] F. Rotaru, F. Negoita, S. Grévy, J. Mrazek, S. Lukyanov, F. Nowacki, A. Poves, O. Sorlin, C. Borcea, R. Borcea, A. Buta, L. Cáceres, S. Calinescu, R. Chevrier, Z. Dombrádi, J. M. Daugas, D. Lebhertz, Y. Penionzhkevich, C. Petrone, D. Sohler, M. Stanoiu, and J. C. Thomas, "Unveiling the Intruder Deformed 0_2^+ State in ^{34}Si," *Phys. Rev. Lett.*, vol. 109, Aug 2012, p. 092503.

[62] O. Shehu, B. Crider, T. Ginter, C. Hoffman, T. Ogunbeku, Y. Xiao, K. Childers, P. Chowdhury, C. Fry, E. Lamere, R. Lewis, S. Liddick, B. Longfellow, S. Lyons, S. Neupane, D. Pérez-Loureiro, C. Prokop, A. Richard, U. Silwal, D. Siwakoti, D. Smith, and M. Smith, "Experimental study of the ^{34m}Cl beam production at intermediate energies," *Nuclear Instruments and Methods in Physics Research Section A: Accelerators, Spectrometers, Detectors and Associated Equipment*, vol. 1035, 2022, p. 166789.

[63] B. M. Sherrill, *Exotic Beam Summer School: Accelerators and Beams*, Facility for Rare Isotope Beams, Michigan State University, 2011.

[64] B. Singh, J. Rodriguez, S. Wong, and J. Tuli, "Review Of Logft Values In β Decay," *Nuclear Data Sheets*, vol. 84, no. 3, 1998, pp. 487–563.

[65] K. Steiger, S. Nishimura, Z. Li, R. Gernhäuser, Y. Utsuno, R. Chen, T. Faestermann, C. Hinke, R. Krücken, M. Kurata-Nishimura, G. Lorusso, Y. Miyashita, N. Shimizu, K. Sugimoto, T. Sumikama, H. Watanabe, and K. Yoshinaga, "Nuclear structure of ^{37,38}Si investigated by decay spectroscopy of ^{37,38}Al," *The European Physical Journal A*, vol. 51, 09 2015.

[66] S. R. Stroberg, A. Gade, J. A. Tostevin, V. M. Bader, T. Baugher, D. Bazin, J. S. Berryman, B. A. Brown, C. M. Campbell, K. W. Kemper, C. Langer, E. Lunderberg, A. Lemasson, S. Noji, T. Otsuka, F. Recchia, C. Walz, D. Weisshaar, and S. Williams, "Neutron single-particle strength in silicon isotopes: Constraining the driving forces of shell evolution," *Phys. Rev. C*, vol. 91, Apr 2015, p. 041302.

[67] S. R. Stroberg, A. Gade, J. A. Tostevin, V. M. Bader, T. Baugher, D. Bazin, J. S. Berryman, B. A. Brown, C. M. Campbell, K. W. Kemper, C. Langer, E. Lunderberg, A. Lemasson, S. Noji, F. Recchia, C. Walz, D. Weisshaar, and S. J. Williams, "Single-particle structure of silicon isotopes approaching ^{42}Si," *Phys. Rev. C*, vol. 90, Sep 2014, p. 034301.

[68] S. Suchyta, S. N. Liddick, Y. Tsunoda, T. Otsuka, M. B. Bennett, A. Chemey, M. Honma, N. Larson, C. J. Prokop, S. J. Quinn, N. Shimizu, A. Simon, A. Spyrou, V. Tripathi, Y. Utsuno, and J. M. VonMoss, "Shape coexistence in ^{68}Ni," *Phys. Rev. C*, vol. 89, Feb 2014, p. 021301.

[69] O. Tarasov and D. Bazin, "LISE++: Exotic beam production with fragment separators and their design," *Nuclear Instruments and Methods in Physics Research Section B: Beam Interactions with Materials and Atoms*, vol. 376, 2016, pp. 185–187, Proceedings of the XVIIth International Conference on Electromagnetic Isotope Separators and Related Topics (EMIS2015), Grand Rapids, MI, U.S.A., 11-15 May 2015.

[70] M. Thoennessen, *The Discovery of Isotopes: A Complete Compilation*, chapter 15: Projectile Fragmentation and Fission, Springer International Publishing, Cham, 2016, pp. 259–273.

[71] V. Tripathi, S. L. Tabor, P. Bender, C. R. Hoffman, S. Lee, K. Pepper, M. Perry, P. F. Mantica, J. M. Cook, J. Pereira, J. S. Pinter, J. B. Stoker, D. Weisshaar, Y. Utsuno, and T. Otsuka, "Excited intruder states in ^{32}Mg," *Phys. Rev. C*, vol. 77, Mar 2008, p. 034310.

[72] Y. Utsuno, T. Otsuka, B. A. Brown, M. Honma, T. Mizusaki, and N. Shimizu, "Shape transitions in exotic Si and S isotopes and tensor-force-driven Jahn-Teller effect," *Phys. Rev. C*, vol. 86, Nov 2012, p. 051301.

[73] A. Volya, "Continuum Shell Model code,", `https://www.volya.net/`.

[74] M. Wang, W. Huang, F. Kondev, G. Audi, and S. Naimi, "The AME 2020 atomic mass evaluation (II). Tables, graphs and references," *Chinese Physics C*, vol. 45, no. 3, mar 2021, p. 030003.

[75] E. K. Warburton and B. A. Brown, "Effective interactions for the $0p1s0d$ nuclear shell-model space," *Phys. Rev. C*, vol. 46, Sep 1992, pp. 923–944.

[76] K. Wimmer, T. Kröll, R. Krücken, V. Bildstein, R. Gernhäuser, B. Bastin, N. Bree, J. Diriken, P. Van Duppen, M. Huyse, N. Patronis, P. Vermaelen, D. Voulot, J. Van de Walle, F. Wenander, L. M. Fraile, R. Chapman, B. Hadinia, R. Orlandi, J. F. Smith, R. Lutter, P. G. Thirolf, M. Labiche, A. Blazhev, M. Kalkühler, P. Reiter, M. Seidlitz, N. Warr, A. O. Macchiavelli, H. B. Jeppesen, E. Fiori, G. Georgiev, G. Schrieder, S. Das Gupta, G. Lo Bianco, S. Nardelli, J. Butterworth, J. Johansen, and K. Riisager, "Discovery of the Shape Coexisting 0^+ State in ^{32}Mg by a Two Neutron Transfer Reaction," *Phys. Rev. Lett.*, vol. 105, Dec 2010, p. 252501.

[77] J. A. Winger, *Coincidence summing in β-decay spectroscopy*, Department of Physics and Astronomy, Mississippi State University, 2017.

[78] *Pixie-16 User Manual*, XIA LLC, 31057 Genstar Rd Hayward, CA 94544 USA, 2019, Retrieved from: https://xia.com/support/pixie-16/.

[79] *Flat panel type mutlianode PMT assembly H13700 series*, XIA LLC, 31057 Genstar Rd Hayward, CA 94544 USA, 2020, Retrieved from: https://www.hamamatsu.com/resources/pdf/etd/H13700_TPMH1370E.pdf.

[80] P. Závodszky, B. Arend, D. Cole, J. Dekamp, M. Doleans, G. Machicoane, F. Marti, P. Miller, J. Moskalik, W. Nurnberger, J. Ottarson, M. Steiner, J. Stetson, J. Vincent, X. Wu, A. Zeller, and Q. Zhao, "Status report of the NSCL/MSU ECR ion sources," *HIGH ENERGY PHYSICS AND NUCLEAR PHYSICS Supp. Jul*, vol. 31, 07 2007.

APPENDIX A

INVESTIGATING ΔE DEPENDENCE ON I2 POSITION

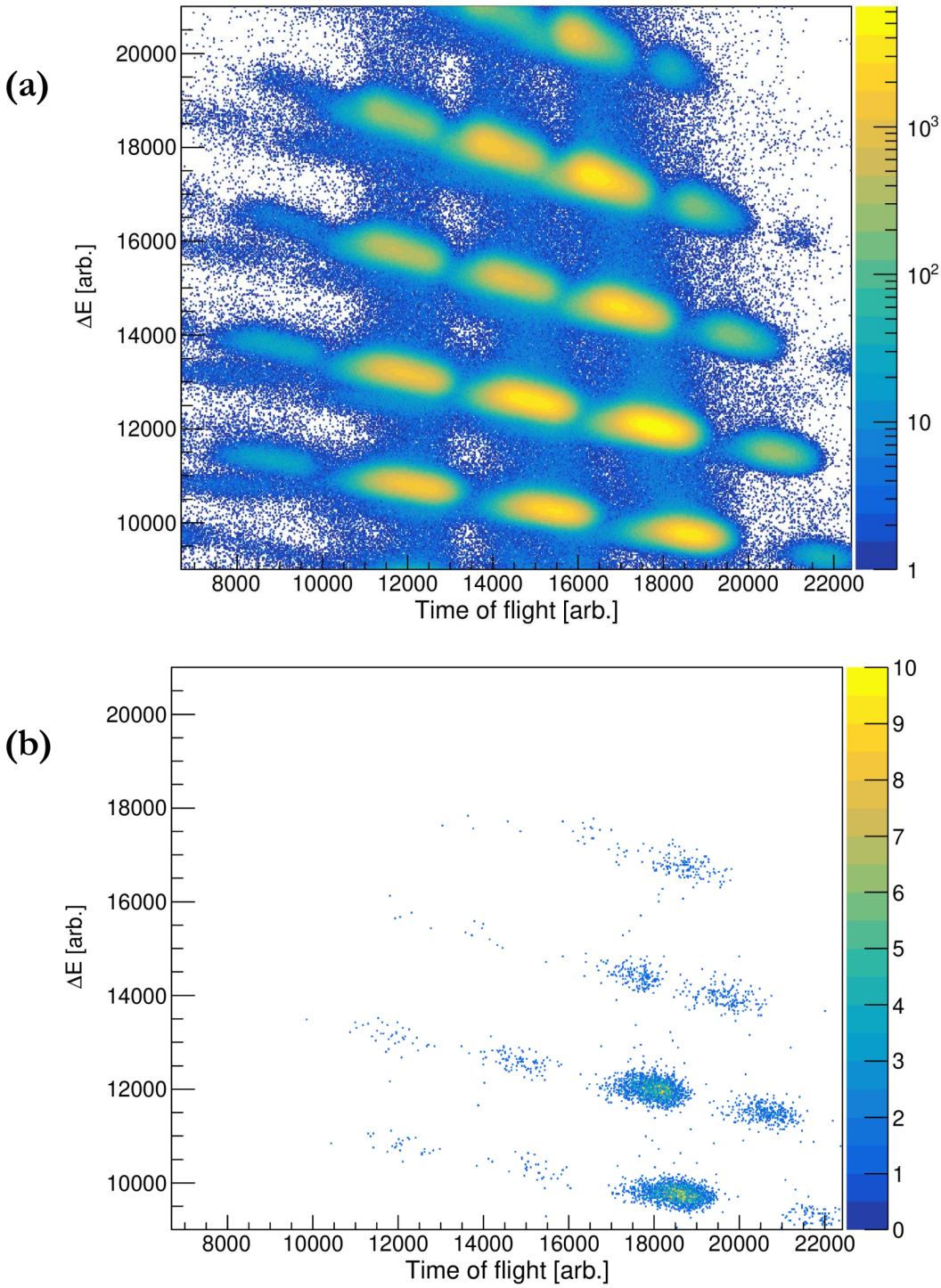

Figure A.1: (a) Raw PID spectrum. (b) PID spectrum gated on distribution "2" in Figure 3.5 (b). The entries observed in (b) can be attributed to the lower-mass isotopes, constituting $\ll 1\%$ of the entries within the raw PID spectrum.

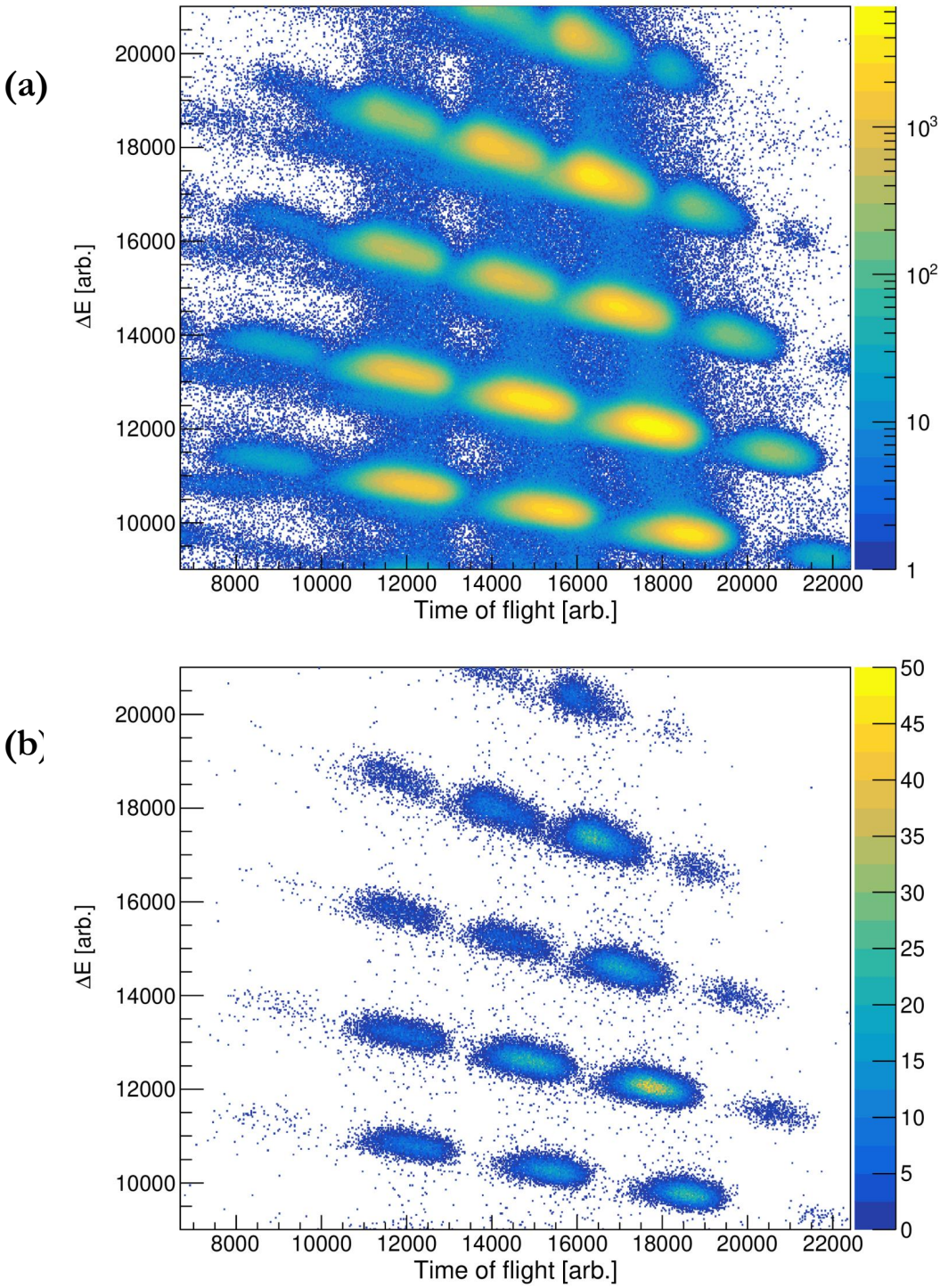

Figure A.2: (a) Raw PID spectrum. (b) Corrrected PID spectrum gated on distribution "3" in Figure 3.5 (b). The entries observed in (b) can be attributed to a retriggering of the I2 scintillator, constituting ~1% of the entries within the raw PID spectrum.

APPENDIX B

AN ALTERNATIVE PROCEDURE TO DETERMINE INTERACTION POSITIONS

In this appendix, I describe an alternative to the procedure discussed in Sec.3.2.2.2 of Chapter III to determine interaction positions necessary for correlating decay electrons to implanted ions. This method reduced the slowness associated with the relatively higher-dimension 2D fitting procedure and involves unfolding the 2D anode energy maps into 1D projections along the x- and y-axes.

Using the x-axis as an example, the projection is fitted using a 1D Lorentzian function of the form

$$L(x) = \frac{A\Gamma^2}{[(x - x_0)^2 + \Gamma^2]} \tag{B.1}$$

where A is the amplitude, x_0 is the position and Γ is the width.

The 1D Lorentzian expressed in B.1 is not linear but can be simplified by finding its reciprocal

$$\frac{1}{L(x)} = \frac{[(x - x_0)^2 + \Gamma^2]}{A\Gamma^2}, \tag{B.2}$$

then making the substitutions $\sigma = \Gamma^2$; $a = \frac{1}{A\sigma}$; $b = \frac{-2x_0}{A\sigma}$; and $c = \frac{x_0^2+\sigma}{A\sigma}$ for convenience, such that B.2 becomes the quadratic equation

$$\frac{1}{L(x)} = ax^2 + bx + c. \tag{B.3}$$

Parameters a, b and c can be determined by evaluating the partial derivative of χ^2 for a fit function $f(x)$ such that

$$\chi^2 = \sum [w_i(y_i - f(x_i))^2], \tag{B.4}$$

where w is the weight, y is the observed data and $f(x_i) = \frac{1}{L(x)}$.

The partial derivatives reduce to a matrix equation $Mu = v$ where u represents the fit parameters and v depends on the observed data. The parameters are determined by solving the matrix equation. M, v and u are defined after taking projections along either axes.

Lastly, a, b and c are transformed back to the parameters of the 1D Lorentzian for both x and y projections using $A = \frac{1}{a\sigma}; x_0 = \frac{-b}{2a}; \sigma = \frac{c-x_0^2}{a}$ to obtain the relevant position parameters, depending on the axis of projection.

APPENDIX C

COMPARISONS BETWEEN EXPERIMENTAL AND THEORETICAL M1 MATRIX ELEMENTS

Table C.1: Comparisons between experimental and theoretical matrix elements for low-lying ground-state $M1$ transitions in ^{37}Si.

		$M(M1)$		
Transition	E_γ (keV)	Exp. (μ_N)	SDPF-MU (μ_N)	SDPF-U-SI (μ_N)
$(7/2^-_1) \rightarrow (5/2^-_{g.s.})$	68	0.33(3)	0.54	0.076
$(3/2^-_1) \rightarrow (5/2^-_{g.s.})$	156	0.114(2)	0.268	0.044

In Ref. [59], experimental $M1$ matrix elements were compared to large-scale theoretical evaluations for 111 low-lying $M1$ transitions in sd-shell nuclei between $A = 16$ and $A = 40$. For succinct comparisons, the experimental and theoretical $B(M1)$ values obtained for this work were converted into reduced $M1$ transition matrix elements, $M(M1)$ using the relationship:

$$M(M1) = \left|\sqrt{B(M1) \times (2J_i + 1)}\right| \tag{C.1}$$

where J_i represents the spin assigned to the initial state undergoing de-excitation.

The measured $M(M1)$ values are displayed in Table C.1 and show good agreement with shell model calculations. This is consistent with similar observations made for other sd-shell nuclei, as illustrated in the bottom-right panel of FIG. 4 in Ref. [59]. In that panel, a cluster of data points can be seen near the diagonal[1], indicating a convergence of experimental and theoretical results for such small magnitudes of $M(M1)$ values.

[1]In the plot, each individual point represents a comparison between experimental and theoretical values. Points that fall along the diagonal line indicate that the values are the same between experiment and theory.